Spatial Dependence of Photocurrent & Photogeneration Mechanisms in Graphene Field Effect Transistors

Gareth Melin

A Thesis
In the Department
of
Physics

Presented in Partial Fulfillment of the Requirements
For the Degree of
Master of Science (Physics) at
Concordia University
Montreal, Quebec, Canada

August 2019

CONCORDIA UNIVERSITY
SCHOOL OF GRADUATE STUDIES

This is to certify that the thesis prepared

By: **Gareth Melin**

Entitled: **Spatial Dependence of Photocurrent & Photogeneration Mechanisms in Graphene Field Effect Transistors**

and submitted in partial fulfillment of the requirements for the degree of

MASTER OF SCIENCE (Physics)

complies with the regulations of the University and meets the accepted standards with respect to originality and quality.

Signed by the final Examining Committee:

_____ Chair

_____ Examiner

_____ Examiner

_____ Thesis Supervisor 1
Valter Zazubovits

_____ Thesis Supervisor 2
Alexandre Champagne

Approved by

_____
Pablo Bianucci, Graduate Program Director

_____ _____
André Roy, Dean, Faculty of Arts & Science

Abstract

Spatial Dependence of Photocurrent & Photogeneration Mechanisms in Graphene Field Effect Transistors

Gareth Melin, M.Sc.
Concordia University, 2019

Graphene is a fascinating 2D material, known for its unique charge transport and optical properties due to its low dimensionality and unique band structure. Although photocurrents in graphene have been heavily studied, there is little consensus on the photogeneration mechanisms contributing to photocurrents in applied graphene devices. There are two primary contributors to photocurrent that we investigate herein: the photovoltaic effect and the photothermoelectric effect. For short-circuit measurement configurations, the photobolometric effect is negligible due to requiring a non-zero bias voltage. Understanding the role each mechanism plays can aid in the design and operation of graphene-based photodetectors. If the mechanisms' contributions are tunable, we can design a photodetector such that the most photoresponsive mechanism dominates, resulting in greater photosensitivity.

We report simultaneous photocurrent and micro-Raman measurements in mono- and bi-layer graphene rectangular transistors of at least 2 μm width and 4 μm length, on Si substrate with 300 nm SiO_2 layer at room temperature and ambient pressure in source-drain configuration, seeking to disambiguate the contribution between photovoltaic and photothermoelectric effects from spatial and power dependencies. Devices presented demonstrated photoresponsivities of up to (229.4 ± 2.5) $\mu A\ W^{-1}$ for bilayer and (159 ± 2) $\mu A\ W^{-1}$ for monolayer when comparable in size and shape. To ensure consistent and comparable results throughout our experiments, we measure Raman spectra during the photoresponse measurements, as well as

gate sweeps before each set of measurements. We found that in order to yield reproducible results without a vacuum, we must employ a laser-annealing technique to reduce the influence of surface moisture. Adsorbed water molecules dope the graphene with holes, affecting transport, but through laser annealing we can ensure that the sample is in the same initial state before each experiment. We measured the photocurrents while observing their dependence on laser spot position on the sample and on laser power intensity. The photocurrent exponents extracted ranged from 0.6 to 1.1, indicating that likely both photovoltaic and photothermoelectric effects contribute to the total photocurrent in varying amounts, with photovoltaic being the dominant effect close to the contacts, likely due to limitations of the electron mean free path of around 7-200 nm and laser spot FWHM between 0.3 μm and 0.4 μm. We also noted that some sample properties evolved over the course of hours or days, suggesting perhaps a shift in charge density during the course of longer experiments experiment.

Acknowledgements

It hasn't always been easy, and I had many challenges along the way, but I had many people who helped to support and guide me while working toward this degree. I can't possibly express the amount of gratitude I feel toward all those who have been positive influences on me, so I hope they will all forgive me for this less-than-comprehensive list of thank-yous.

To my supervisors, Alex and Valter, thank you so much for your guidance and wisdom as I worked on studying photocurrents in graphene transistors and for always being supportive of me, even as I faced great challenges along the way. The greatest lesson that you taught me was to take charge of my project and think critically about the big picture, rather than simply follow orders. In the beginning of my research, you gave me a starting point, along the way I found many paths, and in the end I made the decisions leading to the final results. Your co-supervision gave me the unique opportunity to experience your different leadership and project management styles, and I will do my best to incorporate the best of both worlds in my future endeavors.

To the Champagne Group, thank you all for your collaboration working in the lab. You're serious researchers, but you also know how to make a guy laugh. Special thanks to Andrew: you never turned me away when I asked for your help and were always generous with your time and knowledge, even when you had your own business to take care of. You were a great mentor that I could always count on, an even greater friend, and you always seem to know the right music to fit the mood.

To my parents, Jonathan and Jeri, you have always been supportive of me, have always been my biggest fans, and I've always felt your unconditional love. You encouraged me to do my best and to follow my interests. I've always looked up to you guys, and you continue to inspire me. I'll love you forever, I'll like you for always.

To Carol, thanks for being the best Grammy I've ever known. I especially enjoy our long

phone conversations, even though you claim to not be very newsy. You have always been a joy to be around, and your love knows no bounds.

To Bruce & Gail, you were always there for me when I needed it most. You two made me feel at home away from home, and I'll always cherish your company on the "NDG bus." I'm thankful for all you've done for me.

To David, thanks for your wisdom and especially for listening.

To Kyle, Matthew, and Tom, for being good friends and for staying in touch, despite international and continental divides.

To professor Behrman, thank you for inspiring me to become a physicist, and making physics fun. I have never seen a scientist or professor as passionate and animated about teaching as you, and I continue to look up to you as a role model. Thanks to you, I will never forget to write my units because to have "naked numbers is lewd, crude, and scientifically unacceptable!"

Contribution of the Author

The original research work contained in this thesis is presented in Chapters 3 & 4. In chapter 3 we describe the existing instrumentation, modifications, and protocols necessary to make spatially-resolved Raman & photocurrent measurements. In chapter 4 we report our main scientific results.

Contents

List of Figures

List of Tables

Chapter 1

Introduction: Graphene Transistor Photoresponse

By optically exciting micron-scale graphene transistors, we can study photon-electron and photon-phonon interactions in graphene. Our purpose is to better understand the dominant photocurrent generation mechanisms and how they vary with charge density, density of states (number of layers), and spatial distance between the laser spot and the electrical contacts. Graphene is attractive as a material for photodetectors due to its lack of a band gap, ultra-fast response times, high carrier mobility, high internal quantum efficiency for converting absorbed photons into electric current, and modestly high photoresponse. Although much research has focused on the dominant photocurrent generation mechanisms in graphene, there is much disagreement over which mechanisms dominate and under what conditions. Some claim that the photothermoelectric effect dominates photoresponse except in suspended devices [1], while others claim that the photovoltaic or photobolometric effects are primarily responsible for photoresponse [2]. Still others claim that the photo-bolometric effect outperforms the others [3]. In particular, very few have investigated the spatial-dependence of photocurrent generation, and to the best of our knowledge none have investigated how the photogeneration mechanisms' contributions to the net photocurrent vary with excitation laser spot position. In this thesis, we present our apparatus for distinguishing the contributions of the most likely contributors to photocurrent and how they depend on charge density and laser spot distance from source-drain electrodes in mono- and bi-layer graphene transistors.

We optically excite our graphene using a Raman spectrometer apparatus while simultaneously performing electron transport measurements at ambient pressure and room temperature. The

system's translation stage allows us to optically anneal the device and control the laser spot location, while the graphene transistor's electron transport is probed using source, drain, and gate electrodes. To make our simultaneous optical and electronic measurements, we interfaced and synchronized independently-operating experimental apparatuses. In order to distinguish bulk graphene from edge effects, we require devices of dimensions significantly larger than the laser spot FWHM, which is around 336-432 nm.

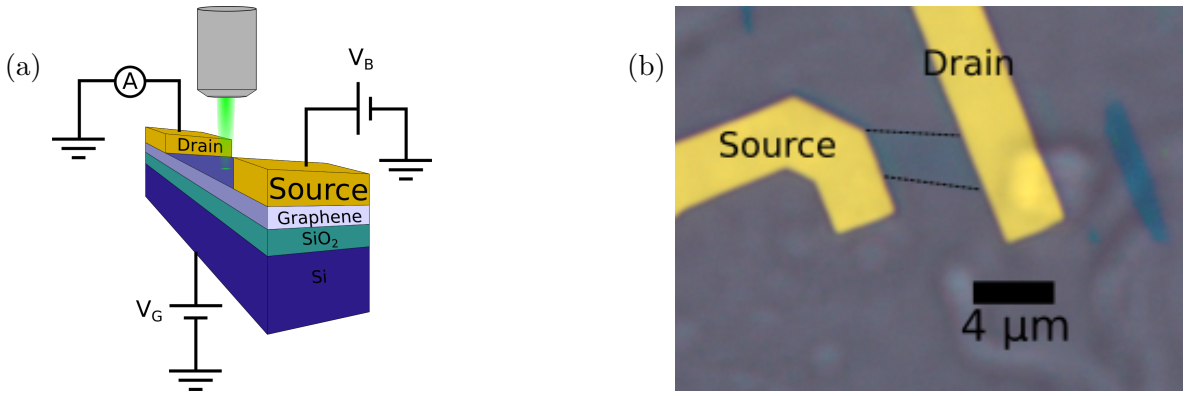

Figure 1.1: Opto-electronic instrumentation for micron-scale graphene graphene devices. (a) Cartoon of optoelectronic apparatus. Light is incident on the sample, a bias voltage is applied at the source electrode, current is measured at the drain electrode, and a gate voltage creates an electric field orthogonal to the graphene sheet. (b) Optical image of a sample device, with scalebar, representing the approximate size of our devices.

1.1 Photoresponse in Graphene Transistors: Recent Experimental Results

Graphene has many desirable qualities for use in photodetectors and there has been great effort in the field to understand the underlying physics of photogeneration in graphene devices. There remains much to be understood, and to some extent the current research disagrees on which proposed mechanisms dominate and under what conditions. Additionally, although graphene has broadband wavelength response, ultrafast response times and a large internal quantum efficiency, it suffers from high background current and a low external quantum efficiency due to its low optical absorption of about 2.3 %. Research into graphene photodetectors tends to fall into one of two categories: distinguishing the photogeneration mechanisms and optimizing or enhancing performance.

1.1.1 Graphene Photodetection and Photocurrent Generation

A basic photodetector converts energy from incident photons into a measurable current or voltage signal. Graphene is a promising 2D material for photodetectors, and so much effort in the field has been attempting to understand the underlying photocurrent mechanisms. One of the more common tools used is an analysis of the photocurrent dependence on incident continuous wave laser power, as is shown in figure 1.2 borrowed from Patil 2013 [1]. Their results yield photocurrent exponents of 0.62 ± 0.05 for a graphene device supported on Si/SiO_2 substrate and 0.93 ± 0.05 for a suspended graphene device indicating that the photo-thermoelectric effect is the dominant photocurrent generation mechanism in supported devices and the photovoltaic effect is enhanced in suspended devices. Other research groups use this same technique, such as in Gaham 2012 where they also report a photocurrent exponent of 0.65 ± 0.02 in a supported graphene device [4].

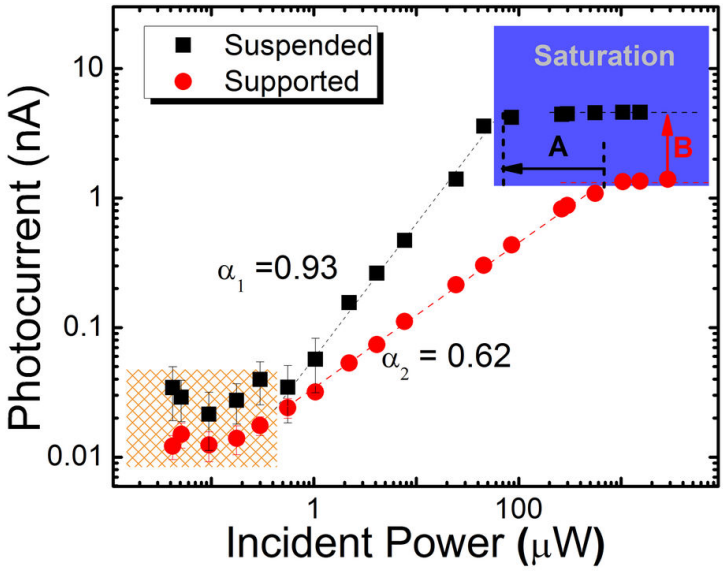

Figure 1.2: Photoresponse and photocurrent generation mechanism in supported and suspended monolayer graphene. When plotted on a logarithmic scale, the slope of the data reveals the underlying photocurrent generation mechanism. Figure borrowed from [1].

These groups argue that the hot, photo-excited electrons in supported graphene relax efficiently thanks to substrate scattering and low mobility. In suspended graphene, the enhanced mobility and lack of substrate for scattering results in enhanced heat conduction and a reduced photo-thermoelectric effect. The authors of these papers used CVD graphene, which often have high structural disorder compared to exfoliated graphene like our samples. Still, suspended devices exhibit more efficient photoresponse and a higher output current by as

much as a factor of 4, and the analysis used in these papers, which will be detailed in Chapter 2, is often used for discussing short-circuit photocurrent experiments.

The photocurrent magnitude depends both on excitation location on the graphene sample and the strength of an external electric field applied via a gate voltage, as demonstrated by Xia 2009 and shown in Figure 1.3 [5]. The photoresponse is enhanced by the gate voltage as the difference between the gate potential and the flat band potential increases. As the gate voltage changes, so too does the location of maximum photocurrent along the channel. The stronger the photocurrent magnitude becomes with V_{G}, the closer it shifts toward the source-drain electrodes. By applying large gate voltages, the authors were able to achieve a responsivity of around 1 $mA\ W^{-1}$ in a monolayer graphene device.

The common figures of merit used as a metric for photodetector performance are internal and external quantum efficiencies, responsivity, noise equivalent power, specific detectivity, lifetime of charge residing in particles, and photoconductive gain [6]. The External quantum efficiency is defined as the number of electron-hole pairs collected per second to produce a current I_{ph} divided by the number of incident photons per second, and essentially this is a measure of how much photoresponse is generated per photon impinging on the detector. Internal quantum efficiency is similarly defined, except it only consider the photons absorbed in the photodetector material. A device with a high internal quantum efficiency is efficient at converting absorbed photons into an electric current. Responsivity is defined as the photoresponse divided by the power of incident light, and can be presented in terms of photocurrent ($R_{\mathrm{ph}} = \frac{I_{\mathrm{ph}}}{P_{\mathrm{opt}}}$) or in terms of photovoltage ($R_{\mathrm{v}} = \frac{V_{\mathrm{ph}}}{P_{\mathrm{opt}}}$). Noise equivalent power is a measure of sensitivity, and is defined by the signal power which yield a signal-to-noise ration of 1 with an output bandwidth of 1 Hz, and is measured in $W\ Hz^{-1/2}$. Photoconductive gain is defined as the number of detected charge carriers per single photon: $\left(\frac{I_{\mathrm{ph}}}{q}\right)\left(\frac{1}{\phi_{\mathrm{in}}QE}\right)$.

1.1.2 Optimizing Graphene-Based Photodetectors

Other graphene-based designs can increase photodetector performance by modifying the device structure, primarily by enhancing the absorption of photons. These devices may incorporate metal-semiconductor-metal (MSM) photodetector design, suspension of graphene to reduce photothermal effects while enhancing photovoltaic effects, nanostructured edges of gold contacts resuling in plasma-assisted wave effects, and encapsulating the graphene channel in a photonic crystal cavity [7]. Heterostructure photodetector devices combine multiple

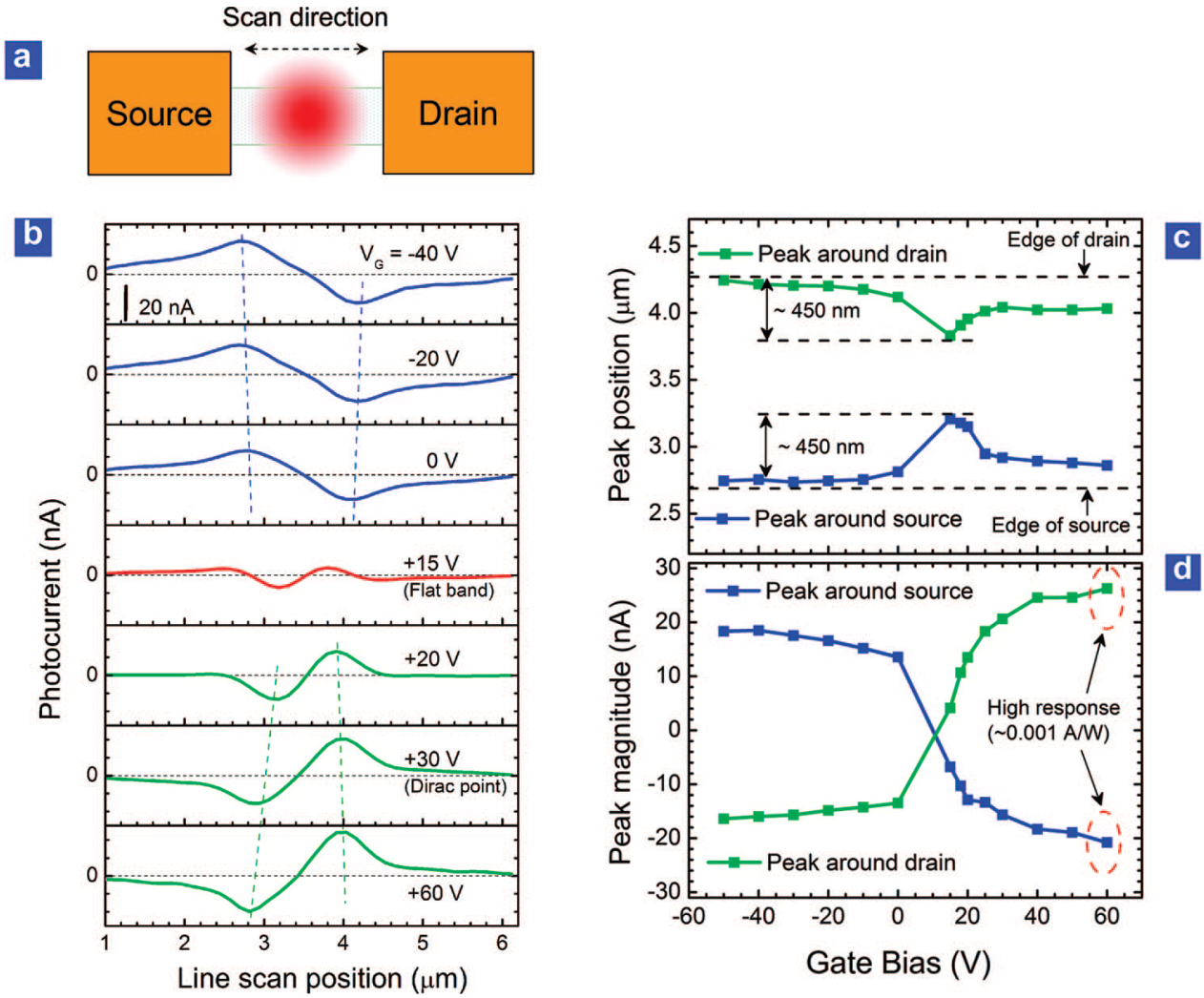

Figure 1.3: Photocurrent dependence on laser excitation location and gate voltage. (a) Illustration of a typical two-point graphene transistor, with source-drain contacts, an excitation laser spot, and labeled direction of line scans. (b) Photocurrent line scans taken at various V_G. Dashed lines indicate the shifting of the peak photocurrent position. (c) Peak photocurrent position along graphene channel as it varies with V_G. (d) Peak photocurrent acquired near the source and drain contacts at varied V_G. Dashed ellipses indicate the highest magnitude photocurrents measured, corresponding to a responsivity of about 1 $mA\ W^{-1}$. Figure borrowed from [5].

materials together in order to engineer photodetector performance. Heterostructures rely on a difference in charge carrier doping between materials creating a p-n, p^+-p^-, or n^+-n^- junction. The change in Fermi level between the two materials results in an internal electric field at their interface, such that any nearby free electron-hole pair will be swept into a current.

One example of a heterostructure is a 2-point graphene transistor whose channel varies in number of graphene layers. Shown in figure 1.4 is such a graphene device with a multilayer-monolayer-multilayer graphene configuration. The result is four junctions at each interface: two multilayer-contact and two multilayer-monolayer. AFM and Raman scans verify the number of layers, as well as demonstrate the quality and uniformity of the etched and non-etched regions. Next in figure 1.5, the authors present their results. A photocurrent image acquired at $V_{\mathrm{G}} = -40\ V$, $V_{\mathrm{B}} = 0$ (short-circuit bias), and $P_{\mathrm{opt}} = 500\ \mu W$ shows that photocurrents observed were largest when the excitation laser spot targeted near an interface, and the signage of the photocurrent is antisymmetric from one contact to the other, due to the nature of the charge density difference across each junction. Photocurrent line scans taken across the multilayer-monolayer junction at various V_{G} demonstrate that the spatial dependence changes and is particularly different and sensitive at lower gate voltages. This can be explained by the charge densities of the mono- and multi-layers evolving at different rates, such that a p-p junction may transition to an n-p junction before finally becoming an n-n^+ junction.

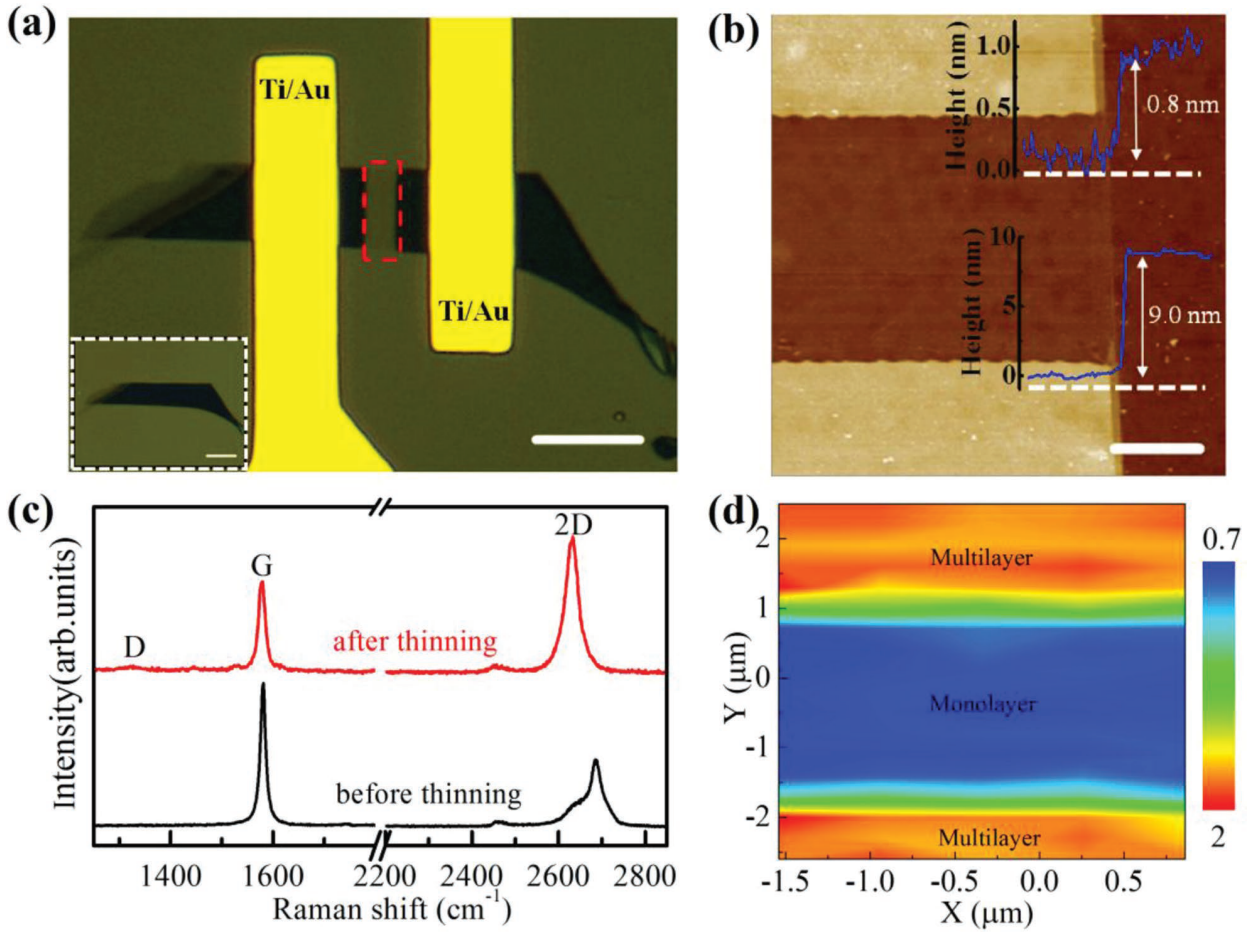

Figure 1.4: Device structure for a two-point multi-mono-multi graphene device used in Zhang 2018. (a) Optical image of graphene FET, with a monolayer region in the center and multilayer regions near the contacts, with $10\mu m$ scalebar. The monolayer region, outlined in red, was reduced from multilayer graphene using a laser thinning method. Inset shows the graphene flake before fabrication and thinning procedures. (b) AFM image of graphene device, with 10 μm scalebar. Inset height AFM height profiles show height along the dashed white lines. (c) Raman spectra of multilayer (black) and monolayer (red) regions. (d) Raman G/2D peak ratio map of the region inset in (b).
Figure borrowed from Zhang 2018 [8].

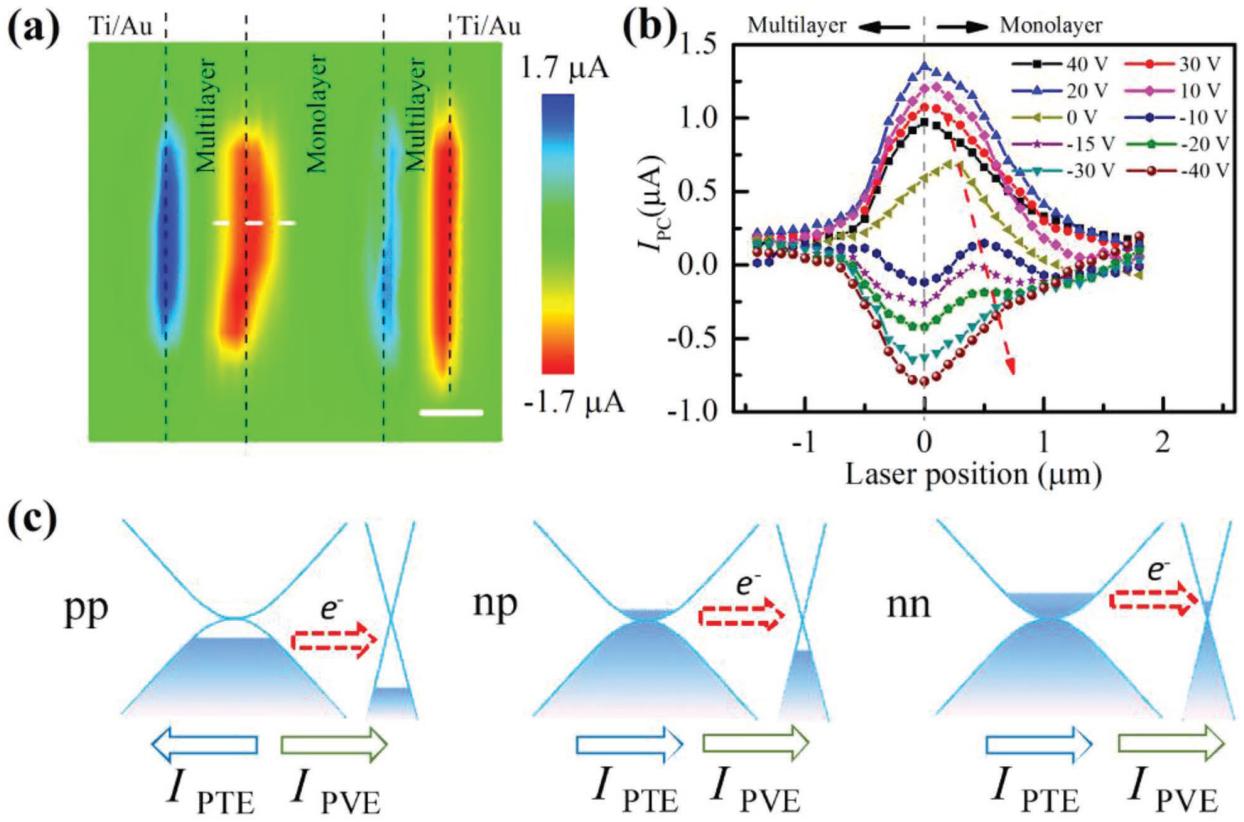

Figure 1.5: Photocurrent for graphene FET heterostructure. (a) Photocurrent image taken at $V_G = -40\,V$, $V_B = 0$ (short-circuit bias), and $P_{opt} = 500\,\mu W$. Dashed lines indicate interfaces between contact, multilayer graphene, and monolayer graphene regions. $2\mu m$ scalebar. (b) Photocurrent line scans at varied $V - G$ between $\pm 40\,V$, taken across the dashed white line in (a). The red arrow indicates the shift of a photocurrent peak away from the mono-multi interface as V_G is varied. (c) Illustration of PV and PTE mechanisms and signed contributions at varied Fermi levels controlled via V_G. Note that mono- and multi-layer graphene Fermi levels depend differently on V_G, and thus change at different rates and will intersect at some V_G. Depending on the Fermi levels in each region, the PV and PTE effects may cooperate or compete in contribution to the net photocurrent. Figure borrowed from Zhang 2018 [8].

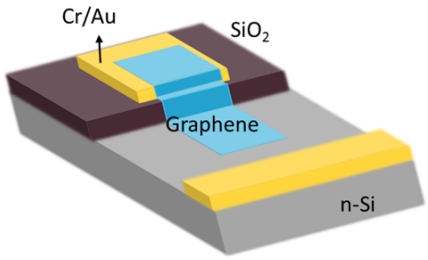

Figure 1.6: Graphene-Silicon FET heterostructure. Figure borrowed from Riazimehr 2017 [9]

While some graphene photocurrent heterostructure devices mix and match number layers of graphene, others interface graphene with various materials. The work shown in Riazimehr 2017 [9] demonstrates a graphene/silicon device configuration that yields high photoresponse. In a graphene-silicon device as illustrated in figure 1.6, the n-doped silicon will be the primary source of photo-generated charge carriers, as the absorption of Silicon is much higher than that of graphene. By applying a reverse bias of $V_{\mathrm{R}} = -2\ V$ under 950 nm excitation, the authors were able to achieve responsivities as high as 270 $mA\ W^{-1}$. The peak in photoresponsivity at $P_{\mathrm{opt}} = 950\ nm$ is due to the absorption of photons by the in the n-doped Si. The authors point out that the curve in figure 1.7 is characteristic of a typical silicon p-n junction, except for the region presented in the inset data. This comparably low photoresponse is due exclusively to charge carriers generated in the graphene, as these excitation energies are below the band gap of silicon and are attributed to the broadband light absorption of graphene (approximately 2%).

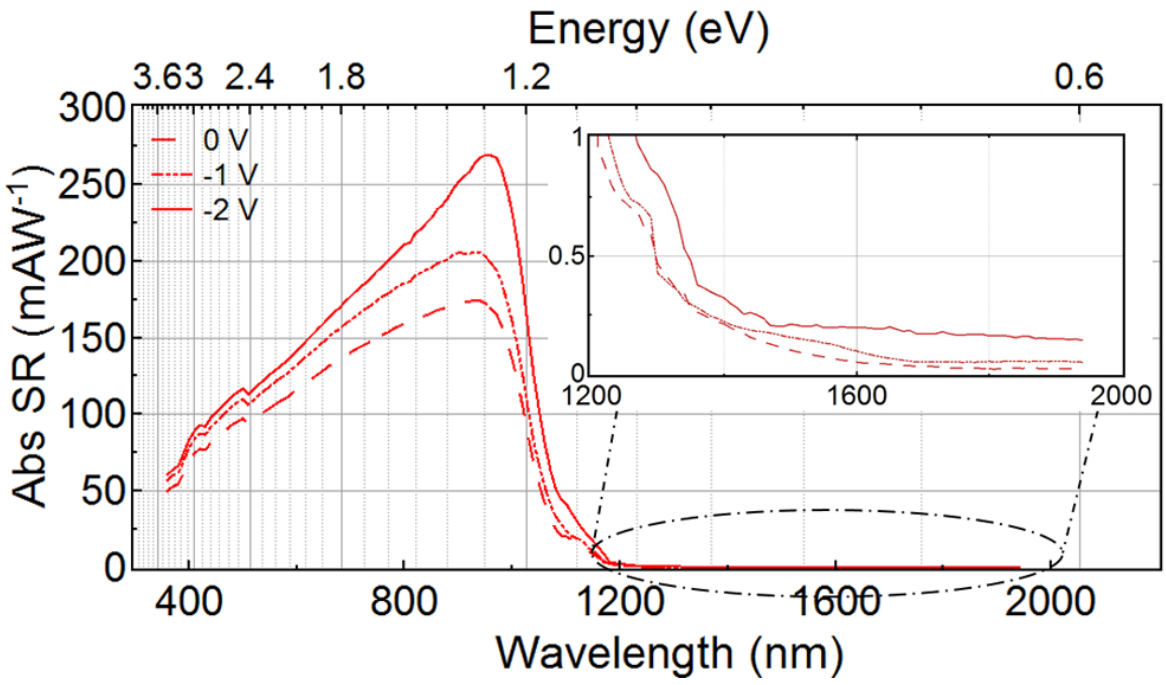

Figure 1.7: Absolute spectral response of a graphene-silicon FET at varied wavelengths. The maximum responsivity may reach as high as 270 $mA\ W^{-1}$ at 950 nm with a reverse bias of $-2\ V$. The device exhibits the behavior of a typical silicon p-n junction, except for the non-zero current shown in the inset data. Figure borrowed from Riazimehr 2017 [9]

The authors report that in such a device, the laser spot target corresponding to the largest photoresponse is at the graphene-Si interface only at low reverse bias voltage, as seen in figure 1.8. In fact for reverse bias voltage magnitudes of 1.5 V or greater, excitation on the graphene-SiO_2 interface yields significantly greater photoresponse. They explain that photogenerated electron-hole pairs generated in the graphene-Si region are much more likely to recombine while passing of the SiO_2, whereas the for high reverse bias the SiO_2 supported region is effectively gated, resulting in a greater charge density.

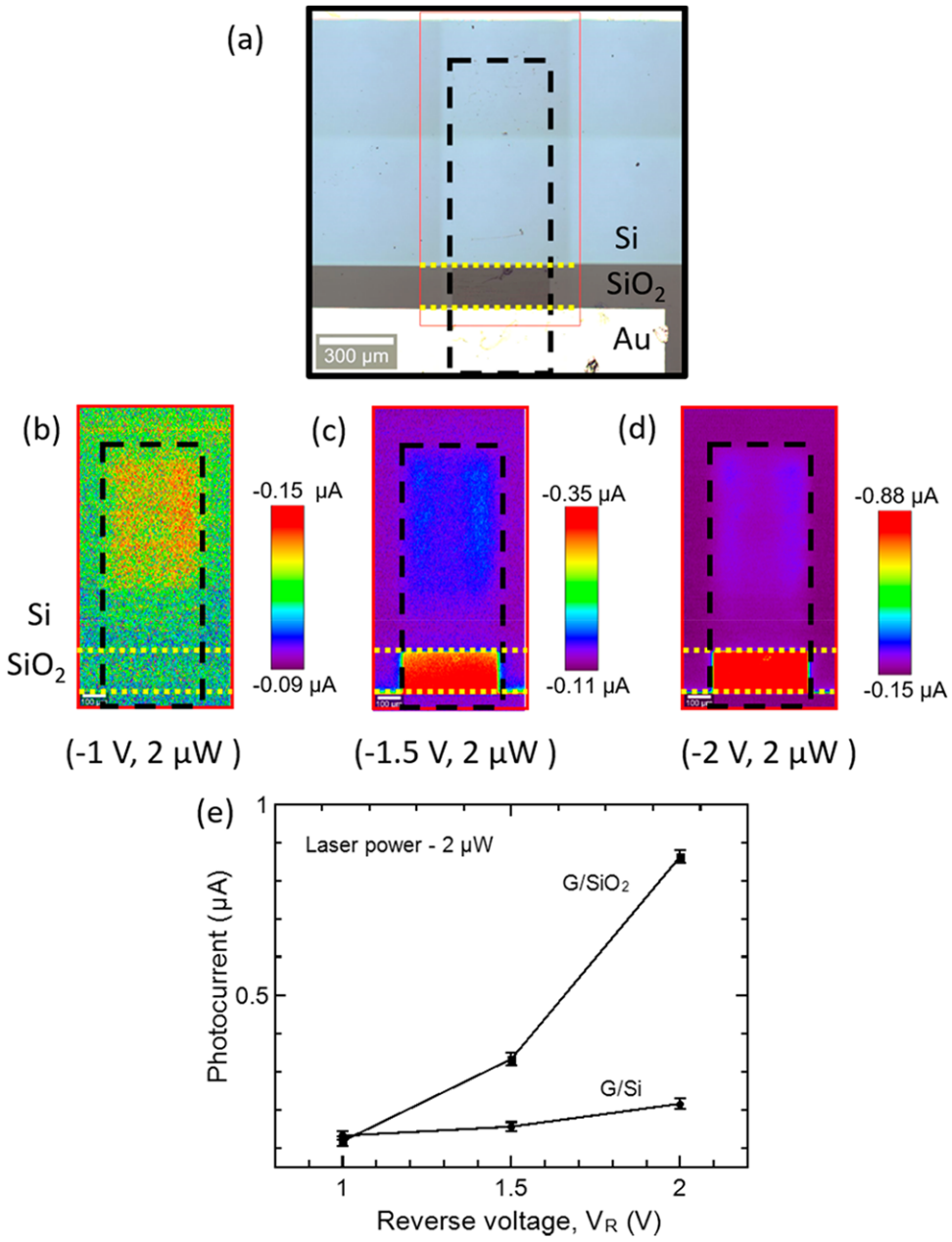

Figure 1.8: Scanning photocurrent mapping a graphene-silicon diode at varied reverse bias V_{R}. (a) Optical image of graphene-silicon diode, with labeled materials. The red rectangle indicates the region scanned during photocurrent measurements. All photocurrent maps were acquired with $P_{\mathrm{opt}} = 2\ \mu W$, with a reverse bias (b) $V_{\mathrm{R}} = -1\ V$, (c) $V_{\mathrm{R}} = -1.5\ V$, and (d) $V_{\mathrm{R}} = -2\ V$. (e) Photoresponse as a function of absolute $|V_{\mathrm{R}}| > 1$ on the graphene-Si and graphene-SiO_2 regions. Note that the response is greater in the graphene-SiO_2 region for $|V_{\mathrm{R}}| > 1$. Figure borrowed from Riazimehr 2017 [9]

1.2 Graphene: Specialized Photodetector Applications

Because graphene is sensitive to surface chemistry effects, graphene devices can be used in humidity sensing applications [10][11]. In 2017, Zhuang demonstrated the linear dependence of two-point graphene quantum dot (GQD) devices on relative humidity (RH) for RH between 10% and 90%.

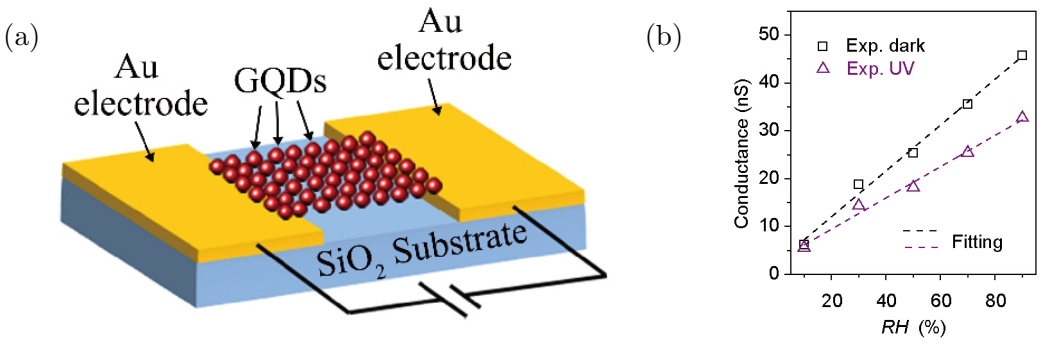

Figure 1.9: Graphene quantum dot humidity sensor. (a) Illustration of of a GQD device with bias voltage and two contacts. (b) Linear dependence of device conductance on relative humidity, measured in the dark and with UV illumination. Figure borrowed from Zhuang 2017 [11].

As shown in figure 1.9, two-point GQD devices are sensitive to RH, expressed by a change in conductance. Conductance is extracted from measured current during a bias sweep ranging from $-5\ V$ to $+5\ V$ and computing the inverse slope of current vs V_{B}. Water molecule accumulation dopes the GQD's with holes, modifying electron transport much like applying a gate voltage. Although this configuration is not sensitive to visible light, there is a notable decrease in conductance under UV illumination, with negative photoresponse to UV reaching as high as $-418.1\ \mu A\ W^{-1}$. Thus in addition to being a humidity sensor, such a device may also be used in UV sensing applications.

1.3 Thesis Structure

In this thesis, we present our photocurrent measurement instrumentation and methods for simultaneous optical and electronic measurements in micron-scale graphene transistors in ambient pressure at room temperature. We will briefly discuss how our devices are fabricated and packaged, and the most common theories describing photocurrent behavior in two-point graphene devices. With this theoretical model for photocurrent generation, we will focus on the effects of photocurrent dependence on laser power, charge density, and laser spot location.

In Chapter 2 we provide an overview of graphene, from its crystal lattice to its electronic band structure and properties via the tight binding model. We will discuss diffusive transport in graphene transistors. Next we will provide an introduction to Raman spectroscopy as a tool to investigate the crystal lattice of graphene. Finally, we outline a background for the three most prominent photocurrent generation theories: the photovoltaic (PV), photo-thermoelectric (PTE), and photo-bolometric effects.

In Chapter 3, we briefly summarize our fabrication process for creating graphene devices on Si/SiO_2 substrate. Next we discuss the design, interfacing, and synchronization of our photocurrent instrumentation, with which we perform simultaneous opto-electronic measurements. We will then detail our annealing and measurement methods.

In Chapter 4, we present our results on selected devices, including both monolayer and bilayer graphene devices. Because the electronic energy dispersion relation is different for monolayer and bilayer graphene, they exhibit distinct electron transport behaviors. Because of monolayer graphene's linear dispersion in particular, it is very sensitive to small changes in charge density, whereas bilayer graphene is more robust. We show the photocurrent vs optical power relationship and extract the photocurrent mechanism parameter β, which indicates how much each of our two main photocurrent mechanisms contribute to the total photocurrent.

In chapter 5, we summarize the key results presented in this thesis, and discuss the outlook for future experiments in opto-electronic experiments on 2D materials.

Chapter 2

Electron Transport and Photocurrent Generation in Graphene

The purpose of our investigation of illuminated graphene transistors is to understand the underlying mechanisms contributing to photocurrent. To this end, we begin by reviewing the background theory of electron transport, phonons, and photocurrent mechanisms in graphene. This theoretical framework will be used as a basis to analyze electron transport and photoresponse data in two-point graphene transistors in Chapter 4.

In this chapter, we will first illustrate the physical structure of graphene in section 2.1, as well as show its unique band structure. Next, we describe diffusive electron transport in section 2.2 Then, we will describe Raman scattering in graphene in section 2.3. We will explore the dominant mechanisms contributing to photocurrent generation at room temperature in ambient air in section 2.4. Then finally in section 2.5, we will discuss the limits of photoresponse due to the mean free path of photo-excited electrons.

2.1 Graphene Lattice and Electron Band Structure

Graphene is an ideal material to study photocurrents because of its high electron mobility, semi-metallic properties, ultrafast response times, broadband absorption, and high responsivity. Its low optical absorption of about 2.3% per layer makes it ideal for use in heterostructure devices requiring transparent contacts. Because of its lack of a band gap, graphene photodetectors are sensitive to a broad spectrum of electromagnetic radiation, especially from THz

excitation to UV light. By optically exciting graphene transistors with a laser, we can probe the physics of photocurrents in graphene.

Graphene is a two-dimensional material, whose atomic structure can be described as a sheet of carbon atoms arranged in a hexagonal, honeycomb lattice having the thickness of a single atom . Each carbon atom forms strong covalent sp^2 bonds with its 3 nearest neighbors, resulting in bond angles of 120° [12].

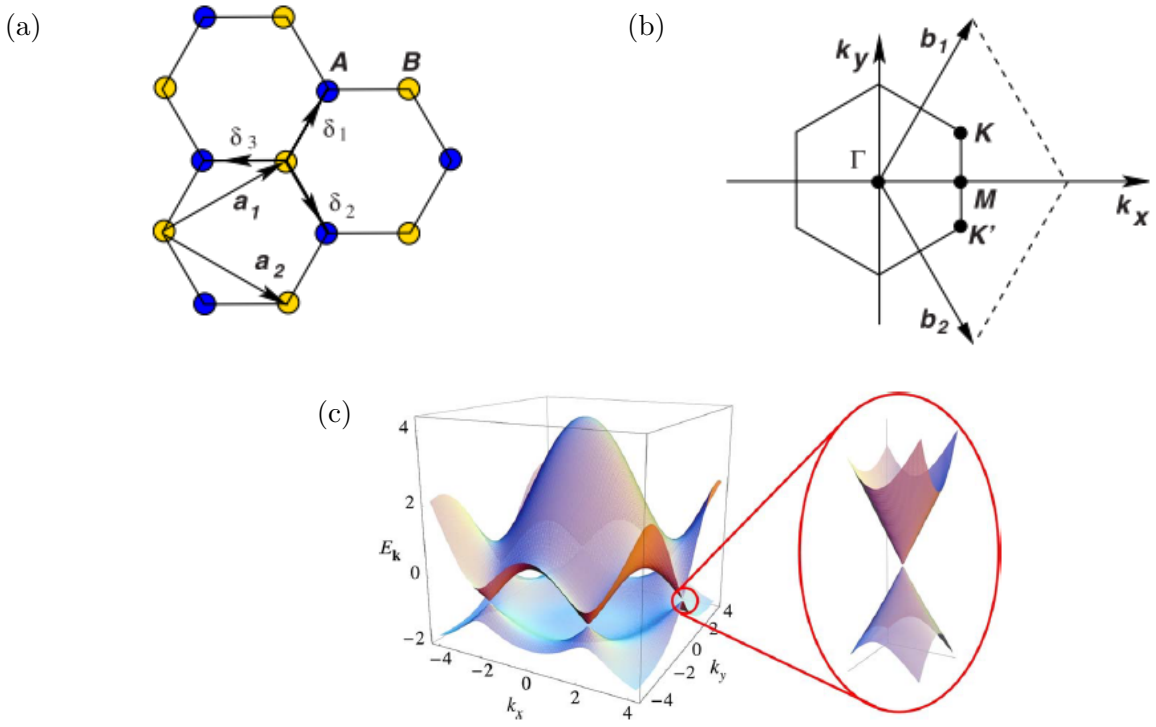

Figure 2.1: Graphene lattice structure, first Brillouin zone, and band structure. (a) Graphene lattice in real space with a 2-atom basis, with basis vectors a_1 and a_2, and nearest neighbor vectors δ_1, δ_2, and δ_3. (b) First brillouin zone of the graphene lattice, with basis vectors $\vec{b}_1$ and $\vec{b}_2$. Dirac points K and K' are indicated, as well as M and Γ points. (c) Electronic dispersion of graphene for finite nearest-neighbor hopping energy $t = 2.7\ eV$ and next nearest-neighbor hopping energy $t' = -0.2t$. Zoomed-in region shows the linear regime near the Dirac point where the electron conduction and valence bands meet but do not overlap. Figures borrowed from Castro Neto 2009 [13].

This hexagonal arrangement can be represented as a triangular lattice with a two-atom basis, shown in figure 2.1a, whose lattice vectors are

$$\vec{a}_1 = \frac{a}{2}(3, \sqrt{3}),\ \vec{a}_2 = \frac{a}{2}(3, -\sqrt{3}). \tag{2.1}$$

The nearest neighbor vectors, $\vec{\delta}_{1,2,3}$, and next-nearest neighbor vectors, $\vec{\delta'}_{1,2,3}$ are

$$\vec{\delta_1} = \frac{a}{2}\left(1, \sqrt{3}\right),\ \vec{\delta_2} = \frac{a}{2}\left(1, -\sqrt{3}\right),\ \vec{\delta}_3 = -a\,(1, 0)\,, \tag{2.2}$$

$$\vec{\delta'}_1 = \pm\vec{a_1},\ \vec{\delta'_2} = \pm\vec{a_2},\ \vec{\delta'_3} = \pm\left(\vec{a_2} - \vec{a_1}\right). \tag{2.3}$$

where a is the lattice constant [13]. The Dirac points, as seen in the first Brillouin zone in figure 2.1b, are then described by

$$\vec{K} = \left(\frac{2\pi}{3a}, \frac{2\pi}{3\sqrt{3}a}\right),\ \vec{K'} = \left(\frac{2\pi}{3a}, -\frac{2\pi}{3\sqrt{3}a}\right). \tag{2.4}$$

The tight-binding model for graphene assumes that electrons can hop between nearest-neighbors, and even next-nearest neighbors [13]. The Hamiltonian for electrons in this system is

$$H = -t\sum_{\langle i,j\rangle,\sigma}(a^{\dagger}_{\sigma,i}b_{\sigma,j} + H.c.) - t'\sum_{\langle\langle i,j\rangle\rangle,\sigma}(a^{\dagger}_{\sigma,i}a_{\sigma,j} + b^{\dagger}_{\sigma,i}b_{\sigma,j} + H.c.), \tag{2.5}$$

where a ($a^{\dagger}$) is the creation (annihilation) operator at site $\mathbf{R}_i$ of sublattice A, σ is electron spin, and the nearest-neighbor hopping energy t is taken to be 2.8 eV [13]. From this Hamiltonian, the derived energy bands are then [13]:

$$E_{\pm}(\vec{k}) = \pm t\sqrt{3 + f(\vec{k})} - t'f(\vec{k}). \tag{2.6}$$

For monolayer graphene, the Fermi level can then be calculated according to

$$E_{\mathrm{F}} = sign(\Delta V_{\mathrm{G}})\hbar\nu_{\mathrm{F}}\left(\alpha\pi|\Delta V_{\mathrm{G}}|\right)^{1/2}, \tag{2.7}$$

where ΔV_{G} is the gate voltage relative to the Dirac point voltage, $\hbar$ is the reduced Planck's constant ($1.05 \times 10^{-34}\ m^2\ kg\ s^{-1}$), ν_{F} is the Fermi velocity , and α is the gate capacitance in an electron charge ($7.1 \times 10^{10}\ cm^{-2}$) [14]. The Dirac point voltage is the gate voltage at which graphene conductivity is minimized and there are zero charge carriers induced by the gate, hence why it is also called the charge neutrality point. The electronic dispersion is visualized in figure 2.1c, where for very low Fermi energy the dispersion is linear. For bilayer graphene the Fermi level can be calculated according to

$$E_{\mathrm{F}} = \frac{\hbar^2\pi\alpha\Delta V_{\mathrm{G}}}{2m^*}, \tag{2.8}$$

where m^* is the effective electron mass ($m^* = 0.033m_e = 0.033\times9.11\times10^{-31}kg$) [14]. Plotting equations 2.7 and 2.8 in figure 2.2, it becomes clear that small changes in gate voltage result in a much greater change in monolayer graphene than in bilayer near the Dirac point.

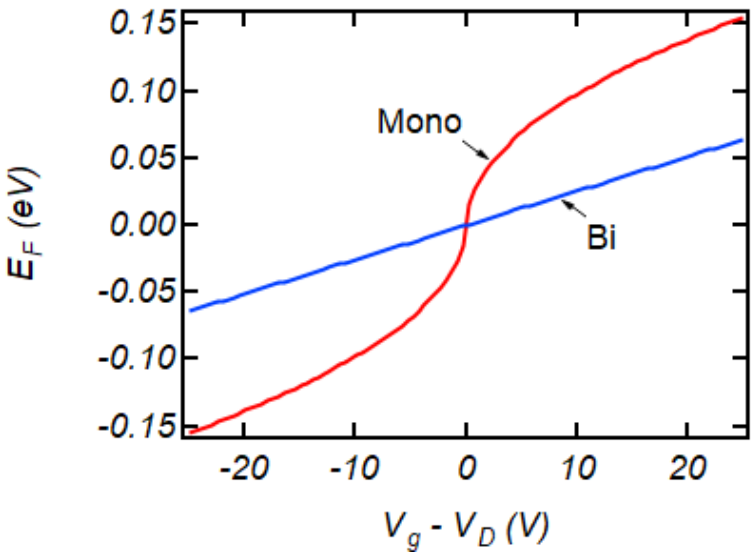

Figure 2.2: Fermi level of graphene as a function of gate voltage for monolayer and bilayer graphene. Note that near the Dirac point, small changes in V_{g} result in much larger changes in E_{F} for monolayer than for bilayer graphene.

2.2 Diffusive Electron Transport

When the mean free path of an electron in graphene is much longer than the length of the device, then electron transport is in the ballistic regime. However, in our experiments we extract mean free paths of a no more than 200 nm at room temperature, compared to channel lengths of several microns. Therefore an electron traveling through the channel will experience many collisions, as illustrated in figure 2.3, and thus are in the diffusive regime.

Surface contaminants, such as ambient moisture or residual polymers used during the fabrication process, will hinder electron transport performance in graphene transistors. Some surface contaminants may be removed using a laser annealing technique [16]. At sufficiently high laser power exposure, polymers can be burned permanently off. However, adsorbed water can only be temporarily removed via laser annealing provided that the graphene surface is still exposed to room temperature and pressure.

As shown in figure 2.4a, increasing relative humidity results in a greater conductivity for a graphene device. In fact the conductance increases linearly with increasing humidity which can be seen in figure 2.4c. The mechanism proposed in literature is that polar surface water molecules attract electrons at the graphene surface, trapping them, as is illustrated in figure 2.4b. This trapping changes the charge density in the graphene channel, effectively gating

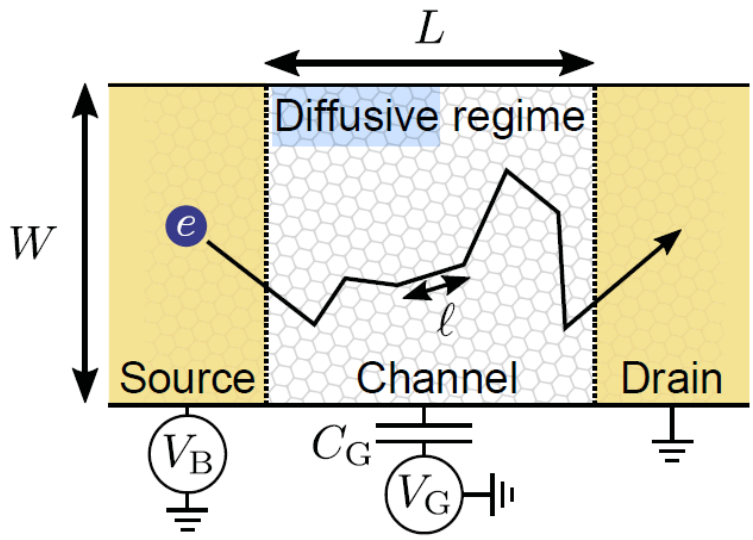

Figure 2.3: Diffusive electron transport in a two-point graphene transisor. Because the electron mean free path ℓ is much shorter than the channel length L, an electron will experience many collisions traveling from source to drain electrodes. Figure borrowed from McRae 2018 [15].

the graphene and doping it with holes. Thus for increased moisture content we would expect to see the Dirac point shift in the positive gate voltage direction, a feature observed in our own measurements which will be presented in chapter 3. [11].

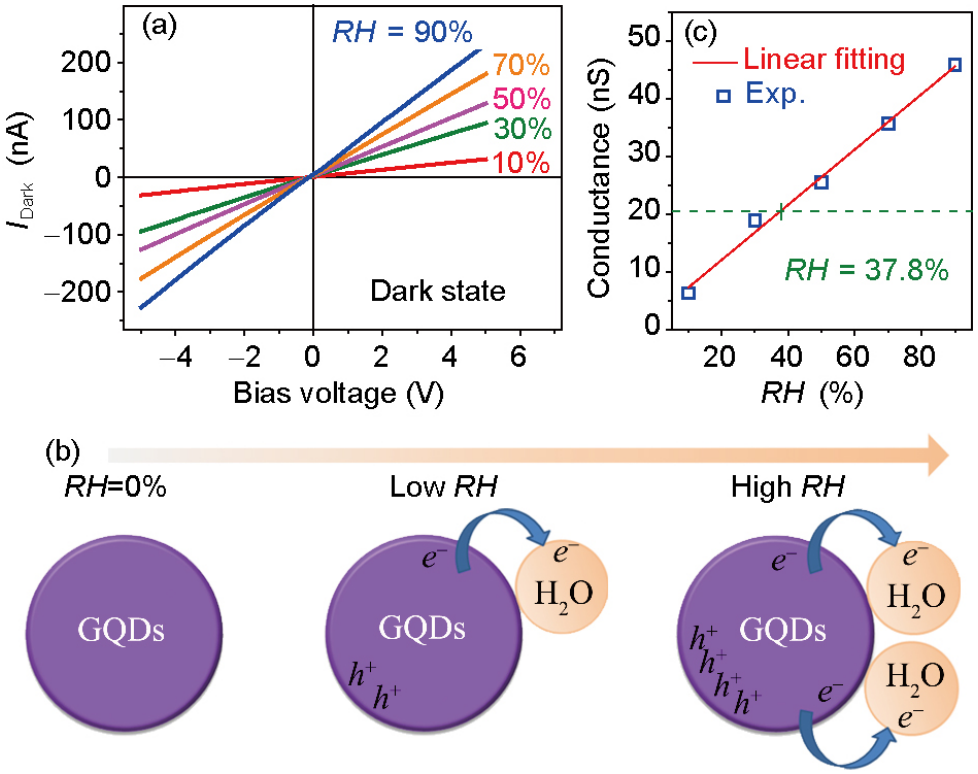

Figure 2.4: Effect of adsorbed moisture on electron transport in graphene. (a) Bias sweeps at various bias voltages, demonstrating that increased humidity results in an increase in conductivity. (c) Increased relative humidity corresponds to a linear increase in measured current and conductance at constant biase voltage. (b) Cartoon illustrates how adsorbed water molecules effectively gate the graphene, modifying its charge density. Figures borrowed from Zhuang 2017 [11].

2.3 Raman Spectroscopy on Graphene

When a photon is incident on a solid material, it will either pass through without interaction, or it will interact through absorption, reflection, emission of light, or scattering. The probability that a photon will undergo any one of these processes depends on the energy of the photon and on the material's electronic and vibrational properties. When a material absorbs a photon of energy greater than the band gap of the material, the photon may excite an electron transition from the valence band to the conduction band, thus creating an electron-hole pair. The e-h pair may contribute to a current in the sample (photocurrent), or recombine by emitting a photon (photoluminescence). Even in the absence of absorption, matter can interact with light via scattering. Upon interacting with a phonon in the crystal lattice, a photon may scatter elasticly (conserve energy) or inelasticly (gain/lose energy from/to the phonon) [17].

Raman spectroscopy can be used to identify samples and quantify their characteristics. Most incident light is Rayleigh scattered, but about 10^{-6} of the initial power will Raman shift as the photons interact with the molecular vibrational energy levels [18]. Infrared bands are due to photon interacting with oscillating dipole moment of vibrating molecule. Raman comes from photons interactiing with polarizability ellipsoid of a vibrating molecule, inducing an oscillating dipole. To picture it, consider the polarizability ellispoid to be the shape of the electron cloud surrounding the molecule. Raman intensity will be increased for symmetric bonds, increased number of bonds, and for heavier atoms. Raman intensity will also depend on concentration level, matrix or solution, other interfering molecules present, and sampling method [18].

Illustrated in figure 2.5a, light is focused on a sample and one of the photons is shown to interact with the lattice. This photon may interact according to one of the three scattering mechanisms, pictured in 2.5b, where the photon may red shift and lose energy (Stokes Raman scattering), blue shift and gain energy (Anti-Stokes Raman scattering), or experience no change in wavelength and energy (Rayleigh scattering). The energy of the shift is the energy of the phonon created or annihilated in the lattice, and is directly related to the energy of of atomic bonds in the lattice. Because the energy shift comes from the symmetry and strength of atomic bonds, Raman active materials can be uniquely identified by their Raman spectra. For example, C-O and C-H bonds have characteristic vibrational state energies, which can be measured by the change in energy of an incident photon, as shown in figure 2.5c.

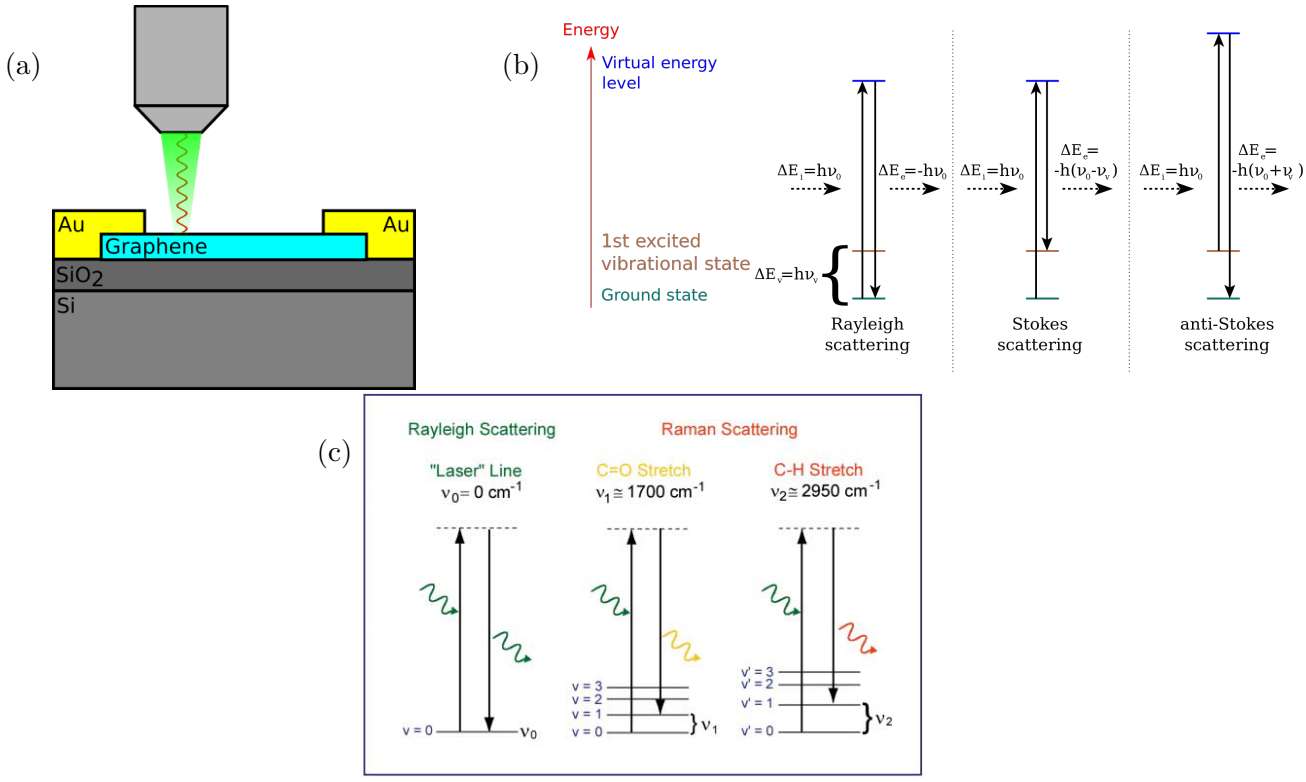

Figure 2.5: Raman excitation and vibrational energy state transitions. (a) Illustration of a typical graphene transistor under focused laser illumination. A fraction of incident light is Raman shifted (b) Diagram distinguishing Rayleigh, Stokes, and anti-Stokes Raman scattering processes. When a photon is absorbed within a crystal lattice, it may scatter with the same wavelength (Rayleigh), donate energy to the lattice and be re-emitted with a longer wavelength (Stokes Raman scattering), or accept energy from the lattice and be re-emitted at a shorter wavelength (Anti-Stokes Raman scattering). (c) The photon energy lost during inelastic scattering is equal to the energy of the vibrational mode of the molecular bond with which it interacted. Molecular bonds and bulk materials can be identified according to the energy shift of the re-emitted photons. Subfigure c borrowed from InPhotonics 1999 [18].

In the case of Raman scattering, a phonon is either created or annihilated in the process of scattering, and thus the re-emitted photons energy does not equal that of the absorbed photon. In other words, light scatters inelasticly. [17]. The incoming photon's electric field will cause the electron and carbon atoms to oscillate oppsite each other, forming a dipole. The stable geometry of the chemical bond for an excited electron is different than for an electron in the ground state, and thus the electron, excited by the photon to a virtual state, and its carbon atom must spatially adjust to a new equilibrium position [17].

The energy and momentum of the system must be conserved, therefore

$$E_{\mathrm{s}} = E_{\mathrm{i}} \pm E_{\mathrm{q}} \tag{2.9}$$

$$k_{\mathrm{s}} = k_{\mathrm{i}} \pm k_{\mathrm{q}} \tag{2.10}$$

where E_{s} is the re-emitted photon energy, E_{i} is the incident laser photon energy, and E_{q} is the scattered phonon energy. k represents the momentum of the of the incident photon, emitted photon, and phonon. The equations above are for Stokes Raman if $-$, Anti-Stokes if $+$.

The order of the Raman process is defined by the number of scattering events involved. First-order Raman scattering creates a single phonon of small momentum ($q \approx 0$), and second-order Raman involves 2 scattering events. For double resonant Raman, the $q \approx 0$ restriction is lifted, and an may scatter from k to $k + q$, then scatter back to its initial position with a phonon of wavevector $-q$, thus allowing the electron-hole pair to recombine [17].

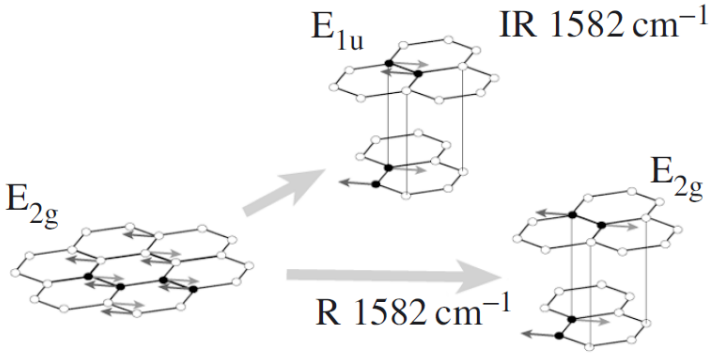

Figure 2.6: First order $E_{2\mathrm{g}}$ mode in mono- and bi-layer graphene. Illustration shows the direction of the antisymmetric vibrations responsible for creating the Raman G. The mode is active in both infrared and Raman spectroscopies, and is responsible for the red-shifted G-peak with a photon energy of about $1,582\ cm^{-1}$. Figure borrowed from Reich 2004 [19].

In graphene there are 3 optical phonons and 3 acoustic phonons, however only the longitudinal (LO) and transverse (TO) optical phonons of pristine graphene are Raman active [19]. These two are in-plane vibrations with an energy of 1582 cm^{-1} for which the basis atoms travel in opposite directions, and are often referred to as the doubly degenerate E_{2g} phonon eigenvector, as shown in figure 2.6. The E_{2g} phonon has a characteristic energy of 1582 cm^{-1}, and composes the G-peak seen in graphene Raman spectra.

The Raman D peak at about 1350 cm^{-1} arises from zone-boundary phonons, and is only present in Raman spectra at edges or when there are defects present in the lattice [20]. This is because they only satify the Raman fundamental selection rule when lattice symmetry is broken. Thus the D peak can be used to quantify disorder in graphene samples. However the 2nd order zone-boundary phonons do satisfy the Raman selectrion rule, and are responsible for the prominent Raman 2D peak found near 2700 cm^{-1} [20].

Raman spectra are sensitive to crystal properties, such as strain, temperature, doping and defects, and external electric fields. The Raman G peak is known to shift with temperature linearly, with a coefficient of $\chi = -(0.016 \pm 0.002)\ cm^{-1}\ K^{-1}$ for monolayer, $\chi = -(0.015 \pm 0.006)\ cm^{-1}\ K^{-1}$ for bilayer, and $\chi = -(0.011 \pm 0.002)\ cm^{-1}\ K^{-1}$ for bulk highly-ordered pyrolytic graphite (HOPG) given a 488 nm excitation wavelength [21][22]. The phonon softens as temperature is increased, which will be important to consider as we conduct our experiments because the laser spot will act as a heat source as high optical power. By monitoring the shift in G peak during acquisitions at varied optical power, we can see at what power there is negligible laser-induced heating of the sample.

Monolayer and bilayer graphene can be distinguished by the shape of the 2D peak and the height of the 2D peak with respect to the G peak. As shown in figure 2.7, both monolayer and bilayer graphene exhibit Lorentzian shape G peaks. However in monolayer samples the 2D peak is much taller than the G peak, whereas for bilayer graphene the 2D peak is not much taller than the G peak and is broader, composed of a superposition 4 Gaussians. Additionally the 2D peak in bilayers and is noticeably red-shifted compared to in monolayer. Thus mono- and bi-layer samples qualitatively distinguished using Raman spectroscopy.

Raman spectra can also quantitatively disambiguate monolayer from multilayer, and clearly distinguish bilayer from trilayer simply by comparing the height of the G and 2D peaks. The ratio of G and 2D peak height is dependent on the number of layers of graphene, as seen in figure 2.8. Although G/2D ratios reported are often simple peak height comparisons, our method described in chapter 3 and employed in chapter 4 takes the integrated area ratios from

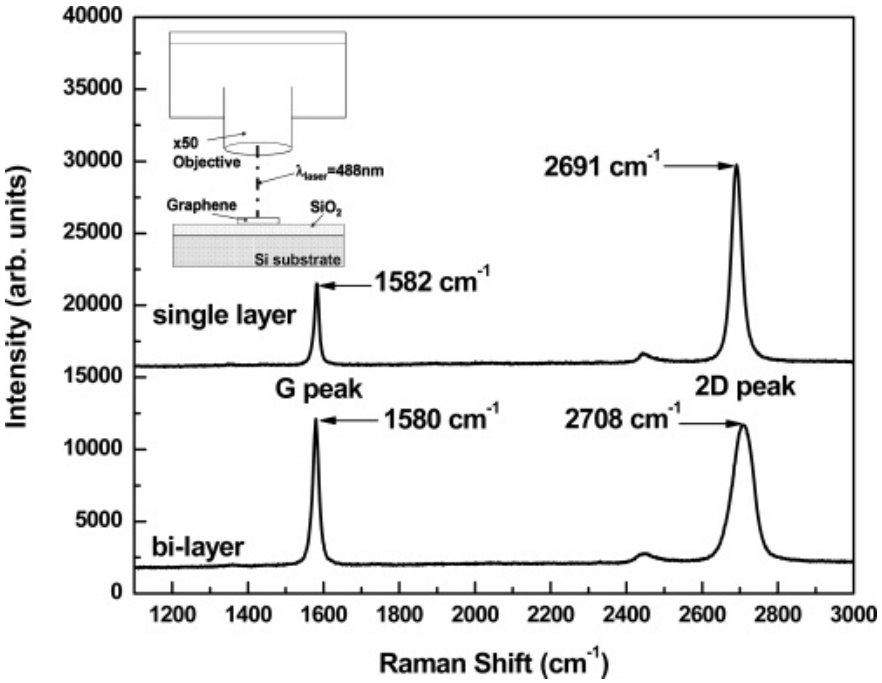

Figure 2.7: Comparison of Raman spectra in monolayer and bilayer graphene. The G peak phonon is softer by 2 cm^{-1} in bilayer compared to monolayer, but both share a Lorentzian line shape. The 2D peak, in additiion to a peak center shifted up by about 17 cm^{-1}, is much broader than in monolayer and is composed of a superposition of four Gaussians. Figure borrowed from Calizo 2007 [21].

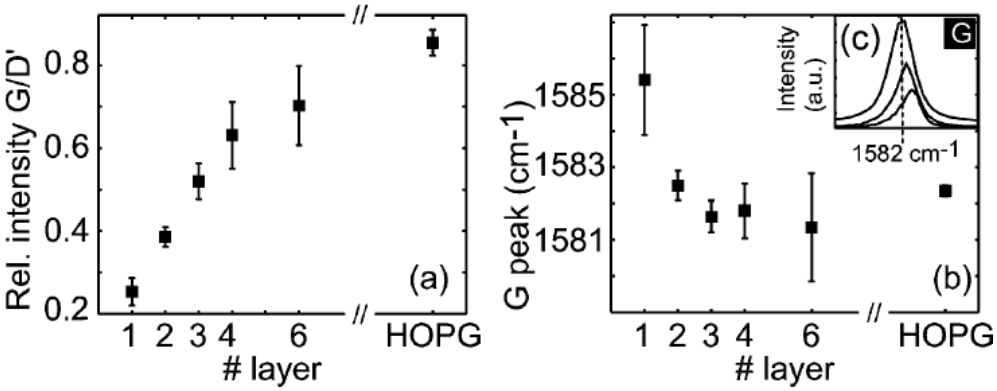

Figure 2.8: Raman G/2D ratio and G-peak center in graphene as a function of number of layers. Figures borrowed from Graf 2007 [23]. Mono-, bi-, and multi-layer graphene can be distinguished by the G/2D peak ratio of their Raman spectra. The Raman G peak of multi-layer graphene is softer than in monolayer by at least a few cm^{-1}.

line fits because it reduces uncertainty from the background noise. However it does result in different values from the reference figure provided, and thus the expected values of G/2D for our method will be about 0.11 and 0.21 for monolayer and bilayer respectively.

As previously mentioned, we can use Raman spectroscopy to quantify lattice defects. The Raman D-peak is activated by structural disorder, arising from missing atoms, grain boundaries, edges, presence of foreign atoms, and the like. From the extracted areas under the D and G peaks from fits, the inter-defect distance, or average distance between defects, can be calculated:

$$L_{\mathrm{D}} = \sqrt{\frac{(4.3 \times 10^3\ nm^2\ eV^4)}{E_{\mathrm{L}}^4} \left(\frac{I_{\mathrm{D}}}{I_{\mathrm{G}}}\right)^{-1}}, \tag{2.11}$$

where $I_{\mathrm{D,G}}$ are the integral area intensities for the D and G peaks and E_{L} is the photon energy of the laser excitation. It should be noted that this form of the equation applies when defects are sparse and the D peak height is much less than that of the G peak, which is normally the case for mechanically exfoliated graphene such as our samples. From the interdefect distance we can then calculate the structural defect density [24][25][26]:

$$n_{\mathrm{D}} = \frac{1}{\pi L_{\mathrm{D}}^2}. \tag{2.12}$$

From the energy time uncertainty relationship, we can estimate the phonon lifetimes from the width of a Raman peak:

$$\tau = \frac{\hbar}{\Gamma}, \tag{2.13}$$

where Γ is the phonon FWHM, and $\hbar$ is Planck's constant taken to be 5.3 $cm^{-1}\ ps$. Because the measured linewidths are dependent on spectrometer slit width, this should yield a lower-bound estimate unless the width is taken to be the zero-slit width limit [27].

2.4 Photocurrent Generation in Graphene

Photocurrent is the flow of electrons produced in a medium in response to photoexcitation. In graphene the mechanisms of photocurrent generation are not fully understood, and there have been many attempts to disambiguate the proposed mechanisms. In particular there are five competing explanations: photovoltaic, photo-thermoelectric, bolometric, photogating, and plasma wave-assisted effects.

2.4.1 The Photovoltaic Effect

The photovoltaic effect mechanism describes the separation of photogenerated electron-hole pairs at a p-n junction. For a graphene field-effect transistor, such a junction could be an interface between the graphene channel and a contact, the interface between the graphene channel and another material in a heterostructure, or the interface between a monolayer and a bilayer region of graphene [6][28].

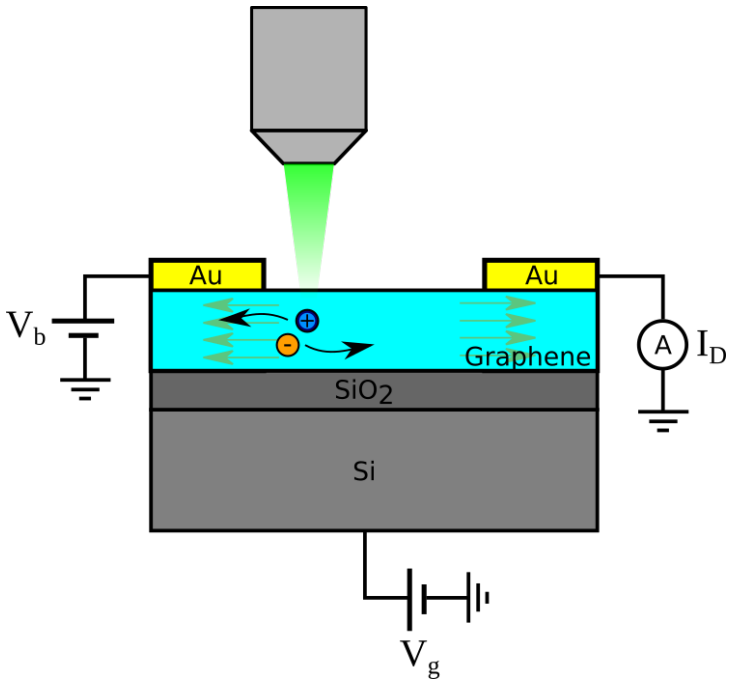

Figure 2.9: Illustration of the photovoltaic effect. Incident photons excite electron-hole pairs which are then carried away by the built-in electric field due to difference in Fermi level between the contacted and exposed regions of the graphene-metal interface.

In our devices the junction is between the graphene channel, and the graphene beneath the gold contacts, as illustrated in figure 2.9. At this interface is a built-in electric field created by the difference in chemical potential between the two sides. The Fermi level of the metal is pinned, but the Fermi level of the graphene is tunable via an applied gate voltage which creates an orthogonal electric field. When a photon interacts with an electron, exciting it from the valence band to the conduction band, it creates an electron-hole pair. If the electron (hole) is close enough to (within the mean free path of) the built-in electric field, then the electron (hole) is carried away by the electric field, resulting in a current. This essentially creates additional carriers for electric current, resulting in additional conductance in the channel. Because the built-in electric field is tunable via the gate, then so is the magnitude

of the resulting photocurrent. Modeling the device as a capacitor, the change in the Fermi level as a function of applied gate voltage for monolayer graphene is

$$\Delta E = \hbar \nu_{\mathrm{F}} \sqrt{\frac{\pi C_{\mathrm{G}} \Delta V_{\mathrm{G}}}{e}}, \tag{2.14}$$

where ν_{F} is the Fermi velocity, C_{G} is the capacitance per unit area, and $\Delta V_{\mathrm{G}} = (V_{\mathrm{G}} - V_{\mathrm{D}})$.

The photocurrent due to the photovoltaic effect can be described by

$$I_{\mathrm{PV}} = q\eta\beta \left(\frac{P_{\mathrm{opt}}}{h\nu} \right) \frac{(\mu_{\mathbf{n}} + \mu_{\mathrm{p}})}{A_{\mathbf{Laser}}} \frac{W}{L}, \tag{2.15}$$

$$I_{\mathrm{PV}} \propto P_{\mathrm{opt}} \tag{2.16}$$

where q is the elementary charge, η is quantum efficiency of the photodetector layer, β is the efficiency of generating an electron-hole pair, P_{opt} is the incident laser power, $h\nu$ is the energy of an incident photon, $\mu_{\mathrm{n,p}}$ is the mobility of electrons (n) or holes (p), A_{Laser} is the area illuminated by the laser, and $\frac{W}{L}$ is the device aspect ratio [1].

The photovoltaic contribution to photocurrent may also be calculated from the change in conductivity due to optical excitation:

$$I_{\mathrm{PV}} = \gamma A e \mu \Delta E = \gamma A \Delta \sigma E, \tag{2.17}$$

$$\Delta \sigma = \Delta n e \mu, \tag{2.18}$$

where γ is the internal quantum efficiency and A is the cross-sectional area of the illuminated region [28].

From this it can be shown that

$$\sigma = \frac{L}{W} \frac{2q^2}{h} \frac{2W}{\pi \hbar \nu_{\mathrm{F}}} T \left(\int_0^\infty dE \frac{1}{1 + e^{(E+E_{\mathrm{F}})/kT}} + \int_0^\infty dE \frac{1}{1 + e^{(E-E_{\mathrm{F}})/kT}} \right), \tag{2.19}$$

where $T = \frac{\lambda}{\lambda + L}$ is the transmission coefficient and λ is the mean free path [28]. Note that the photoresponse depends on the photon wavelength, giving a greater response for shorter wavelengths.

2.4.2 The Photo-Thermoelectric Effect

The thermoelectric effect is the generation of a voltage across a device due to a difference in both the Seebeck coefficient and electronic temperature across a junction. Such a junction may be a contact interface between two materials (graphene-gold), between differently-doped regions of graphene (p-n or p-p^+), or between regions of graphene which differ in number of layers. As illustrated in figure 2.10, an incoming photon excites an electron, creating an electron-hole pair. The temperature of the electron is highly elevated, much more than that of the lattice, resulting in an electronic temperature gradient across the junction. Because electrons are hot and relaxation through phonons is limited, electrons maintain extra momentum and may diffuse farther. Similar to the photovoltaic effect, the photo-thermoelectric effect depends on the built-in electric field across the junction. Photogenerated carriers are swept across the junction by this built-in field, resulting in an electronic current. [28] [6].

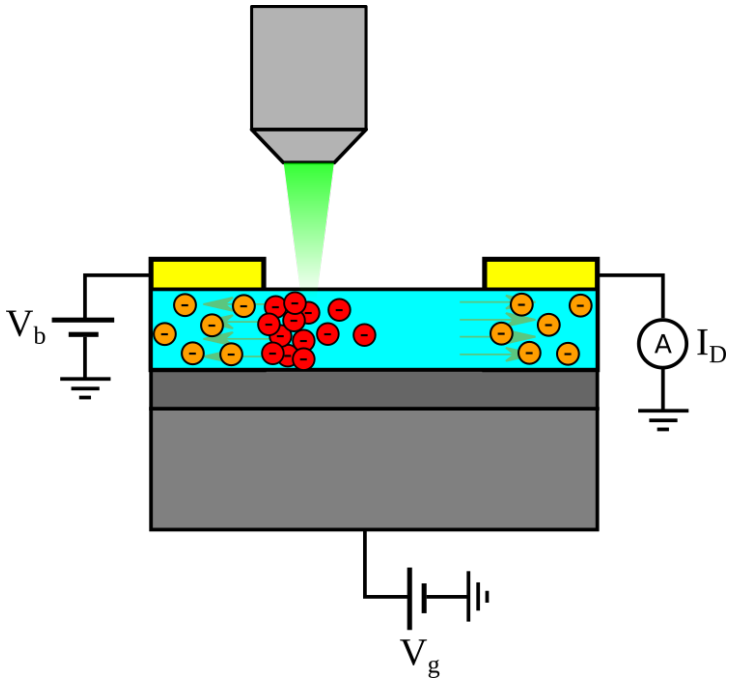

Figure 2.10: Illustration of the photo-thermoelectric effect. Electrons excited by an incident laser also experience an increase in temperature. These hot electrons may diffuse farther than cool electrons. A difference in Fermi level between the contact-covered (pinned by the contacts) and exposed channel (modulated via externally applied gate voltage) graphene regions results in a built-in electric field. Electrons beneath the contacts are thermalized with the lattice, but those in the illuminated channel are elevated above that of the lattice. This difference in temperature combined with the built-in electric field results in a flow of charge.

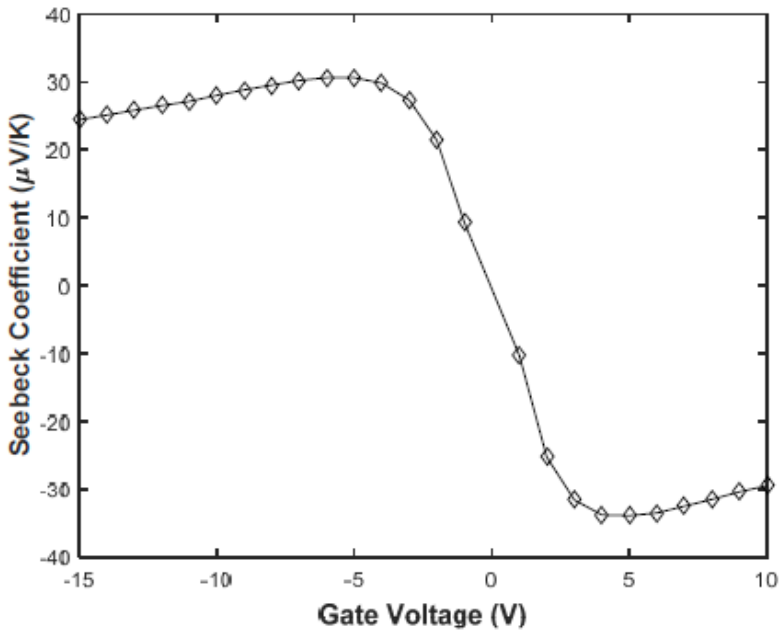

Figure 2.11: Calculated Seebeck coefficient for monolayer graphene, plotted equation 2.21. The laser radiation is treated as a heat source incident on the graphene channel. The temperature difference between illuminated and non-illuminated regions is $\Delta T = \frac{P\alpha}{k_{\mathrm{T}} 2\pi d}$, where $k_{\mathrm{T}} = 5 \times 10^3\ W\ m^{-1}\ K^{-1}$ is the monolayer thermal conductivity of graphene, $d = 3\ \mathring{A}$ is graphene thickness, P is the incident laser power, and $\alpha = 2.3\ \%$ is the monolayer absorption coefficient. Figure borrowed from [28].

The magnitude of photocurrent induced by the photo-thermoelectric effect can be controlled by adjusting the gate voltage. The photo-thermoelectric voltage across the junction is described by

$$V_{\mathrm{PTE}} = \int S \cdot \Delta T_{\mathrm{e}}\ dx \approx \Delta S \Delta T_{\mathrm{e}}, \tag{2.20}$$

where S is the Seebeck coefficient (thermoelectric power coefficient), ΔT_{e} is the electronic temperature gradient across the junction. The Seebeck coefficient for monolayer graphene, plotted in figure 2.11, can be calculated according to

$$S = \frac{\pi^2 k^2 T}{3q} \frac{1}{G} \frac{\partial G}{\partial V_{\mathrm{G}}} \frac{\partial V_{\mathrm{G}}}{\partial E}\bigg|_{\mathrm{E}=E_F}, \tag{2.21}$$

where G is conductance, q is the fundamental charge, k is the Boltzmann constant, and T is temperature [28].

The photocurrent due to the photothermoelectric effect can then be calculated according

to

$$I_{\mathrm{PTE}} = \frac{(S_1 - S_2)\,\Delta T_{\mathrm{e}}}{R} = \frac{2\pi e k_{\mathrm{b}} T}{3h} \Delta T \left(\frac{dT}{dE}\right)_{E_{\mathrm{F}}}, \tag{2.22}$$

where $S_{1,2}$ are the thermoelectric power (Seebeck) coefficients for naked and contacted regions of graphene, and ΔT_{e} is the electron temperature elevation above the lattice temperature [1][28]. $\Delta T = \frac{P\alpha}{k_{\mathrm{T}} 2\pi d}$, where $k_{\mathrm{T}} = 5 \times 10^3\ W\ m^{-1}\ K^{-1}$ is the monolayer thermal conductivity of graphene, $d = 3\ \mathring{A}$ is graphene thickness, P is the incident laser power, and $\alpha = 2.3\ \%$ is the monolayer absorption coefficient.

As we have already seen, $S \propto T_{\mathrm{e}}$. Now we consider that the number of incident photons which actually contribute to electron heat is proportional to the power of incident light: $C_{\mathrm{e}} T_{\mathrm{e}} \propto P_{\mathrm{opt}}$, where C_{e} is electronic heat capacity.

$$C_{\mathrm{e}} \propto T_{\mathrm{e}}^2 \tag{2.23}$$

$$T_{\mathrm{e}}^3 \propto P_{\mathrm{opt}} \Rightarrow T_{\mathrm{e}} \propto P_{\mathrm{opt}}^{1/3} \tag{2.24}$$

$$I_{\mathrm{PTE}} \propto S(T) \times \Delta T_{\mathrm{e}} \tag{2.25}$$

$$I_{\mathrm{PTE}} \propto P_{\mathrm{opt}}^{2/3} \tag{2.26}$$

where P_{opt} is the incident laser power. [1]

The change in temperature within the graphene lattice due to laser excitation can be described by the following equation for monolayer graphene:

$$k_{\mathrm{T}}^2 \pi d \Delta T = P\alpha, \tag{2.27}$$

where k_{T} is the thermal conductivity of monolayer graphene (about $5 \times 10^3\ W\ m^{-1}\ K^{-1}$ at room temperature), d is the thickness of monolayer graphene (about 3 $\mathring{A}$), P is incident laser power, and α is the monolayer absorption coefficient (about 2.3%) [28].

2.4.3 Photo-Bolometric Effect

Although PTE and PV effects are thought to be the competing, dominant photocurrent generation mechanisms in graphene, the photo-bolometric effect may have a non-negligible contribution under certain conditions. If photocurrent generation is photoconductive, then photons create new conductance channels through the graphene by creating electron-hole

pairs. The photo-excited contribution to the charge density Δn and electron mobility μ are related to the change in conductivity $\Delta\sigma$ by

$$\Delta\sigma = \Delta n e \mu \tag{2.28}$$

where e is the fundamental charge. The photo-induced voltage is then

$$\Delta V = I_{\mathrm{DC}} \Delta R = I_{\mathrm{DC}} \frac{L}{W} \Delta \left(\frac{1}{\sigma}\right) = I_{\mathrm{DC}} \frac{W}{L} R^2 \Delta\sigma = I_{\mathrm{DC}} \frac{W}{L} R^2 \Delta n e \mu \tag{2.29}$$

where L is channel length, W is channel width, R is channel resistance, and I_{DC} is the source-drain current measured. But if the photocurrent generation is photobolometric, then impinging light locally warms the device, inducing a temperature gradient between the lattice and its thermal reservoir (substrate). The photo-induced voltage is then

$$\Delta V = I_{\mathrm{DC}} \Delta R = I_{\mathrm{DC}} \frac{dR}{dT} \Delta T \tag{2.30}$$

If the system is at low temperature, then the electronic and lattice temperatures are decoupled. Due to low electronic specific heat and weak electron-phonon interactions, the laser significantly heats electrons above the lattice temperature. Charge carrier transport is sensitive to carrier temperatures, resulting in a change in resitance and an enhanced bolometric photoresponse [29].

Bolometers essentially measure a change in resistance (conductance) due to a change in temperature ΔT induced by the absorption of incident radiation. Because of the electron-photon-decay botleneck in graphene and small electron specific heat, graphene has a hot carrier effect. As the electron temperature rises, carrier scattering occurs more frequently. The current due to the photobolometric effect is described by

$$I_{\mathrm{PHB}} = \frac{V_{\mathrm{PHB}}}{R} = I_{\mathrm{ds}} \frac{\partial R}{\partial T} \Delta T_{\mathrm{e}}, \tag{2.31}$$

where I_{ds} is the measured source-drain current, ΔT_{e} is the elevated electron temperature above the lattice temperature, R is the resistance of the graphene channel, and $\frac{\delta R}{\delta T}$ is the change in graphene resistance per change in lattice temperature [28][29]. Because the photobolometric effect depends on a bias voltage, it will not contribute under zero-bias conditions and can be neglected. In addition, if the incident laser power is low enough such that it negligibly heats the graphene lattice, then this effect will be negligible.

2.5 Mean Free Path Limitations of Photoresponse

Nearly all photons are reflected from the gold contacts, and therefore only photons incident on the exposed graphene channel may contribute to photocurrent (or to scattering processes, like Raman).

Both the photovoltaic and photo-thermoelectric effects rely on photo-generated carriers reaching the built-in electric field near the contacts. Carriers that do so can contribute to the total current, but otherwise they will recombine and not contribute to the total current. The mean free path of a carrier is the average distance it will travel before experiencing a collision, either with the lattice or another carrier.

We hypothesize that when the laser spot distance from the gold contact, illustrated in figure 2.12a, is much greater than the mean free path, then the photovoltaic effect cannot contribute to the total current. However because the photo-thermoelectric effect generates hot carriers, these carriers may survive one or more collisions before recombining or transfer their momentum to another carrier, effectively extending its range of travel and allowing it to reach the contacts from greater distances.

Assuming a Gaussian laser spot distribution, modeled in figure 2.12b, we suppose that only those photons incident on the graphene channel can possibly contribute to the photocurrent due to PV and PTE effects. Photons incident on the contacts are mostly reflected, and the skin depth of the gold is shallow enough that zero photons can reach the graphene beneath them. We then suppose that the mean free path of an electron is limited to 100 nm and consider the fraction of all photons absorbed in the channel that are also within the mean free path of the nearest gold contact. In figure 2.12c we show that this results in at most 20% of all incident photons actually capable of creating an electron hole pair within a mean free path of 100 nm, and only then when the spot is centered very near the contact. If our hypothesis is correct, then one would expect that both PV and PTE effects may be present near the contacts, but only the PTE effect can contribute when the laser spot is farther than the mean free path from either contact. Thus if we were to measure the photocurrent dependence on power and fit $I_{\text{ph}} \propto P_{\text{opt}}^{\beta}$, then we would expect to yield near $\beta = 1$ for a laser spot near the contacts and $\beta = 2/3$ for a laser spot far away (greater than the MFP) from the contacts.

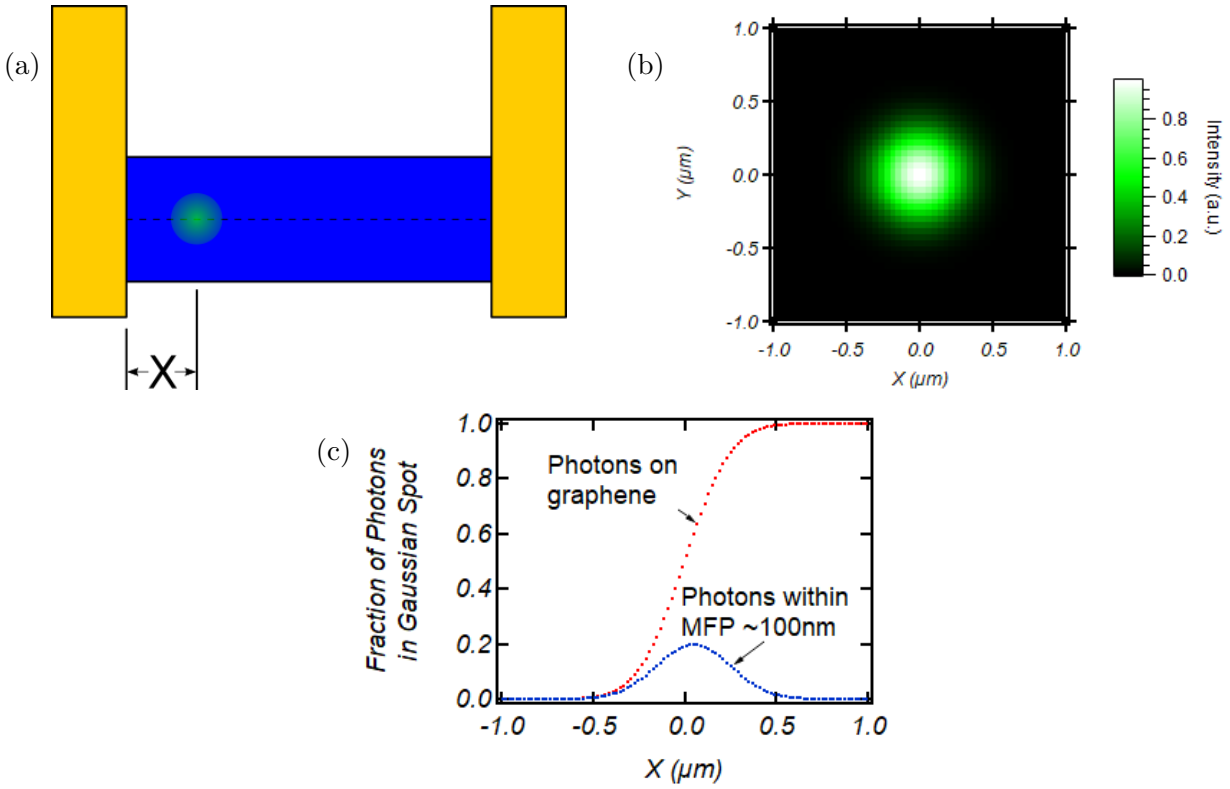

Figure 2.12: Model of photons capable of contributing to photocurrent as a function of distance from source-drain electrodes. (a) Illustration of laser spot on the graphene channel along the centerline a distance x from the graphene-contact interface. (b) Gaussian laser spot model with normalized maximum intensity. (c) Integral volume fraction of photons in laser spot incident on the graphene channel and total fraction photons incident on channel and within mean free path of the contact. Assuming a gaussian laser profile, curve is normalized such that all photons in laser spot is unity. Only photons incident on the graphene channel may possible contribute to photocurrent via PV or PTE.

2.6 Conclusion: a Theoretical Framework for Understanding Photocurrents

In this chapter, we have presented the framework within which to understand the experimental data and calculations to follow. We have shown the electronic dispersion, Raman modes, and the primary contributors to photogeneration in mono- and bi-layer graphene graphene field-effect transistors. The next step will be to combine optical and electronic measurements, along with spatial resolution, to investigate photocurrent dependence on gate voltage, local laser excitation target, laser power, and bias voltage. The different photogeneration mechanisms will contribute to the total photocurrent measured in different proportions according to these parameters, as will be discussed in Chapter 4. But first we must address experimental considerations. In particular we will show how to simultaneously extract optical and electronic measurements for micron-scale devices.

Chapter 3

A Platform for Optoelectronics: Devices, Instrumentation, and Methods

To study the photocurrent mechanisms in graphene transistors, we must simultaneously conduct optical and electronic measurements as illustrated in figure 3.1. In this chapter, we begin with a description of our device fabrication and packaging methods in section 3.2. Next we present our custom-modified system for spatially-resolved photocurrent mapping, with independent control of charge density, laser power, and laser spot targeting at room temperature and ambient pressure, in section 3.3. We then demonstrate a sample of our electrical measurements and analysis techniques in section 3.4. We follow with sample Raman spectral acquisition and analysis. Then in section 3.6, we discuss our photocurrent acquisition and mapping capabilities. We then discuss how we addressed spatial drift and precision in section 3.7. Finally, we detail in section 3.8 our methods and protocols for optical annealing and measuring photocurrents in our graphene transistors.

3.1 Introduction

Although photocurrent in graphene transistors has been heavily investigated, there is some disagreement in literature concerning which photogeneration mechanisms dominate. In particular, it is unclear how the spatial targeting of the laser spot influences which mechanisms

dominate. In our own lab, research had been almost exclusively limited to electron transport, using Raman spectroscopy only as a tool for characterizing the number of layers in a sample. The independent optical and electronic equipment were not designed to interface, and thus we made modifications to hardware and software to allow simultaneous measurements.

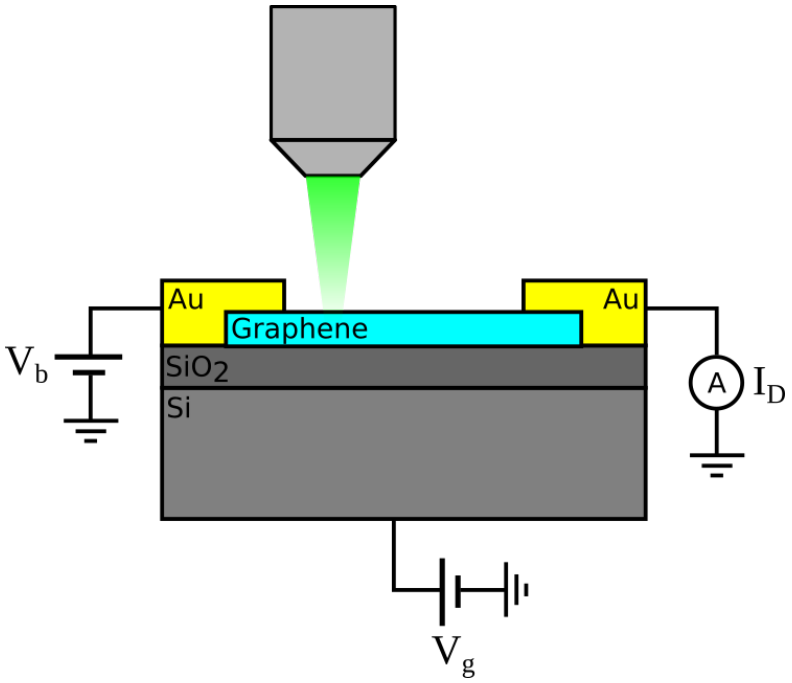

Figure 3.1: Cross-sectional illustration of laser illumination and electronic circuit. A microscope objective focuses a laser into a spot on the graphene channel. Bias and gate voltages V_B and V_G can be applied to the sample while the drain current I_D is recorded.

As we have discussed in Chapter 2, there has been much investigation into the photocurrent mechanisms operating in graphene devices. However there is still disagreement on which mechanisms contribute and under what conditions they dominate. In particular, there remains much to be explained about the photocurrent mechanism's dependence on the laser spot position. The challenge in performing such an experiment is that it requires sub-micron certainty of laser spot position, coordination of optical and electronic measurements, live measurement of incident laser power, and a wide range of optical power configurations. Our Renishaw inVia spectrometer had the precision we required, but was lacking a means to conduct electrical experiments. By designing a sample holder interface, we were able to combine the capabilities of our optical apparatus with that of our electronic apparatus.

In this chapter, we begin describing fabrication and packaging of graphene transistors used for studying the photocurrent mechanisms in micron-scale graphene ribbons. Next we will

delineate structure and design of our optical setup and its integration with electron transport instrumentation. Finally we outline our electronic, optical, and simultaneous measurement methods.

3.2 Fabrication of Graphene Transistors

In this section, we discuss the fabrication details and packaging of graphene devices. Because graphene flakes are obtained via mechanical exfoliation, size and shape are not controlled, but rather selected. The challenge in this process is that it requires patience and yields very few devices. Particularly because we required rather large dimensions, micron-scale for both monolayer and bilayer samples, suitable flakes were extremely rare.

Our ideal device geometry consists of a rectangular graphene flake, supported on Si/SiO_2 substrate, with gold films evaporated onto opposing ends of the flake to serve as source-drain electrodes, like that illustrated in figure 3.1. The n-doped silicon will serve as a back gate for applying an orthogonal electric field to the graphene channel. We summarize the process, including preparation of the substrate wafer, deposition of graphene flakes, deposition of gold contacts, and packaging.

We begin with a 4" diameter, 500 μm thick, $\langle 100 \rangle$ Si/SiO_2 wafer. The wafer initially has a coating of 300 μm thick SiO_2 on either side with a surface roughness of ± 10 nm, and reactive ion etching is used to remove this layer from the backside to facilitate connecting the gate. Gold grids are patterned onto the wafer, using mask-aligned photolithography, to allow for ease of locating flakes later. Wafers are then diced into several chips of at least 7×7 mm^2 and cleansed of organic contamination via etching in HCl/H_2O_2 solution. Next we deposit graphene flakes onto the chips via mechanical exfoliation. Several HOPG chunks are placed onto Scotch tape, which is then folded and peeled 20 times such that the tape is covered in fine graphite dust, as seen in figure 3.2, before firmly pressing the chips into the tape for a few minutes. As the tape is gently peeled off, van der Waals forces hold flakes of graphene and chunks of graphite to the Si/SiO_2 susbstrate. We use high quality HOPG in order to maximize the size and number of deposited graphene flakes. However the tape leaves behind some adhesive residue, which must be removed by soaking the chip in acetone. Now that the flakes are deposited, we look for suitable device candidates using optical microscopy to search through the patterned chips for flakes conforming to size and shape requirements. Pictured in figures 3.2 and 3.2, monolayer graphene flakes are visible but nearly transparent when

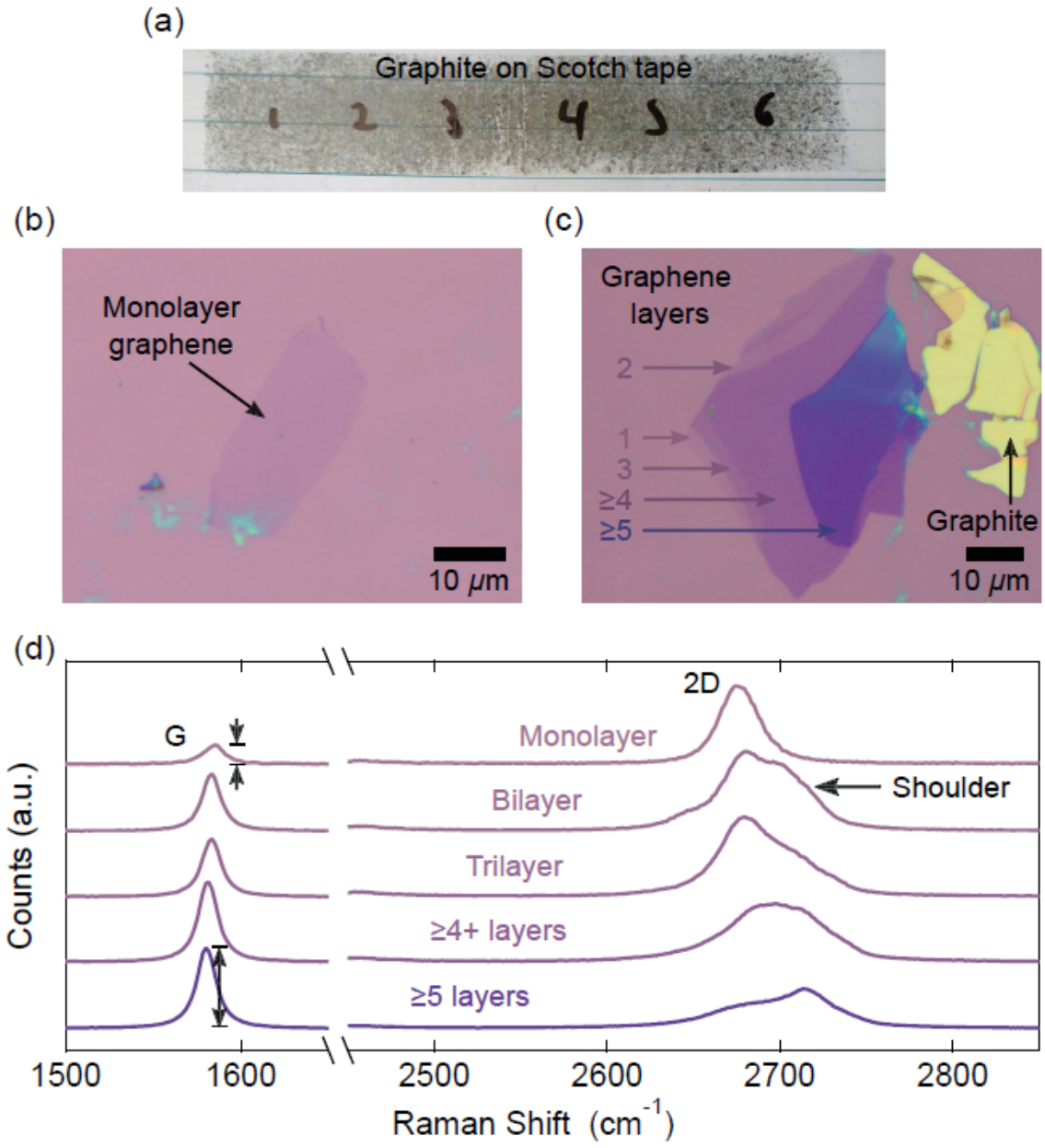

Figure 3.2: Graphene mechanical exfoliation, deposition, and identification of layers via microscope and Raman analysis. (a) Image of graphite on Scotch tape during exfoliation. (b) A sample monolayer graphene flake deposited via mechanical exfoliation. (c) Optical image of monolayer vs multilayer graphene flakes and bulk graphite). (d) Comparison of Raman spectra of graphene by number of layers. Figures borrowed from McRae 2018 [15].

viewed under a microscope and bilayer flakes appear somewhat darker. As we search for flakes, candidates are photographed and their positions noted. However it is often difficult to distinguish monolayer and bilayer flakes from higher number layers, so we must quantitatively confirm them with another method.

We must confirm our candidate flakes are monolayer or bilayer, and thus we use Raman spectroscopy to characterize them by number of layers and quality. Raman spectra are recorded for each flake using a 532 nm excitation laser, and can be used to quantitatively determine how many layers of graphene are present, as well as the structural quality of the crystal lattice. First we inspect and compare the G and 2D Raman peaks found near 1583 cm^{-1} and $2,700$ cm^{-1} respectively, as can be seen in figure 3.2. As discussed in chapter 2, the 2D peak has a Lorentzian shape in monolayer graphene, but is composed of at least 4 Lorentzians in multilayer graphene. Additionally, the 2D peak is much higher than the G peak in monolayer. Therefore monolayer graphene can be immediately and qualitatively distinguished from multilayer by inspection of the 2D peak line shape. Quantitatively we confirm the number of layers by calculating the G/2D integrated intensity ratio. Monolayer flakes yield a G/2D ratio of about 0.12 ± 0.02, bilayer flakes 0.22 ± 0.02, and flakes of > 3 layers 0.28 or higher. Additionally, we quantitatively evaluate the structural cleanliness of our flakes by comparison of the D and G peaks. The D peak arises as a consequence of disorder in the crystal lattice, and an increase in its height corresponds to an increase in defect density. The samples presented in chapter 4 of this thesis showed no discernible D peak, and therefore based on the resolution of our measurement we can estimate the upper bound defect density of our flakes to be 10.9 μm^{-2}. Thus we have qualitatively and quantitatively investigated our graphene flakes to confirm that our flakes are monolayer or bilayer, and that the crystal structure has minimal structural defects.

For spatially-resolved photocurrent measurements, we require devices of at least 1 μm width and 2 μm length of uncovered graphene because our laser spot has an FWHM of between 336-432 nm, limiting our spatial resolution to at best around 0.5 μm. With these minimum dimensions we can distinguish regions of graphene channel, graphene edges, left vs right contacts, and some transition in-between. However since parts of each flake will be covered by gold contacts, we require that candidate flakes have an extra 1 μm length on opposing sides for good contact with the source-drain electrodes, reducing contact resistance.

Once we have selected a candidate flake for a device, we clean the chip with acetone and IPA and coat the chip with a 200 nm layer of PMMA A4. We design a pattern of source-

drain contacts using CAD, align and etch this pattern into the resist using electron-beam lithography, and then develop the resist. Next, we deposit a 3 nm sticking layer of Cr followed by a layer of Au. For device A, the layer of gold is 57 nm thick, and for all others it is 100 nm. Finally, we perform lift-off in hot acetone to remove the resist and excess deposited metal, and rinse the chips in IPA.

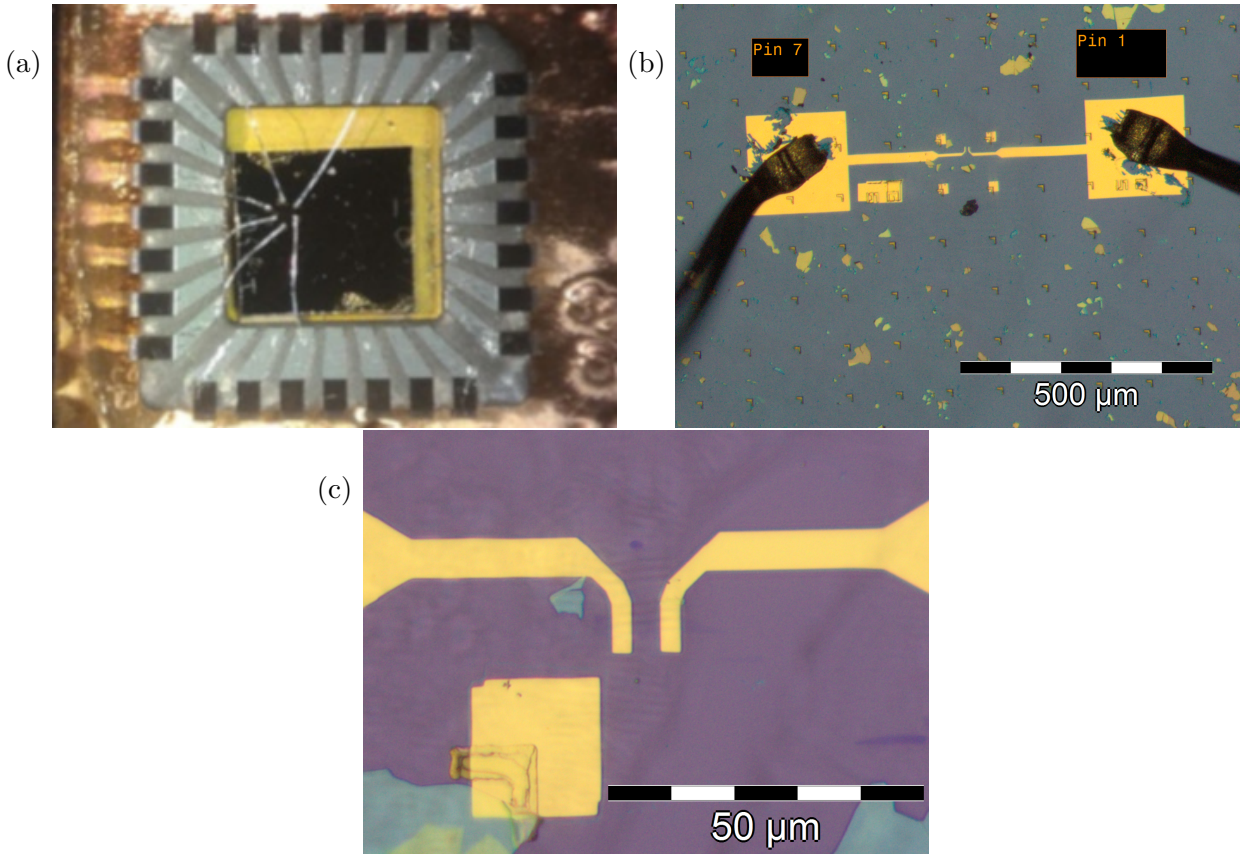

Figure 3.3: Device packaging and wirebonding. (a) Chip carrier with wirebonded device, as seen through a stereoscope. (b) Gold contact pads with wirebonds, as seen under a microscope. These wirebonds connect the measurement circuit to the gold pads, which are in turn connected to the source and drain contacts attached to the graphene channel. (c) Microscope image of a graphene transistor with gold contacts.

To connect our device to our measurement circuit, we require that it be packaged onto a chip seat compatible with a PLCC-28 socket. We place a small drop of silver paint in the center of chip seat, then gently press our chip into it and allow it time to dry, thereby bonding the doped Si to the chip carrier gold surface. We load the chip carrier into the Westbond 7400A wedge bonder grounded socket, grounding all pins for the safety of the device. Then we bond 25 μm diameter aluminum wires (1% silicon) from the chip carrier pins to the large gold

pads which are part of the source-drain electrodes on the device and to the gate via the gold surface of the chip carrier, which is pictured in figures 3.3. Now that the device is packaged, the chip seat can be placed into any compatible socket to easily connect it to our electronic measurement circuit. Next we must address optical capabilities.

3.3 Opto-electronic Instrumentation for Spatially-Resolved Photocurrent Mapping

We wished to explore photocurrent in graphene as a function of laser spot position to understand how each the PV and PTE effects contribute, mapping photocurrent vs position. In particular we wish to see whether the two effects can be selected by adjusting the spot position. To acquire photocurrent data on our graphene devices, we must coordinate two previously independent measurement systems designed for optical and electronic measurements. Our Renishaw inVia Raman spectrometer system was not designed to support electronic experiments, nor our electronics apparatus for optical experiments. Therefore we designed and implemented hardware and software modifications to accomodate simultaneous measurements, as well as further modifications to increase the available laser power selection, reduce mechanical vibrations, and allow continuous monitoring of the incident laser power.

3.3.1 Electronic Measurement Apparatus

Our sample holder, seen in figure 3.4b , was originally designed for RF measurements and is suitable for our DC measurements. It includes eight SMA interfaces that allow electrical circuit connections to pins 1, 5, 7, 11, 13, 17, 19, 23, and 25. All other pins in the sample holder are grounded. Wires connect these ports to a National Instruments PCIe-6321 DAQ card, a Keithley 2400 voltage source, and an Ithaco 2110 current preamplifier, seen in figure 3.4a, according to the circuit diagram illustrated in figure 3.5. The DAQ allows us to output a bias voltage of up to $\pm 10\ V$. A voltage divider allows us to precisely reduce this output to the order of mV on-sample by a voltage divider. As seening in figure 3.4a, we use a Keithley 2400 controlled by the computer via GPIB connection to supply gate voltages. Although it can supply voltages in excess of ± 100, we limit our experiments to ranges of $V_{\mathrm{G}} = \pm 50\ V$ or less in order to reduce the risk of dielectric breakdown, which can destroy devices.

(a)  (b) 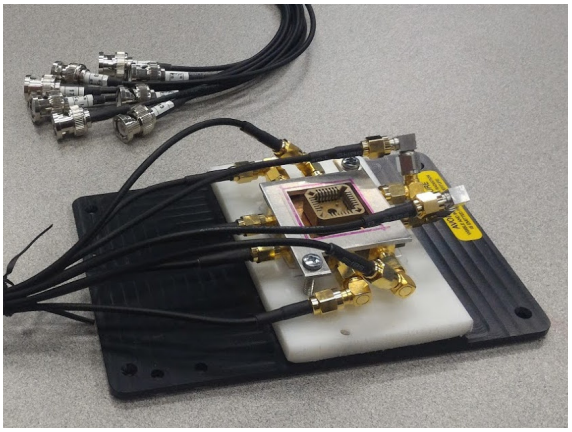

Figure 3.4: (a) Keithley 2400 voltage source stacked atop Ithaco 1211 current pre-amplifier. The Keithley allows applied gate voltages in excess of $\pm 100\ V$, far greater than the DAQ card voltage output limited to $\pm 10\ V$. The Ithaco amplifies drain current which can then be recorded via the DAQ card. Each connects to the measurement circuit via BNC connections. (b) The sample holder has a socket compatible with PLCC-28 chip carriers, and connects to the measurement circuit via SMA-to-BNC cables (RG174/U MIL-C-17). A plastic seat and metal faceplate fix the sample holder to a baseplate which attaches to the translation stage.

(a) 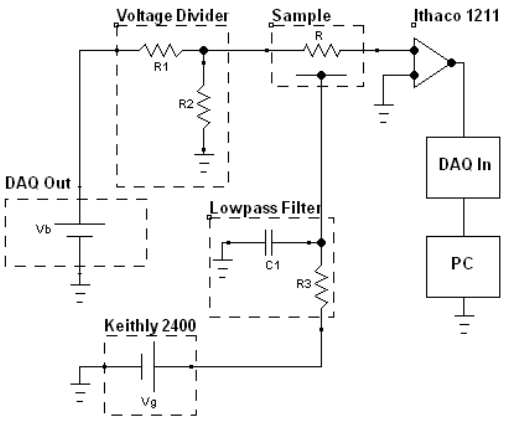

(b) 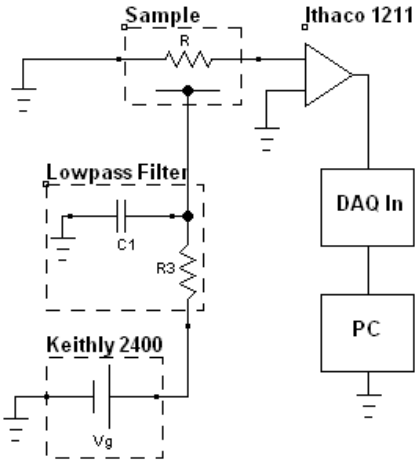

Figure 3.5: Electron transport circuit diagrams. (a) Measurement circuit used for electron transport and photocurrent experiments. (b) Simplified measurement circuit for photocurrent experiments taken at $V_\mathrm{b} = 0$.

(a)  (b) 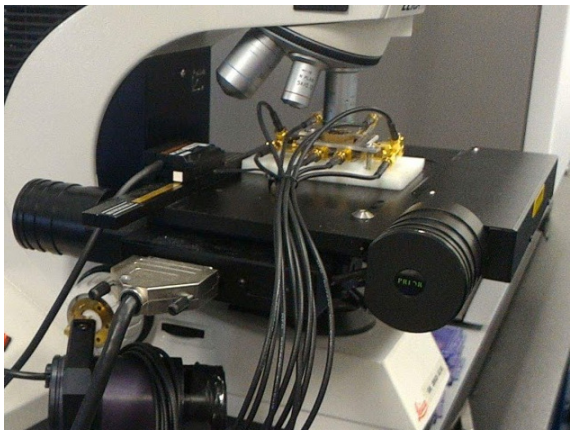

Figure 3.6: Sample holder with adapter under microscope. (a) Circuit connections to the sample holder are made via rigid SMA wires with SMA-to-BNC adapters. The result was too much weight and tension in the wires, reducing spatial accuracy. (b) Sample holder connected using SMA-to-BNC wires. The connections are flexible and lightweight enough to not exert excessive force on the translation stage. These cables are more easily managed.

To optically study our devices, the sample holder must be rigidly mounted onto the Prior ProScan motorized XYZ translation stage. To achieve this, we designed a plastic spacer with screw holes to mount onto an interchangeable translation stage plate, as seen in figures 3.6b and 3.4b. Additionally, we fashioned a steel faceplate which sits over the sample holder and fixes it to the plastic spacer using two screws in opposing corners. The stage plate is then connected rigidly to the translation stage and secured via four screws. Once a device is loaded in the sample holder and fixed under the microscope, we can then make optical and electronic measurements simultaneously.

Our first iteration, seen in figure 3.6a, used heavy, rigid wires that would resist and exert excessive force on the motor stage, reducing spatial accuracy, defocusing the microcsope, and hindering repeatability for mapping areas greater than a few microns. We replaced these wires with SMA-to-BNC wires (RG174/U MIL-C-17), shown in figures 3.4b and 3.6b, which were lightweight, flexible, and didn not require an extra SMA-to-BNC adapter. The new wires improved spatial accuracy, and could be more neatly managed. At this point we can then connect a packaged sample to the measurement circuit by loading it into the sample holder and mount the holder onto the microscope translation stage, thereby allowing us to perform optical and electronic measurements concurrently, as shown in figure 3.7.

(a) (b)

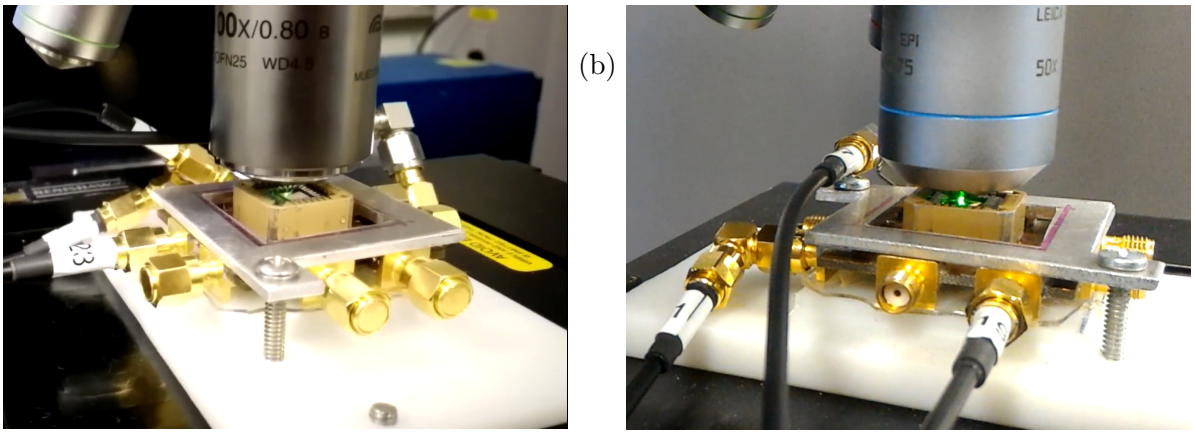

Figure 3.7: Packaged graphene transistors mounted under microscope and connected to electrical measurement circuit. (a) Packaged graphene transistor loaded in sample holder mounted on translation stage under 100x microscope objective with laser spot incident on sample. (b) Another packaged graphene transistor loaded in sample holder mounted on translation stage under 50x microscope objective with laser spot incident on sample.

3.3.2 Optical Measurement Apparatus

For optical measurements, we use a Renishaw inVia Raman spectrometer, seen in 3.8a, equipped with a Prior ProScan morotized translation stage, an Innovative Photonic Solutions 532 nm spectrum stabilized laser source (model I0532SR0050B), and a Leica DM LM optical microscope. According to specification, the translation stage has a spatial precision of $\pm 0.05 \mu m$ for in-plane XY directions. Our laser spot has a Gaussian distribution when focused onto the sample, and its width depends on the objective used. For our 50x and 100x objectives, our spot is elliptical with FWHM between 336 nm and 432 nm, thus we estimate the limit of our optical resolution to be at best 0.4 μm. Because we want to investigate photocurrent dependence on laser spot position, we selected larger graphene flakes with dimensions of at least 2 μm. Renishaw's WiRE software controls the translation stage and has many customizable acquisition options, including acquisition time laser power, mapping dimensions, automatic laser focusing, and more. The diagram in figure 3.8b shows a typical optical beam path of a Renishaw inVia system. The holographic filters fulfill the same function as a dichroic mirror, directing the excitation laser beam toward the sample, and allowing the scattered light to pass through it toward the diffraction grating and CCD camera.

In order to measure the photocurrent exponent, we require a large selection of laser power settings. The Renishaw inVia system comes stock with a set of flag neutral density filters,

(a)

(b)

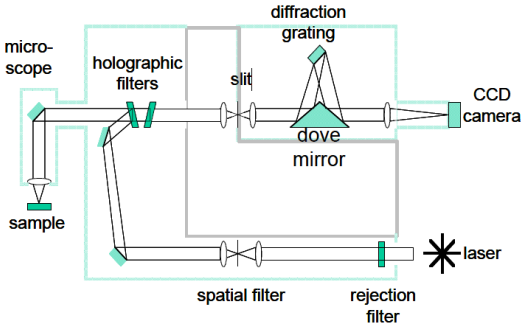

(c)

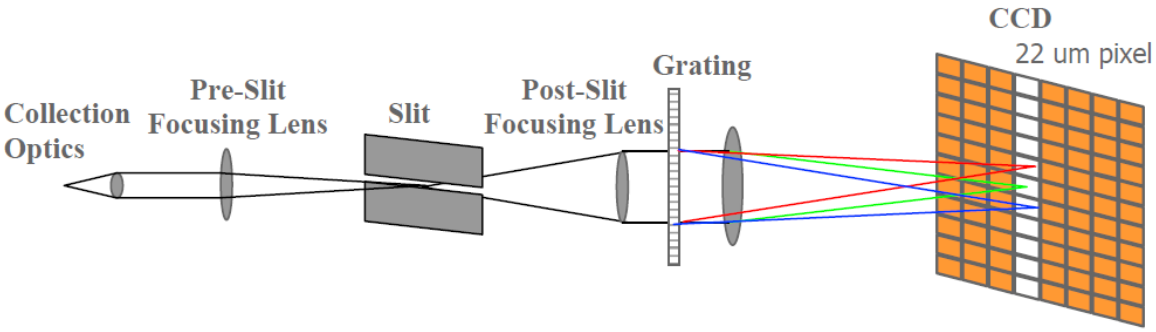

Figure 3.8: (a) Renishaw inVia Raman spectrometer system with Leica optical microscope and Prior Scientific XYZ translation stage. (b) Beam path diagram and components of the Renishaw inVia Raman system. A laser beam is focused on a sample, then the scattered light of variaous wavelengths is guided through the spectrometer, separated by the grating, and measured by the CCD. Figure borrowed from Abel 2005 [30]. (c) Renishaw inVia systems incorporate a dispersive multi-channel spectrometer with a CCD camera whose pixel size is $22\mu m$. Figure borrowed from Abel 2005 [30]

(a) (b)

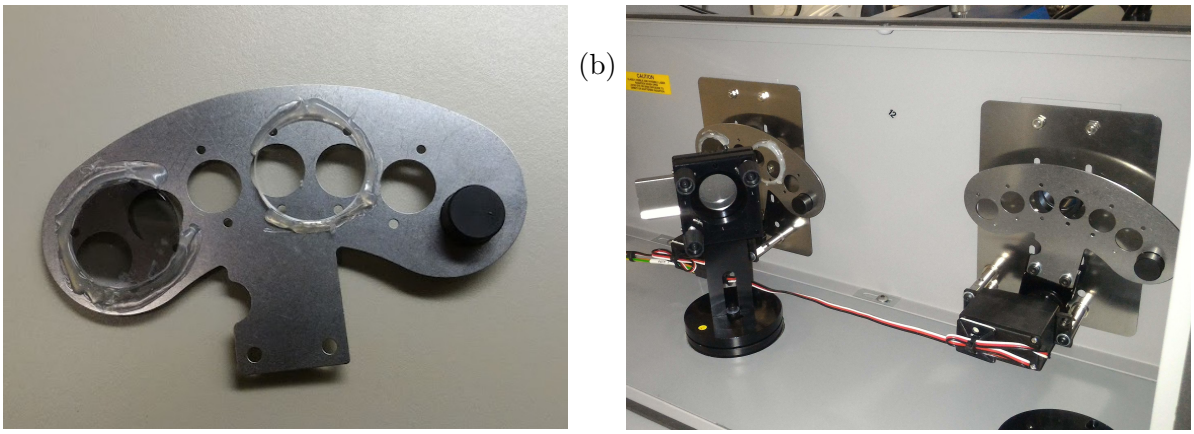

Figure 3.9: Neutral density filter modifications. (a) Motorized arm with added ND filters OD 0.5 and 0.04, obverse side. An OD 0.1 filter is added to the reverse, overlapping apertures 5 and 6. Thus this arm enables 5 unique laser power settings that can be combined with the Raman system's existing filter set. (b) Image of motorized arm with added ND filters. Apertures with different ND filter configurations are selected by rotating the motorized arm.

attenuating the laser by 50%, 10%, 1%, and 0.1%. These filters are motorized, operating independently of each other, and can be combined in order to increase the number of power settings. These provide us with 7 unique power settings between 100% and 0.10% transmission. To further increase the number of available settings, we made use of a general-purpose motorized arm with 7 apertures, pictured in figure 3.9. Aperture #2 is left empty to allow 100% light transmission and aperture #1 is covered, serving as the laser shutter. We fixed 3 ND filters to motorized arm using hot glue, partially overlapping 2 of the filters in order to create an effective 4th ND filter. The resulting power configurations were 0%, 100%, 91.2%, 79.4%, 25.1%, and 31.6% for apertures 1 through 7 respectively. At any given moment only one of these additional ND filters can be actively in the beam path, however they can be combined with the flag filters to further increase the number of available power settings to 35 between 100% and 0.025%. Listed in table 3.1 are all power settings available between 100% and 0.29% transmission combining added filters with the original stock filters.

Software (%)	Measured (mW)	Measured (%)
100	18.3	100
91	17.3	94.54
80	15	81.97
50	10	54.64
45.5	9.55	52.19
40	8.24	45.03
31	6.42	35.08
25	5.47	29.89
15.5	3.5	19.13
12.5	2.96	16.17
10	1.94	10.60
9.1	1.83	10.00
8	1.58	8.63
5	1.05	5.74
4.55	0.991	5.42
4	0.858	4.69
3.1	0.676	3.69
2.5	0.570	3.11
1.55	0.365	1.99
1.25	0.307	1.68
1	0.147	0.80
0.91	0.138	0.75
0.8	0.120	0.66
0.5	0.0795	0.43
0.455	0.0753	0.41
0.4	0.0655	0.36
0.31	0.0524	0.29

Table 3.1: Laser power settings available with added ND filters. The software was initially configured using the labeled values of all ND filters, both stock and added. We then measured the nominal optical power after the filters for all power settings, and re-adjusted the software values to match. These are the power settings available from 0.29% to 100%.

(a)

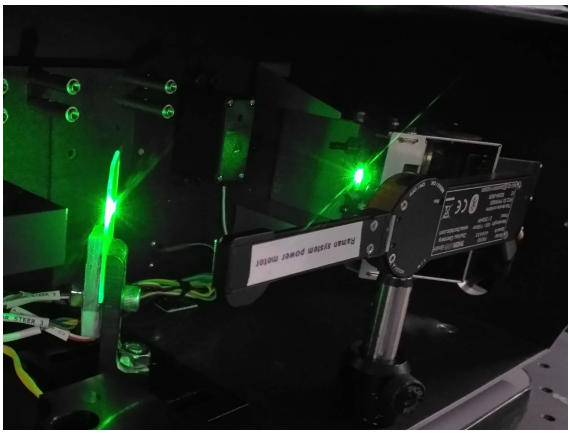

(b)

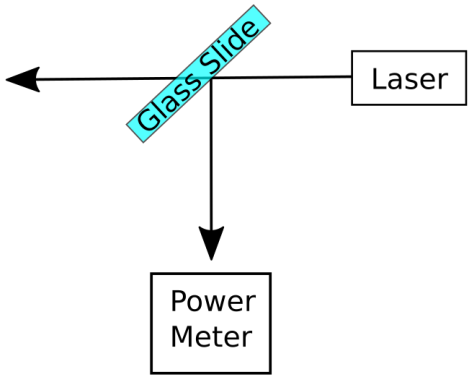

Figure 3.10: Optical power meter installation. (a) Optical power meter installation with glass slide oriented at 90° as a beamsplitter. The majority of laser light transmits through the glass slide, and a fraction is reflected toward the Thorlabs PM160 power meter. (b) Beam path diagram, highlighting glass slide beamsplitter and power meter.

Now that we have spatial precision and available optical power settings addressed, we will need to measure and record the optical power concurrently during experiments. Since we require the laser power on the sample in order to determine the photocurrent exponent, we must have some means of measuring the laser power output. To accomplish this, we inserted a thin glass slide, as shown in figure 3.10, into the beampath inside the spectrometer box, after all ND filters, at an angle of 45°, thereby reflecting a small portion of light 45° from the original beam path, absorbing a small amount of light, and transmitting the rest. Finally, a Thorlabs PM160 is fixed into place to measure the reflected light. By determining the ratio of power transmitted vs power reflected, we can calculate the transmitted power for all future measurements by measuring only the reflected light. In this way, we can measure continuous laser power simultaneously with our opto-electronic experiments without interrupting measurements. We calibrate this setup by measuring the laser power immediately before the glass slide, the laser power transmitted after the glass slide, and the laser power reflected by the glass slide. Most of the light is transmitted through the glass slide, continuing on the orignally designed beam path. Because the slide is very thin, refraction through the glass slide negligibly affects the beam path. A small fraction of the laser is absorbed and the rest is reflected toward the power meter. As recorded in table 3.2, we measured the optical power immediately before and after the glass slide to be 382 μW and 297 μW respectively, and the reflected light to be 51.2 μW. By calculating the ratio of the optical power transmitted and reflected, we find a ratio of 5.605 which can be used to calculate the optical power entering into the microscope objectives from the measured reflected beam path. The software pack-

aged with the PM160 can then record optical power reflected during measurements. But we are ultimately interested in the laser power on the sample, so we need to know how much light is attenuated through each microscope objective.

Light Measured	Power (mW)	Power (%)
Before Slide	0.382	100
Reflected 90°	0.0512	13.4
Transmitted	0.287	75.13
Losses		11.47

Table 3.2: Laser power attenuation due to glass slide. Power was measured with a Thorlabs PM160, capturing power incident on, transmitted through, and reflected from the glass slide. The resulting ratio of power incident over power reflected is 5.605. Thus the reflected laser power recorded during experiments must be multiplied by 5.605 to get the laser power entering the microscope objective.

Objective Magnification	Power after Slide (mW)	Power after Objective (mW)	Attenuation Ratio
50x	1.65	1.05	0.636
50x	1.64	1.03	0.628
50x	1.65	1.05	0.636
100x	1.65	0.47	0.285
100x	1.65	0.46	0.279
100x	1.65	0.47	0.285

Table 3.3: Laser power attenuation due to objective. Power was measured with a Thorlabs PM160 immediately after the glass slide and immediately after select objectives in a dark room. The average attenuation ratio for our 50x and 100x objectives were 0.634 and 0.283 respectively, and are used in calculations to determine the power incident on-sample.

In our experiments we use 100x and 50x objectives with numerical apertures of 0.80 and 0.75 respectively, and characterized their light attenuation by using a power meter to measure the light in the beam path immediately after the glass slide beamsplitter, and the light exiting each objective. The results, shown in table 3.3, show that the 50x and 100x objectives have an attenuation ratio of 0.634 and 0.285, respectively. Finally we can calculate the optical

power focused on a sample according to:

$$\begin{pmatrix}\text{Power on}\\ \text{Sample}\end{pmatrix} = \begin{pmatrix}\text{Raw Power}\\ \text{Reading}\end{pmatrix} \times \begin{pmatrix}\text{Glass Slide}\\ \text{Attenuation}\\ \text{Ratio}\end{pmatrix} \times \begin{pmatrix}\text{Objective}\\ \text{Attenuation}\\ \text{Ratio}\end{pmatrix}, \tag{3.1}$$

where $RawPowerReading$ is the raw data acquired from the PM160, the attenuation ratio due to the glass slide is 5.605, and $ObjectiveAttenuationRatio$ is the attenuation ratio due to the selected microscope objective.

Although the laser specifications indicate it should have a power stability within ±5%, we noticed occasionally during hours-long experiments that the laser output power may fluctuate by as much as up to ±15%. Figure 3.11 presents a sample acquisition during which the laser power drifted quite a bit. One protocol that reduces fluctuations is to warm up the laser for at least 2 hours, longer than the 30 minutes specified in the system's documentation. Sometimes simply turning the laser off and on again would correct the issue. However since the drift occurred over periods on the order of hours, short experiments completed in under 30 minutes would be relatively stable.

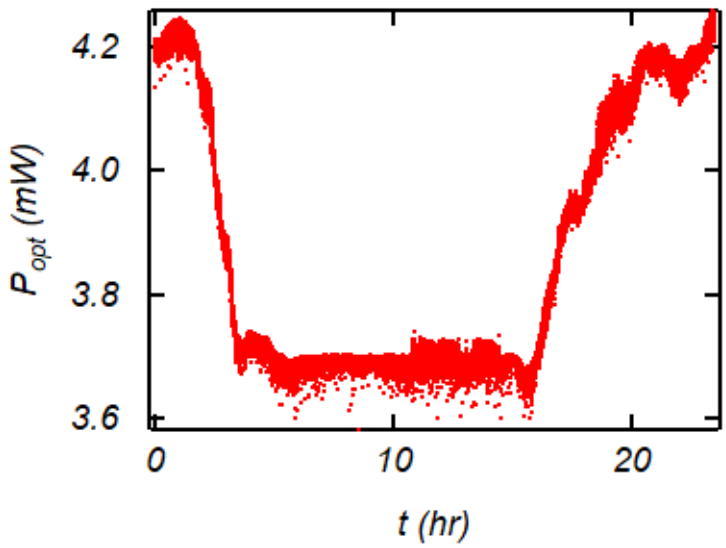

Figure 3.11: Laser power stability over time. The laser spec indicates that the laser power stability may fluctuate within ±5%, however our measurements show that such fluctuations may exceed that. Shorter experiment have less risk, but laser power must always be recorded during photocurrent experiments.

3.3.3 Laser Spot Characterization

In order to characterize our laser spot, we focus the laser on the Si substrate with a 100x microscope objective ($NA = 0.80$), adjust the camera acquisition time such that the laser spot is clearly visible and not saturated, and then capture the image. Next, we convert the image to grayscale, where the value of each pixel becomes a measure of intensity. Once we plot the data in Igor Pro 7, we can then fit the intensity profile with the 2D Gaussian function:

$$f(x,y) = A\exp(-(a(x-x_0)^2 + 2b(x-x_0)(y-y_0) + c(y-y_0)^2)), \tag{3.2}$$

with coefficients $a = \frac{\cos^2\theta}{2\sigma_x^2} + \frac{\sin^2\theta}{2\sigma_y^2}$, $b = -\frac{\sin 2\theta}{4\sigma_x^2} + \frac{\sin 2\theta}{4\sigma_y^2}$, and $c = \frac{\sin^2\theta}{2\sigma_x^2} + \frac{\cos^2\theta}{2\sigma_y^2}$, where A is the amplitude, $\sigma_{x,y}$ are the widths along the x and y axes, and θ is the rotation of the Gaussian spot. From this fit we can extract the FWHM for each axis according to:

$$FWHM_{x,y} = 2\sqrt{2\ln(2)}\sigma_{x,y}. \tag{3.3}$$

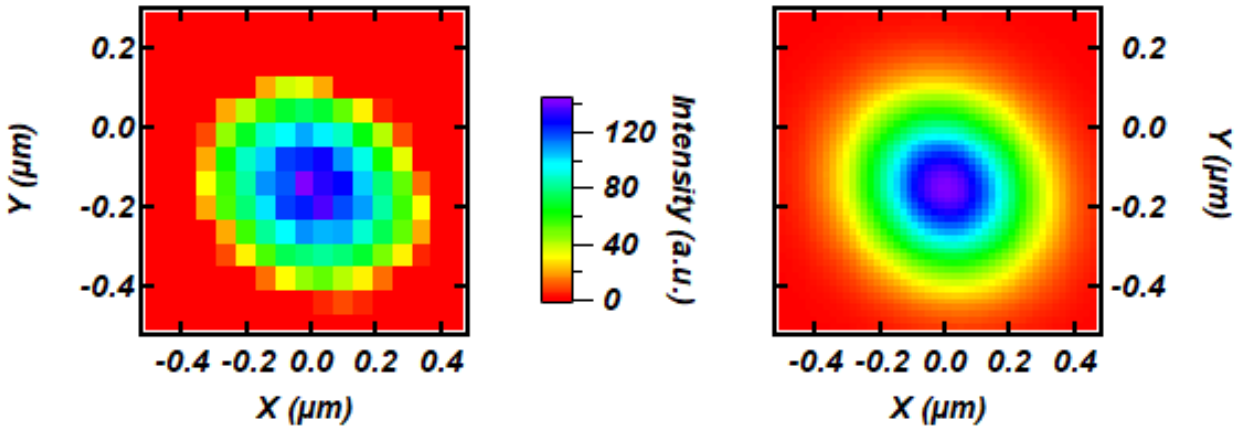

Figure 3.12: Laser spot characterization via Gaussian fit. The left shows an image of measured laser spot intensity reflected from the Si/SiO_2 substrate through a 100x microscope objective, while the right shows a 2D gaussian fit of the laser spot image. Our spot appears to be elliptical and rotated by nearly 45°.

The raw data and resulting fit are shown in figure 3.12, displaying our elliptical spot. From the narrow and wide cross-sections, we extract $FWHM_x = 336\ nm$ and $FWHM_y = 432\ nm$, as shown in figure 3.13. An elliptical spot shape is not ideal, and can be corrected in future experiments by introducing a beam-expander in the optical path just after the built-in neutral density filters.

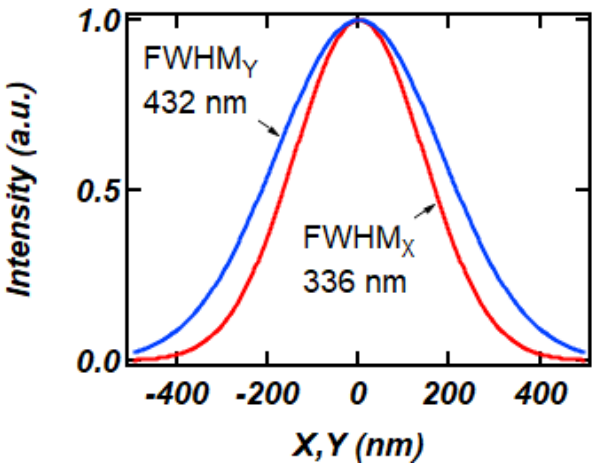

Figure 3.13: Extracted laser spot Gaussian FWHM. We extracted $FWHM_x = 336\ nm$ for the narrowest width of the spot, and $FWHM_y = 432\ nm$ for the broadest.

3.3.4 Vibration Isolation and Table Leveling

To obtain high quality data, we had to address vibrations in the building. Previous users of the Raman system only required the spatial stability to be accurate within a few minutes, but our newfound photocurrent and Raman mapping experiments could last up to several hours. Construction of a building nextdoor, in addition to building vibrations of less than 30 Hz on the fifth floor of the building, made spatial accuracy during such long measurements nearly impossible. We observed drifting within the XY plane, but also observed the microscope focus (Z-axis) drift. To address this we transferred the Raman system onto a Newport VW-3660-OPT-0121 optics bench, pictured in figure 3.14b, equipped with a pneumatic vibration isolation system.

Compressed air stored in a cylinder "floats" the tabletop by raising supports in each leg of the table, lifting it above the metal frame. The gas cylinder regulator outputs about 110 PSI to an AW20-N02E-CZ regulator, pictured in figure 3.15a, which further reduces the pressure available to the front legs to about 80 PSI. Moving the center of mass of the Raman system as close to the center of the table as possible, we still found most of the weight distributed toward the front legs. We connected one automatic leveler valve, pictured in figure 3.15b to each of the front two legs, effectively controlling their pressures, and therefore height, independently. The rear side of the table supported a lighter load, and only one automatic leveler was necessary to balance them. The pressure in each leg is adjusted to 5-10 PSI above that which is necessary to lift the table by adjusting the leveling arm screw on the

automatic leveler. When this arm lifts above the set point, it releases pressure to lower the table. When the arm lowers beyond the set point, it allows pressure into the leg to lift the table.

(a) 

(b) 

Figure 3.14: Vibration isolation and leveling apparatus. (a) Raman system sits on a baseplate, located on a countertop in the lab. Excessive vibrations through the table made experiments requiring acquisition times longer than several seconds difficult and unfeasible. (b) Raman system after move to Newport optics table with pneumatic vibration isolation. Vibrations transmitted through the legs of the table are severely dampened when pneumatics are active, greatly improving spatial precision and making hours-long measurements possible.

(a) 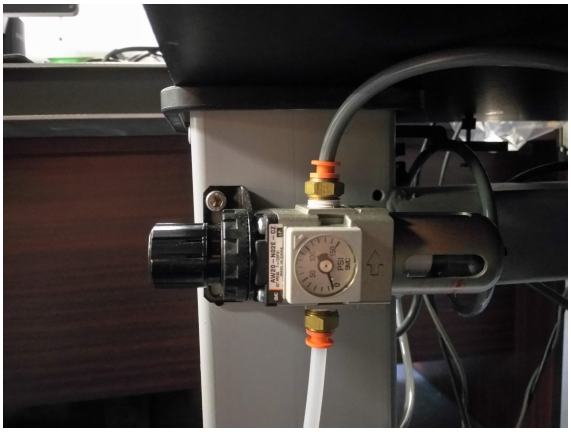 (b) 

Figure 3.15: Newport optics table vibration isolation and auto-leveling system. (a) Image of a regulator which controls the total air pressure available to the pneumatic legs to float the table and adjust table level. (b) The auto-leveling valves have an adjustable lever: when it is too low, air is allowed to flow into the leg, when it is too high air is released via an exhaust valve, and when it is at the set level height, it maintains pressure.

3.3.5 Software Synchronization of Opto-Electronic Measurements

The commercial optical software and custom electrical software were developed and designed to operate independently, making synchronization of measurements a challenge. An initial, temporary solution using timed offsets worked for maps of 30 minutes or less, but would often get out-of-sync by 1 mapping point per 15-30 minutes. To overcome this, we made use of a built-in, software-based triggering system in WiRE. WiRE allows the option of external commands by communicating with 2 Windows handles: one trigger OUT (mapping point complete) and one trigger IN (waiting for signal to begin next point). When both triggers are selected, the Raman system moves the translation stage to the next mapping point with laser active, waits for the IN trigger, acquires a Raman spectrum at the target location, moves the translation stage the next mapping point, sends the OUT trigger, and then the process repeats until all mapping points are acquired. The developers provided sample C++ code to listen for the IN trigger as well as send the OUT trigger, however our electrical acquisition software code built in LabWindows CVI, called *Motor_Curve* and based on the C programming language, is incompatible with C++. However LabWindows CVI can call upon external executables, so we compiled an executable, written in C++ and based on the sample trigger code provided by Renishaw, that simply sends the IN trigger, waits for the trigger OUT from WiRE, and closes. This executable can be called from *Motor_Curve* to synchronize measurements with WiRE.

Incorporating this trigger executable, the new experimental timing is as follows. First of all, the mapping parameters in WiRE must be entered into the interface in *Motor_Curve*, including the number of points in the map and any timing offsets such as for auto-focus or laser annealing. We command WiRE to begin a defined mapping measurement in WiRE, which commences by unshuttering the laser moving to the first map point and waiting for an IN trigger. Next, we initiate *Motor_Curve*, which begins by acquiring the first set of configured electrical measurements.

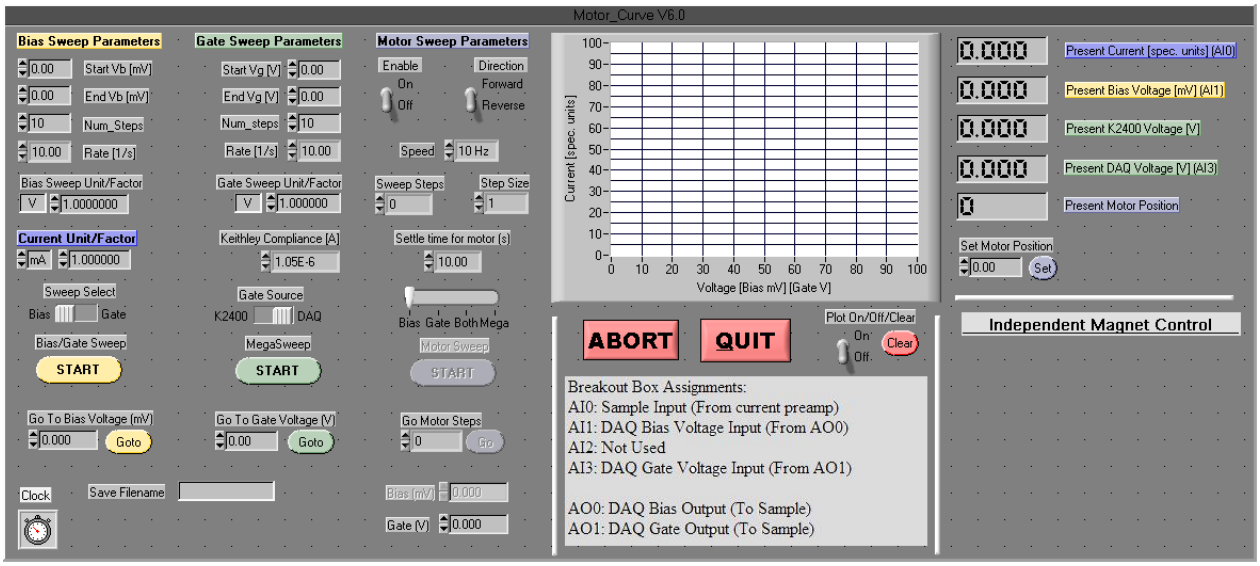

Figure 3.16: Custom lab software for photocurrent experiments. Version of Motor Curve v3.2 drives and monitors electronics equipment, and records measurements. Features include the ability to acquire bias and gate sweeps, complete mega sweeps, as well as motor sweeps for experiments beyond the scope of our photocurrent experiments.

The original version of *Motor_Curve*, whose interface is shown in 3.16, allows customized control over bias, gate sweeps, and combined voltage sweeps. It directly communicates with the DAQ and Keithley 2400 to output and monitor bias and gate voltages, as well as record the drain current that passes through the Ithaco 1211 current preamplifier. It reports and logs live measurement values, and graphs the data in real time. It can also control motors for experiments beyond the scope of this thesis. Data is output to an ASCII formatted, tab-delimited file which includes columns of bias and/or gate voltages, as well as a header including the date, time, and units of acquisition.

Our software modification to facilitate photocurrent experiments introduces several new features. As shown in figure 3.17, there are four new types of photocurrent sweeps available:

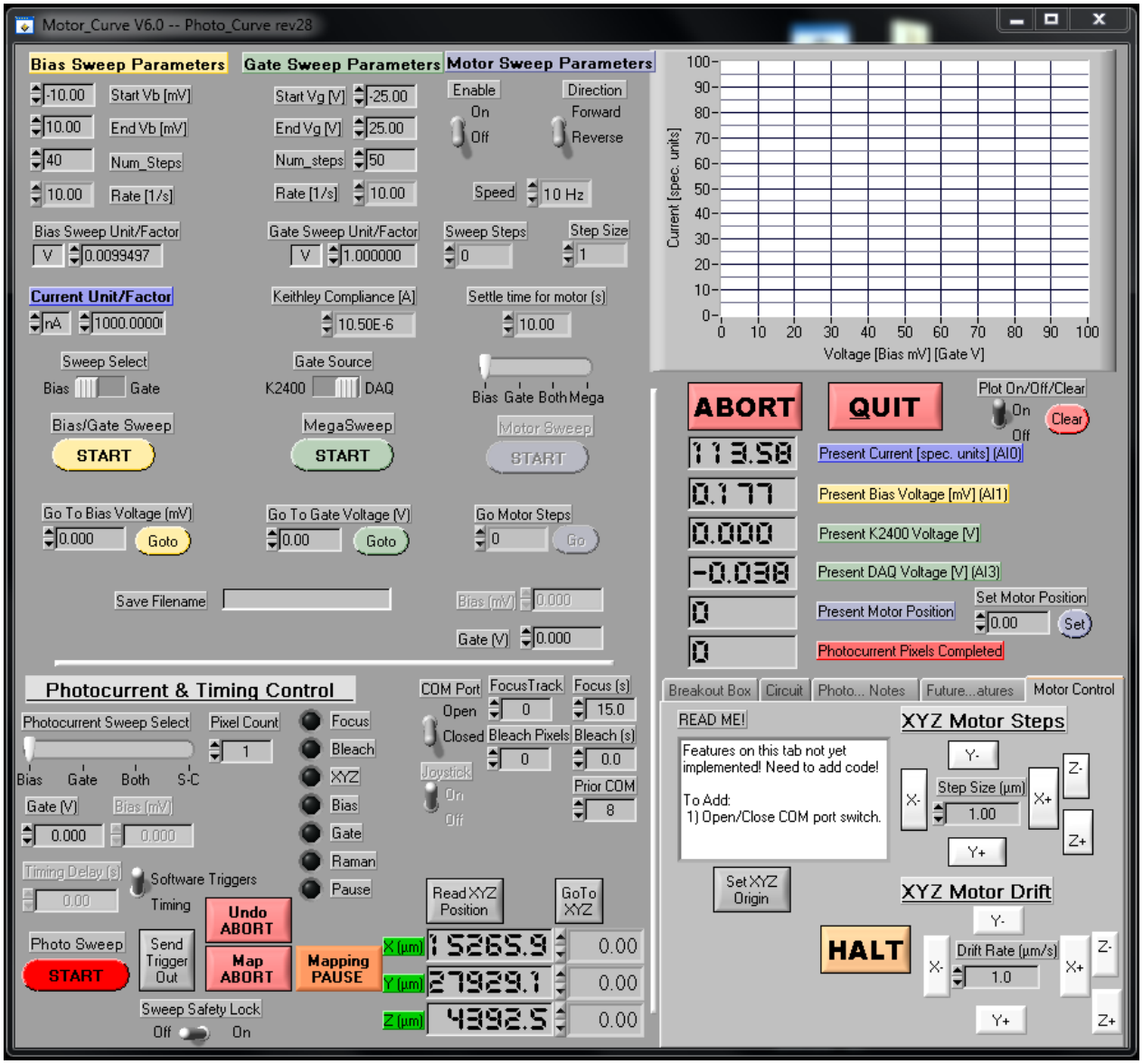

Figure 3.17: Software modifications for photocurrent experiments. The newly customized interface now allows synchronization of Raman experiments controlled by WiRE. It also communicates with and controls the translation stage and has options for 4 types of photocurrent experiments, as well as auto-focusing, pausing for anneals, and software vs timed triggering.

bias, gate, bias and gate, and scanning photocurrent mapping (SPCM). The first conducts a bias sweep for every pixel in a photocurrent map, the second conducts a gate sweep for every pixel, the third conducts a bias sweep then a gate sweep for every pixel, and the fourth simply measures a single datapoint of current. The user can specify gate voltages during bias sweeps, bias voltages during gate sweeps, and both bias and gate voltages for SPCM acquisitions. The user can input timing offsets to account for when auto-focus settings are used in WiRE, and it features both timing and software triggers. Additionally, it can communicate with the Prior Proscan XYZ translation stage to read and write motor position. Maps can be paused at the end of any pixel, and the interface reports live XYZ motor positions and number of pixels completed.

The data outputs to an ASCII formatted, tab-delimited file with seven columns, the first contains either bias or gate voltage measurements, the second contains drain current, the third holds an index representing to which pixel in the map the datapoint belongs, the fourth is the start time of the electrical sweep per pixel, and the last three are the xyz translation stage motor positions in μm. A file header includes the experiment start date and time, column labels, and units used during acquisition. The photocurrent map can then be generated entirely from this data using custom functions written in our data analysis software, Igor Pro 7.

3.4 Electron Transport in Graphene

3.4.1 Measurements

We use two fundamental measurements to characterize electron transport in our devices: bias sweeps and gate sweeps.

First while applying a constant gate voltage, we sweep the bias voltage, resulting in a linear trace as seen in figure 3.18a. Because the gate voltage modulates the charge density, a plot of multiple sweeps at varied gate voltages will show that the slope we extract from the measurement will depend on the gate voltage.

Second, we apply a constant, non-zero bias and sweep the gate voltage, yielding a characteristically U-shaped curve symmetric about a minimum point. This minimum corresponds to the Dirac point, and indicates the gate voltage at which the gate-induced charge carrier

density is zero. The position of the Dirac point is dependent on impurities, as ideal graphene is centered at $V_G = 0$ V. The tails of the curve far from the dirac point may level-off, and the region where this inflection occurs yields information about inherent device properties, such as contact resistance.

3.4.2 Data Analysis

Concerning electron transport, a wealth of information is extracted from a single gate sweep. Here we present a sample analysis on an example device.

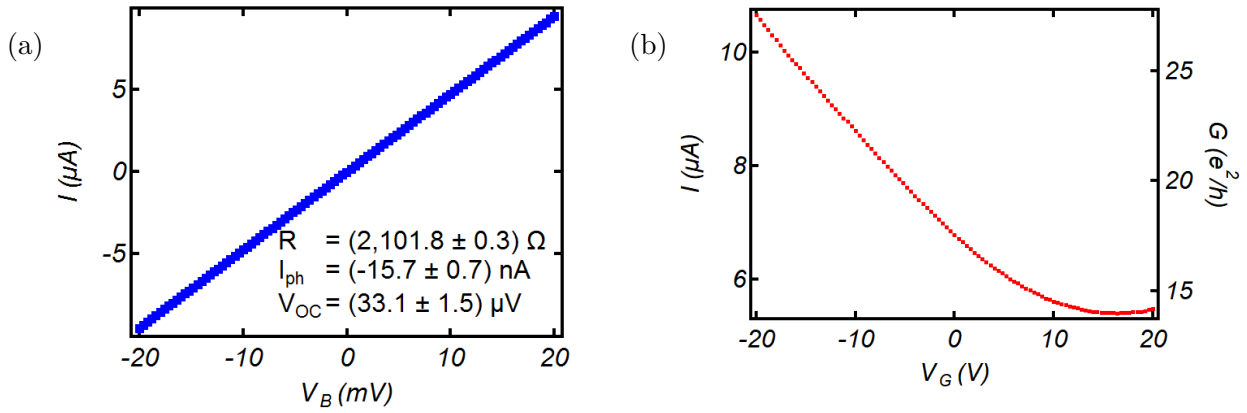

Figure 3.18: Sample bias and gate sweeps of a graphene transistor. (a) Bias voltage sweep acquired at constant $V_G = 0$ gate voltage. The differential resistance is extracted from the slope of a linear fit of the data. (b) Gate voltage sweep acquired at a constant bias voltage. Quantities such as the Dirac point voltage, conductivity, and electron mean free path can be extracted from fits of the data.

In figure 3.18b, consider the point at which gate voltage is $-10.002\ V$. The bias voltage is 10 mV, and the current measured is 8.6176 μA. From these values, we can determine the resistance using Ohm's Law:

$$R = \frac{V_{\text{bias}}}{I}, \tag{3.4}$$

where V_{bias} is the bias voltage and I is the current measured. Applying equantion 3.4 to our sample data, we calculate:

$$R = \frac{(10\text{ mV})}{(8.6176\ \mu\text{A})} = 1.16\ \text{k}\Omega. \tag{3.5}$$

Once knowing the resistance, we can then determine the sheet conductance (2D conductivity), of the graphene channel with width 1.89μm and length 1.85μm:

$$\rho = R\frac{W}{L} \tag{3.6}$$

where W and L are the channel width length respectively. The sheet conductance G is simply the inverse of the sheet resistance (2D resistivity), and thus $G = 0.840$mS.

$$\rho = (1.846\ \text{k}\Omega)\,\frac{(1.89\ \mu\text{m})}{(1.16\ \mu\text{m})} = 1.19\ \text{k}\Omega \tag{3.7}$$

A graphene flake lying on Si/SiO_2 substrate forms a parallel plate capacitor with the Si gate, with a dielectric SiO_2 layer. For a supported graphene sample on a 300 nm thick layer of SiO_2, the device capacitance per unit area is

$$C' = \frac{C}{A} = \left(\frac{\epsilon\epsilon_0 A}{d}\right)\frac{1}{A} = \frac{\epsilon\epsilon_0}{d} \tag{3.8}$$

$$C' = \frac{(3.9)(8.854\times10^{-12}\ \frac{\text{F}}{\text{m}})}{(300\ \text{nm})} = 11.51\frac{\text{nF}}{\text{cm}^2} \tag{3.9}$$

where C is the parallel-plate gate capacitance, A is the surface area of the graphene channel, ϵ is the relative permittivity of SiO_2, ϵ_0 is the permittivity of free space, and d is the oxide thickness. Knowing that the Dirac point is at a gate voltage at which the conductance is a minimum, in this case 16.40 V from figure 3.18b, we may now calculate the gate-induced charge carrier density

$$n_\text{G} = \frac{C'(V_\text{G} - V_\text{D})}{e} \tag{3.10}$$

$$n_\text{G} = \frac{(11.51\frac{\text{nF}}{\text{cm}^2})[(-10.002\ \text{V}) - (16.40\ \text{V})]}{(1.602\times10^{-19}\ \text{C})} = 1.897\times10^{12}\ \text{cm}^{-2} \tag{3.11}$$

where V_G is the applied gate voltage, V_D is the Dirac point gate voltage, and e is the elementary charge [31]. Next we calculate the electron mobility according to

$$\mu = \frac{\sigma}{ne} \tag{3.12}$$

$$\mu = \frac{(0.840\ \text{mS})}{(1.897\times10^{1}2\ \text{cm}^{-2})(1.602\times10^{-19}\ \text{C})} = 2,764\ \frac{\text{cm}^2}{\text{V s}} \tag{3.13}$$

where σ is the sheet conductance, and n is the total charge carrier density. As long as we are considering far enough away from the Dirac point, then we can neglect residual charge carrier density and n is approximately n_{G}. We can calculate the electron mean free path from

$$\ell = \sqrt{\frac{n}{\pi}}\frac{\mu h}{2e} \tag{3.14}$$

$$\ell = \sqrt{\frac{(1.897 \times 10^{12}\ \mathrm{cm}^{-2})}{\pi}}\frac{(2,764\ \frac{\mathrm{cm}^2}{V\ s})(6.62607 \times 10^{-34}\ \mathrm{J\ s})}{2(1.602 \times 10^{-19}\ \mathbf{C})} = 44.4\ \mathrm{nm} \tag{3.15}$$

where h is Planck's constant [31]. This mean free path describes the average distance an electron may travel without experiencing a collision, and can be a measure of cleanliness of device, as this value will decrease as defects increase.

Finally, we can calculate the transit time for a single electron to travel from one electrode to the other through the graphene channel,

$$\tau = \frac{L^2}{\mu V_{\mathrm{b}}} \tag{3.16}$$

where L is the length of the channel, μ is the charge carrier mobility, and V_{B} is an applied bias voltage [6]. Applying equation 3.16 to our sample, we find:

$$\tau = \frac{(1.85\ \mu\mathrm{m})^2}{(2,764\ \frac{\mathrm{cm}^2}{\mathrm{V\ s}})(10\ \mathrm{mV})} = 12.4\ ps. \tag{3.17}$$

3.4.3 Contact Resistance and Mobility Estimates

In order to estimate the mobility of charge carriers in our devices, we employ the Fitting Transconductance Method (FTM), as demonstrated in Yigen 2014 [32]. From a typical gate sweep acquired in the dark, we can plot the device resistance against charge density, as shown in figure 3.19 with data borrowed from Yigen 2014 [32].

The resistance of the graphene device vs charge density is described by

$$R = R(n_{\mathrm{G}}) = R_0 + \frac{1}{\frac{n_{\mathrm{G}} e \mu W}{L} + G_{\mathrm{CNP}}}, \tag{3.18}$$

where R_0 is the series contact resistance, W/L is the graphene channel aspect ratio, e is the fundamental charge, n_{G} is the gate-induced charge carrier density, and G_{CNP} is the device

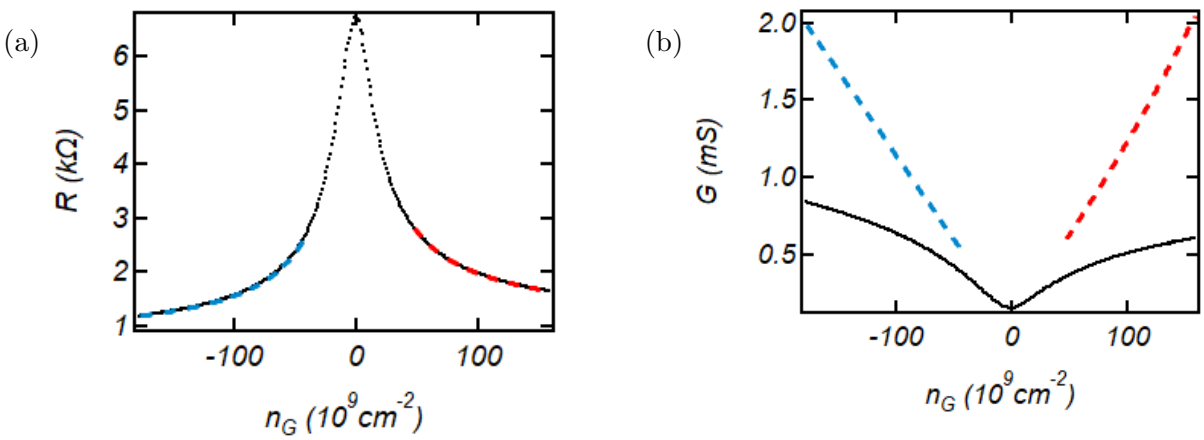

Figure 3.19: Estimation of contact resistance and charge carrier mobility via FTM analysis. (a) From gate sweep data, we plot device resistance vs gate-induced charge carrier density. The tails of the curve can be fitted using equation 3.18. Fits on the example data borrowed from Yigen 2014 yield series contact resistances $R_0 = 1,172\ \Omega,\ 695\ \Omega$ and carrier mobilities $\mu_{\mathrm{e,h}} = 75,800\ cm^2\ V^{-1}\ s^{-1},\ 66,000\ cm^2\ V^{-1}\ s^{-1}$ for electrons and holes respectively [32]. Positive (negative) charge density corresponds to a graphene channel doped with electrons (holes). (b) Device conductance (black). The blue and red traces represent the conductance after the contact resistance for charge carriers has been subtracted at hole-doped and electron-doped charge densities. Figures recreated from Yigen 2014 [32].

conductance at the charge neutrality point. By applying equation 3.18 to the data shown in figure 3.19a, the fit parameters yield series contact resistance $R_c = 1,172\,\Omega$ ($R_c = 695\,\Omega$) and charge carrier mobility $\mu_e = 75,800\ cm^2\ V^{-1}\ s^{-1}$ ($\mu_h = 66,000\ cm^2\ V^{-1}\ s^{-1}$) for electrons (holes) [32]. These correspond to mean free paths of $\ell_e = 884\ nm$ and $\ell_h = 770\ nm$. Note that this example device is much shorter than those presented in Chapter 4, and measurements were made under vacuum at cold temperatures.

3.5 Raman Spectroscopy on Graphene

3.5.1 Measurements

Raman data is acquired at a constant gate voltage by illuminating a focused beam of 532 nm light at a constant output power onto an approximately 0.9 μm diameter spot and recording the reflected, Raman-shifted light with a CCD camera for a predetermined acquisition time. The spectra acquired are sensitive to structural properties of the lattice, and spectral features may change as a function of lattice temperature, disorder, externally-applied electric field, or other parameters. The laser used for Raman itself acts as a heat source, particularly at sufficiently high power settings. Graphenes characteristic Raman spectra will be analyzed according to its D, G, and 2D spectral features.

3.5.2 Analysis

Raman yields a wealth of information about the crystallographic structure of graphene. The first information to extract is a quantitative determination of the layers of graphene by evaluating the ratio of areas under the Raman G and 2D peaks.

The second piece of information to extract is the interdefect distance and defect density. Exfoliated graphene like ours tends to be very clean, as is evidenced by the low height of the D-peak with respect to the G-peak seen in figure 3.21b. From the data, we curve fit the two peaks with a Lorentzian function, then calculate the area ratio of the peaks from the results:

$$\left(\frac{I_D}{I_G}\right) = \frac{(14180.2)}{(964977)} = 0.0146949. \tag{3.19}$$

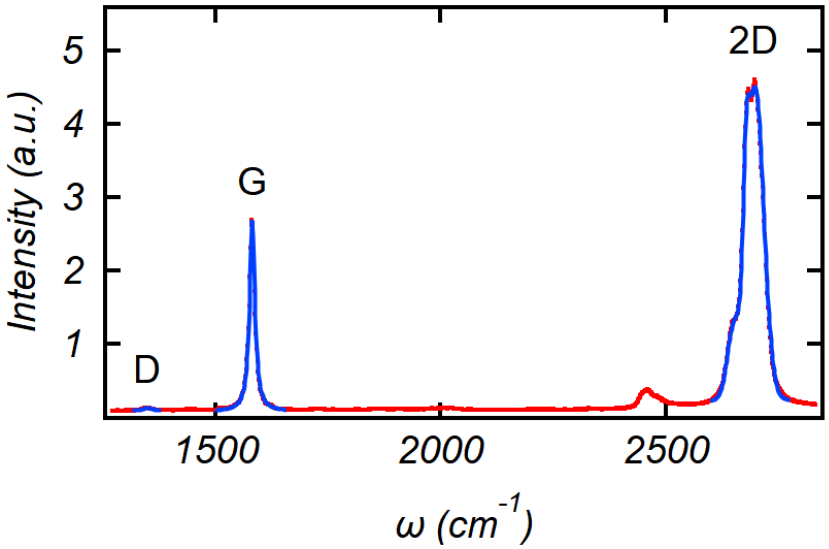

Figure 3.20: Sample Raman spectrum of a graphene flake, with fitted, labeled peaks. From the size and shape of the 2D peak, we qualitatively conclude that this sample is bilayer by the shape and height of the 2D peak.

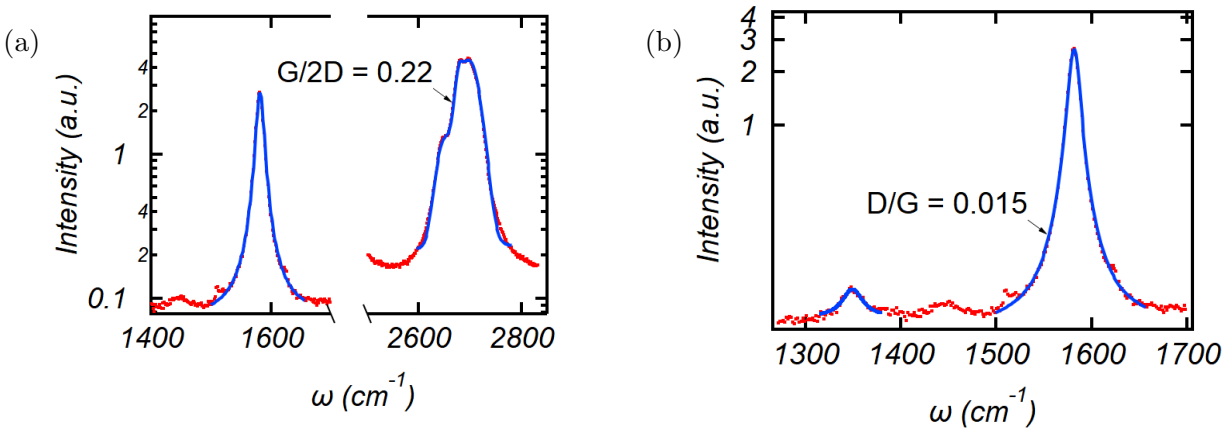

Figure 3.21: Raman ratio analysis of a sample graphene flake. (a) The ratio of areas under the G and 2D peaks is 0.22, which is consistent with bilayer graphene. (b) The ratio of areas under the D and G peaks is 0.015, which corresponds with an inter-defect density of 100 nm and a defect distance of 3.2×10^9 cm^{-2}.

Next we can determine the interdefect distance according to

$$L_{\mathrm{D}} = \sqrt{\frac{\left(4.3 \times 10^3 \text{ nm}^2 \text{ eV}^4\right)}{E_{\mathrm{L}}^4} \left(\frac{I_{\mathrm{D}}}{I_{\mathrm{G}}}\right)^{-1}} \tag{3.20}$$

$$L_{\mathrm{D}} = \sqrt{\frac{\left(4.3 \times 10^3 nm^2 \mathrm{eV}^4\right)}{\left(2.33 \mathrm{eV}\right)^4} \left(0.0146949\right)^{-1}} = 99.6 \text{ nm} \tag{3.21}$$

where E_{L} is the energy of a single photon from the laser. The equation used is valid for the low-density defect regime in which the D peak is much smaller than the G peak. Interdefect distances less than ˜ 8nm require treatment with another model. Knowing the interdefect distance, we can then calculate the density of defects in the graphene lattice:

$$n_{\mathrm{D}} = \frac{1}{\pi L_{\mathrm{D}}^2}. \tag{3.22}$$

Calculating the defect density according to equation 3.22, we find

$$n_{\mathrm{D}} = \frac{1}{\pi \left(99.6 \text{ nm}\right)^2} = 3.21 \times 10^9 \text{ cm}^{-2}. \tag{3.23}$$

The defect density quantifies the structural cleanliness of the device, averaged over the area illuminated by the laser spot. Structural defects, such as missing carbon atoms, edges, dopants, interfaces with other materials, and more, may act as scattering sites not only for the phonons, but for the electrons as well.

3.6 Photocurrent Microscopy on Graphene

In Raman experiments, the laser is used to probe the graphene structure. In photocurrent microscopy, it is used to locally perturb, or gate, the electrical behavior of the graphene. Two types of measurements can be used in order to determine the photocurrent induced by laser beam excitation: the photoconductive method, and the photocurrent method. The photoconductive method consists of a bias sweep under illumination, the linear fit of which will directly yield three photocurrent device properties in its fit parameters: open-circuit voltage, photo-illuminated resistance, and photo-induced current. The photocurrent method is by measuring the current in a device under illumination at constant bias bias voltage for several seconds. A special case of this type of measurement is taken at $V_{\mathrm{B}} = 0$, and is often

referred to as short-circuit photocurrent. Furthermore, the device photoresponse can be used to characterize it as a photodetector. All of the photocurrent maps and optical power sweeps present in Chapter 4 were acquired using the photocurrent method.

3.6.1 Photoconductive Measurement Method

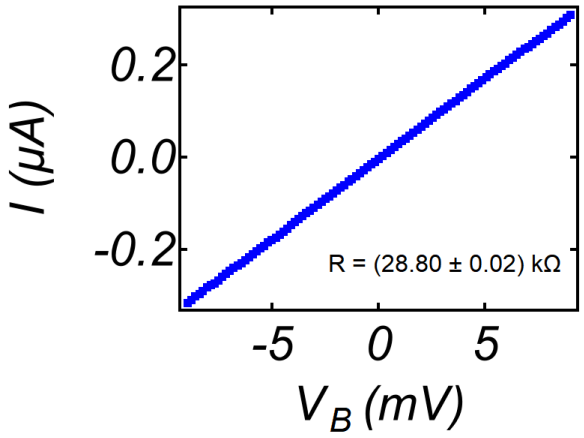

Figure 3.22: Sample photocurrent extraction from bias sweep of an example graphene device, with fit parameter results for photocurrent, open-circuit voltage, and resistance. When measured without illumination as in this sample, extracting I_{ph} and V_{OC} can be useful for testing the zeroing of our current preamplifier.

Figure 3.22 shows a sample bias sweep acquisition from an example device. Three parameters are extracted from a linear fit of the data: device resistance, photocurrent offset, and open-circuit voltage. The data is fit according to

$$V = V_{\mathrm{OC}} + RI \tag{3.24}$$

where V is the voltage across the device, V_{OC} is the open-circuit bias voltage for which a zero current is produced, R is the device resistance, and I is the device current. To determine the photocurrent, we set $V = 0$ and solve for I:

$$I_{\mathrm{ph}} = -\frac{V_{\mathrm{OC}}}{R}, \tag{3.25}$$

where I_{ph} is the photocurrent generated. In graphene, photocurrent tends to have a negative contribution to the total device current. It is expected that the device resistance will not change with laser excitation, but this may not be true for sufficiently high excitation.

Making the previous measurement at varied optical excitation power, we can deduce the dominant photocurrent mechanism in graphene. First we plot the photocurrent vs the incident power , then focus our attention on the region which is above the noise floor and below the photocurrent saturation regime. We fit the data according to

$$I_{\text{ph}} = \alpha P^{\beta} \tag{3.26}$$

where α and β are fit parameters and P is the optical input power. According to theory, the result will yield $\beta = 1$ if the photovoltaic effect dominates and $\beta = 2/3$ if the photothermoelectric effect dominates. Measurements often yield a value between these limits, indicating that both effects have non-negligible contributions to the total photocurrent.

$$G = R^{-1} \tag{3.27}$$

$$\sigma = \frac{L}{W} G \tag{3.28}$$

Photoconductivity is the portion of the total device conductivity that is due to photo-induced charge carriers, and is determined by

$$\sigma_{\text{ph}} = \Delta\sigma = \sigma_{\text{illuminated}} - \sigma_{\text{dark}}. \tag{3.29}$$

Characterizing the device as a photodetector, we can determine its gain from

$$\text{Gain} = \frac{\left(\frac{I_{\text{ph}}}{e}\right)}{\frac{A_{\text{G}}}{A_{\text{L}}}\left(\frac{P\eta}{h\nu}\right)} \tag{3.30}$$

where e is the elementary charge, A_{G} and A_{L} are the respective areas of the graphene channel and laser spot, $h\nu$ is the energy of a single photon of excitation light, P is the optical input power, and η is the absorption coefficient of graphene ($\sim 2.3\%$) [6][7]. Gain is essentially a metric of efficiency for how many electrons are excited to produce photocurrent by a single photon. The performance of a photodetector can be characterized its specific detectivity:

$$D = \frac{I_{\text{ph}}}{P\sqrt{2eI_{\text{dark}}}} \tag{3.31}$$

where I_{dark} is the current at zero bias without laser excitation, and I_{ph} is the photocurrent under illumination [6][7].

For characterizing our device performance, we will focus on using device photoresponsivity which is a measure of how much current, or voltage, is generated per incident optical power. The equation used for photoresponsivity is

$$\mathcal{R} = \frac{I_{\text{ph}}}{P_{\text{opt}}}, \tag{3.32}$$

where $\mathcal{R}$ is photoresponsivity, I_{ph} is the photo-generated current, and P_{opt} is the incident optical power [7].

3.6.2 Photocurrent Measurement Methods

We apply a constant bias and gate voltage to a device under illumination of constant optical power and measure the drain current for several seconds, followed by the same measurement under no illumination (dark). We then subtract the average of the dark current as background from the average photocurrent. Because the photo-bolometric effect depends on bias voltage across the sample, we apply $V_{\text{B}} = 0$ to guarantee that our measured photocurrents can only be due to either the photovoltaic or photo-thermoelectric effects.

3.6.3 Mapping and Combined Measurements

Laser excitation is a necessary component for the acquisition of Raman data in our graphene devices, but it also perturbs the device in two ways: sample heating and photocurrent generation. These effects may vary with laser spot position and can be investigated via spatially-resolved mapping of opto-electronic measurements. Extracted parameters, such as electron mean free path, lattice defect density, and photocurrent generation, may exhibit different behaviors based on whether the laser spot is probing near an edge, a contact, or the center of the graphene channel.

For each acquisition, we define a Raman map in WiRE to scan the focused laser spot within a square region surrounding the graphene channel at constant optical power. For each pixel in the map, we may simultaneously acquire a bias, gate, or both sweeps as WiRE acquires spectrum. Relevant data is processed as in the previous sections, and plotted as a function of laser spot position with respect to the graphene channel. Alternatively, PhotoMod can

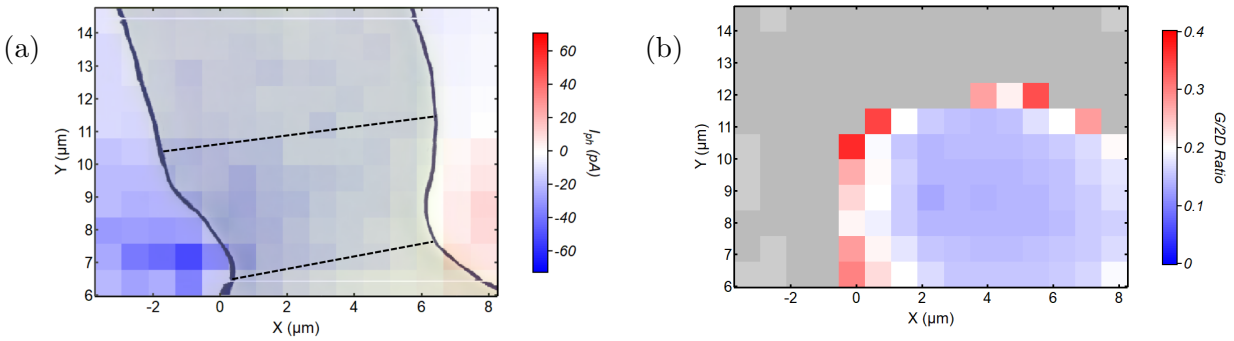

Figure 3.23: Photocurrent and Raman maps of a graphene FET acquired simultaneously. (a) Source-drain current was measured under laser illumination for each laser spot target coordinate (x,y). The black outline represents the edges of the gold contacts which were created using photolithography. (b) Raman spectra were recorded for each laser spot position as in the photocurrent map. Raman features, such as peak positions and FWHM, can each be plotted vs position. When there is insufficient Raman signal, the fit extraction fits background noise features, yielding extreme, meaningless values which can be removed (gray). (a) and (b) are plotted with the same spatial axis scaling and range.

run in scanning photocurrent mapping (SPCM) mode, which acquires a single measurement of photocurrent at each map coordinate. Shown in figure 3.23 are a photocurrent map a simultaneously acquired 2D peak FWHM map on an example device. The outlines show the locations of the gold contacts.

3.7 Reducing Spatial Drift and Mechanical Vibration

When we first accomplished assembling our apparatus to accommodate measuring photocurrents, a spatial drift was observed resulting in difficulty repeating measurements or even acquiring. Over time, I determined and addressed the primary contributions to this error: wire stiffness, optical bench vibrations, room temperature instability, and heating due to white light source.

The stiffness of the electrical wires connecting the sample holder to the measurement circuit resulted in a hysteresis of directional movement on the order of tens of micrometers. By replacing the wires with thinner cables, we were able to recreate the same quality transport measurements while also improving motor position uncertainty by at least an order of

magnitude.

The Raman microscope system initially was located on the fifth floor of a building, and only had weak, passive vibration damping. Under these conditions, vibrations from shaking in the building, nearby construction outside, heavy footsteps, or opening cabinet doors would result in jumps of several microns which would take more than a few seconds to recover. Furthermore, the motor positions could vary slightly from the spatial positions viewed through the microscope after such shocks and drift would accumulate over time. To address this, the system was moved onto a Newport vibration isolated workstation with pneumatic vibration isolation. Once in place, all visible vibration from the building or shocks in the room completely disappeared, drastically improving observed drift.

Another source of drift came from the microscope coarse adjustment. I found that if the coarse adjustment was used to raise the microscope stage and then subsequently the fine adjustment motor is used to lower it, then the coarse adjustment would turn along with the fine adjustment a fraction of a turn before settling. This behavior was not observed when the fine adjustment was used to raise the stage. If the fine adjustment motor was not used, or not used sufficiently, after raising the stage via coarse adjustment, then the focus of the microscope would tend to drift over time. Therefore proper procedure is to lower the stage to its minimum position via the motor, then raise the stage back into focus again with the motor.

With the above considerations, sometimes there would be no observable drift experienced, but at other times there the drift could range from the order of microns per hour to microns per minute. Considering such variation, I observed temperature patterns inside the lab and outside the building. I noticed that on sunny Summer days, the lab temperature fluctuated $\pm 3°C$, but on cloudy or cool days it would only fluctuate within $\pm 0.5°C$. Furthermore, I observed large drifts on the days with large lab temperature fluctuations and none when temperature was much more stable.

Finally, I observed that some steady drifting occurred within the first few hours after turning on the white light illumination source. By turning this on at least 3 hours in advance and taking all the above consideration, I was able to achieve motor stage position certainty repeatably within about 0.2 μm.

3.8 Laser Annealing and Measurement Protocols

As shown in Chapter 2, laser annealing can be used to remove surface impurities, including moisture condensation, PMMA, and other polymers. Conductance of a monolayer device scales linearly with relative humidity, with adsorbed water and oxygen increasing conductivity by doping the graphene channel with holes. Early in our photocurrent experiments, we noticed a time-dependent behavior in electron transport data. As shown in figure 3.24, the device will undergo a measurable change during laser illumination. As the laser impinges on the sample, we noted that the Dirac point shifts in the direction of negative gate voltage, indicating a reduction in hole doping. As discussed back in chapter 2, laser excitation may burn away excess materials leftover from the fabrication process, or it may evaporate condensation from the surface of the graphene. Because the change due to the laser was observed to be reversible, we believe the latter hypothesis to be the most likely. Water molecules adsorbed to the surface of the graphene trap electrons within the graphene channel, effectively changing the charge density within the channel by doping it with holes and thus shifting the Dirac point in the positive gate voltage direction [16][11]. By removing these surface molecules, their gating effect is removed and the Dirac point shifts nearer its intrinsic value. This time-dependent change in charge doping eventually reaches a steady state and the Dirac point ceases to shift, as seen in figure 3.24b. At this point the surface moisture has been removed and the sample is ready for testing.

However after illumination ceases, the charge doping anneal will begin to recover as moisture begins to re-accumulate. In fact the observed changes due to annealing were completely reversible, eventually returning to their initial state after several hours, as seen in figure 3.25. Observing no change in the Raman structural defect peak (D-peak) and the process being reversible, we concluded that the change must be due to the laser warming the device, removing surface adsorbants such as water, followed by moisture slowly re-adsorbing to the channel surface after illumination is removed. Although full recovery can take several hours, most of the recovery occurs within the first several minutes, and thus it was necessary to acquire our photocurrent measurements as quickly as possible, often under 1 minute, in order to measure graphene in the annealed state before significant recovery can occur.

Finally, we must ensure that the laser annealing is uniform across the entire channel. To determine the best procedure, we tested 3 annealing procedures: focusing the laser spot at the channel center, line-scanning the laser spot along the length of the channel, and raster-scanning the laser spot in a 2D region encompassing the device. Each method was performed

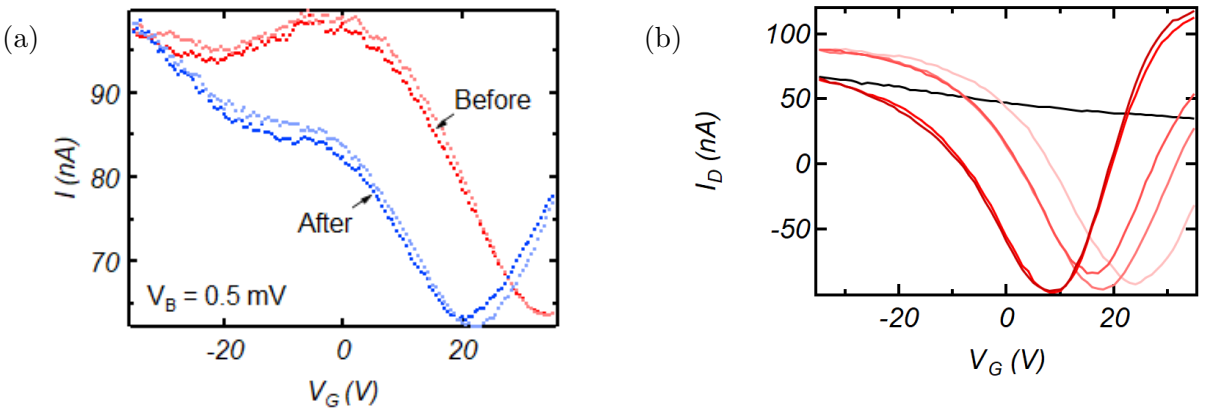

Figure 3.24: (a) Example demonstration of annealing on device before and after a 2D mapping experiment, demonstrating a change in the charge doping after laser illumination which is illustrated by a significant shift in the Dirac point. Red curves were acquired before a 2D map, and blue curves immediately after. Both red and blue were acquired sweeping V_{G} negative to positive, then positive to negative. (b) Repeated gate sweeps under laser illumination, approaching steady state. The black trace was acquired in the dark before illumination, exhibiting a Dirac point that is far beyond the measured voltage range. Red curves were acquired under illumination in succession, where darker red represents more recent. Note that during illumination the Dirac point shifts in the negative voltage direction until it settles into a final position. This stabilized position is repeatable, and indicates that the device is annealed.

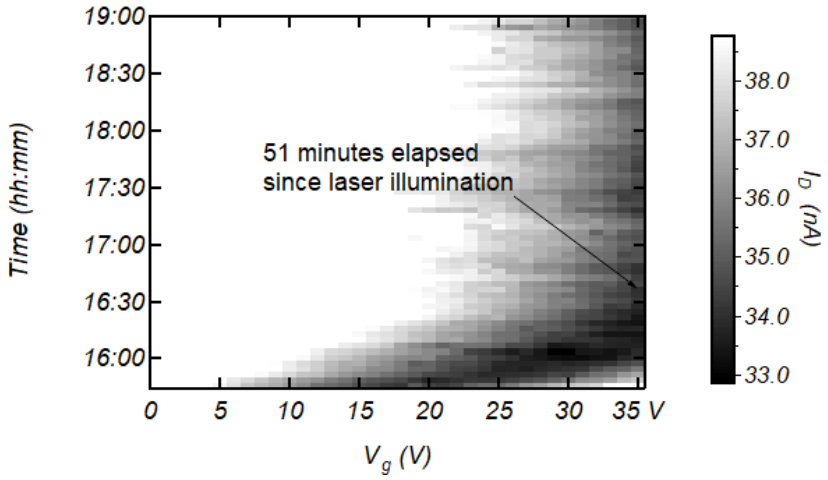

Figure 3.25: Gate sweeps relaxing to initial state after laser is illumination discontinued. It is shown that the device will relax near to its pre-illuminated state about 1 hr after removing laser illumination. For repeatable annealed current results, sweeps should be acquired within ~ 2 minutes after anneal, with more leeway allowable for higher laser power acquisitions.

repeatedly to show reproducibility of the anneal. Aiming at the channel center took several minutes to anneal devices greater than the width of the laser beam, and was less reliable as the channel dimensions increased. Scanning the laser across the length of the channel proved reliable and efficient for narrow devices whose widths were less than or equal to the beam width. The raster scanning method was the most robust and universal method, especially for larger dimensions. This is because it would uniformly and repeatably anneal a device, no matter its dimensions. For example, a beam spot focused on the center or side of a large graphene flake may eventually reach a steady anneal state, but the accumulated moisture across the device may not be uniform and the resulting anneal would be dependent on the spot position.

The ideal annealing method must uniformly anneal the device, yield repeatable results, minimize hysteresis, and cause no damage or irreversible changes to the device.

3.8.1 Photocurrent Mechanism Extraction "Descend" Method

The advantage of the "descend" method is in its speed. To determine the photocurrent mechanism as outlined in Chapter 2, we must acquire the photoresponse at many laser power settings for a single (x,y) spatial coordinate. We begin by focusing our laser beam on the desired location, then shutter the laser. Our custom electrical acquisition software is

then set to record the drain current at a rate of about 7.70 Hz and for a duration longer than necessary to complete the measurement set. Next, we start the power meter log using the software included with the PM160 and engage drain current measurements. The power meter data file includes timestamps, which can be used to correlate power measurements with a particular map pixel or electronic measurement. This is especially important for quantifying photoresponsivity. We now unshutter the laser at the highest desired optical power for several seconds, shutter the laser and decrease the optical power, and repeat the reduction of laser power until the minimum desired laser power is recorded. At this point the data set is complete, so the measurement software are disengaged. We now have two data files, one including laser power and time throughout the experiment, and the other including current.

First, we load the data files into Igor Pro via custom functions, and plot the laser power vs time. Because the electrical acquisition is indexed without a time stamp, we compare it to the power meter data by first scaling the index spacing by about 0.13 seconds, then shifting the time axis offset such that the dark and illuminated data regions between the power and electrical measurements line up. From here we see which powers settings correspond to which photocurrent responses. For each region of illuminated and unilluminated data, we calculate averages and standard deviations of both power and current measurements. Finally, we can run my Igor function **PowerLawPlot** on the processed data, which does several things: first, it subtracts the baseline from the measured current, second it calculates the log_{10} of the input data and the standard deviations according to

$$\delta log_{10}(y) = \frac{1}{ln(10)} \frac{\delta y}{y}, \tag{3.33}$$

and third it plots the result with error bars and a weighted linear fit over all the data. The slope of this linear fit of the log plot is reported as the photocurrent exponent. The initial result does not take into account any noise floor or power saturation regimes, therefore this value needs to be recalculated by manually selecting the appropriate range of data for linear fitting.

This method is the fastest way to acquire the photocurrent exponent, and may take up to several minutes. We anneal the device before using this method, however the annealing effect may wear off, particularly when illuminating at lower optical powers.

3.8.2 Photocurrent Mechanism Extraction "GoTo" Method

The "GoTo" method was developed after learning the importance of annealing samples, and includes a rigorous procedure to ensure that the device has a consistent anneal for every set of acquired photocurrent and laser power. However it is also by far the longest and most tedious procedure, often taking more than an hour to acquire a laser power sweep for a single map coordinate.

We begin by setting up the spectrometer software WiRE to make several acquisitions at the same (x,y) coordinate but each with a unique power setting. The acquisition time of each Raman spectrum is determined based on its laser power, increasing time as we lower the laser power setting. Because the laser illumination must last longer than its corresponding electrical measurement, we configure each Raman acquisition to illuminate and then wait for a software trigger before acquiring data. Next we program our annealing procedure in WiRE, which will be run before each power setting acquisition. Then we configure our custom electrical software to measure the drain current at a rate of 7.70 Hz for a total of 101 points.

Before we begin, we run our anneal procedure two or more times to ensure that the annealed state is repeatable. Once ready to proceed with the full data set, we follow this iterative process:

1. Begin laser power log and perform optical annealing procedure.
2. Engage PhotoMod to record dark current.
3. Engage the highest "GoTo" Raman spectrum acquisition in WiRE with the microscope podule adjusted for visible light. The motors drive the stage to the desired (x,y) coordinate, unshutters the laser, and waits.
4. Acquire initial position image, then switch podule to laser illumination, and then focus the laser spot if necessary.
5. Engage the custom PhotoMod measurement software and wait until it completes.
6. Send the OUT trigger manually from PhotoMod, signaling WiRE to acquire Raman data. Meanwhile, capture an image of the laser spot.
7. Once WiRE completes, it shutters the laser. Immediately begin acquiring dark current in PhotoMod.

8. Switch the podule back to visible light, and capture an image of the device through the microscope.

9. Run the anneal procedure, engage the next-highest laser power setting, and repeat from step 3 until all laser power settings have been acquired.

Data acquired using the "GoTo" method consists of many files, including a single power meter file, a set of one illuminated and two dark currents, and a Raman spectrum file. All the data files are imported into Igor Pro 7, where we compute the average and standard deviation of data contained in each file generated by PhotoMod. The power meter log data is stored a single file, so regions of data representing dark and illuminated acquisitions are selected for averaging. These regions can be easily identified because each acquisition is preceded by a high power power anneal and the time stamp can be checked with the time stamps on the electrical acquisition filenames. We acquire the optical images to ensure that the laser spot is on-target for each acquisition and determine the spatial uncertainty of each measurement. We use the dark data for background subtraction.

3.9 Conclusions

In this chapter, we briefly presented our fabrication and packaging methods which produce two-point graphene field-effect transistors on a carrier that is compatible with any PLCC-28 socket. We also detailed our instrumentation and software modifications necessary to measure photocurrents. In order to perform simultaneous optical and electronic measurements, we interfaced and synchronized two independently operating apparatuses. To increase our available optical power settings and allow instantaneous measurement and logging of optical power, we added hardware modifications to our Raman system. To further improve the quality and reproducibility of our measurements, we transferred the Raman system to an optics bench with vibration isolation. We modified existing software to synchronize optical and electronic measurements, making automated photocurrent mapping possible. We developed measurement protocols, including warmup, annealing, and acquisition procedures.

Using the platform for opto-electronic measurements outlined in this chapter, we present the results of our newfound capabilities in the following chapter. There, we will introduce our device details and parameters and examine the photoresponse of mono- and bi-layer graphene devices as we vary laser power, charge density, and the laser spot position.

Chapter 4

Spatial Segregation and Tuning of the Photovoltaic and Photothermoelectric Effects in Graphene

In this chapter, we demonstrate the photocurrent dependence on laser power, charge density, and laser spot illumination position in graphene transistors in the grounded-source electrode configuration. These devices behave as photodetectors, where incident photons create electron-hole pairs which are then swept into a current by the presence of a built-in electric field between the uncovered region graphene and a region covered by gold contacts. First, we find that the largest magnitude of photocurrent and responsivity in this configuration to be near the contacts, with bilayer graphene transistors being about twice as photoresponsive as monolayer ones. Second, we find that the strength of an external electric field, applied via a gate voltage, increases the magnitude of the photocurrent but not the proportional contributions of each the PV and PTE effects to the total photocurrent. Third, we demonstrate that photo-generated current from a laser spot on a graphene transistor farther than the electron mean free path from the contacts is likely due exclusively to the PTE effect.

In section 4.1, we discuss details and characterization of the monolayer and bilayer graphene devices on which we performed photocurrent experiments. Next in section 4.2, we discuss the dependence of photocurrent magnitude on incident laser power. Then in section 4.3, we discuss the dependence of photocurrent on charge density. Next we investigate the spatial dependence of the photoresponse on the incident laser spot in section 4.4. Finally, we summarize our results in section 4.5.

4.1 Device Details and Charge Transport Measurements

First we selected monolayer and bilayer graphene flakes of micron-scale dimensions for devices to conduct our experiments, seen pictured in figures 4.1a-c. Devices A and B are approximately rectangular, with widths and lengths of comparable dimensions: $W_{\mathrm{A}} = 2.66\ \mu m$, $W_{\mathrm{B}} = 2.36\ \mu m$, $L_{\mathrm{A}} = 4.32\ \mu m$, and $L_{\mathrm{A}} = 4.96\ \mu m$. Device C has trapezoidal dimensions, with $L_{\mathrm{C}} = 7.55\ \mu m$, $W_{\mathrm{C\ max}} = 7.50\ \mu m$, $W_{\mathrm{C\ min}} = 4.10\ \mu m$, and a side of length $7.86\ \mu m$. The dimensions of our graphene channels are summarized in table 4.1. The Raman spectra for devices A, B, and C shown in figure 4.1d yield an integral G/2D peak intensity ratio of 0.11, 0.22, and 0.13, indicating that devices A and C are monolayer and device B is bilayer. The absence of a discernible D peak in the spectra of all three devices indicates high structural quality and low disorder, with a maximum estimate of defect density to be 10.9 μm^{-2} based on the background noise of our Raman measurements. Devices A and B will be the primary focus of our work presented because they are comparable in size and shape, and because device C exhibited strong hysteresis, high noise, and a non-rectangular shape.

Device	Width (μm)	Length (μm)	G/D Ratio	# Layers	Shape
A	2.66	4.32	0.11	1	Rectangular
B	2.36	4.96	0.22	2	Rectangular
C	$4.10 - 7.50$	7.86	0.13	1	Trapezoidal

Table 4.1: Graphene device dimensions and geometries. Devices A and B are both rectangular and of comparable dimensions, except the former is monolayer and the latter is bilayer. Device C is a larger monolayer device and trapezoidal, with one side orthogonal to the source-drain contacts.

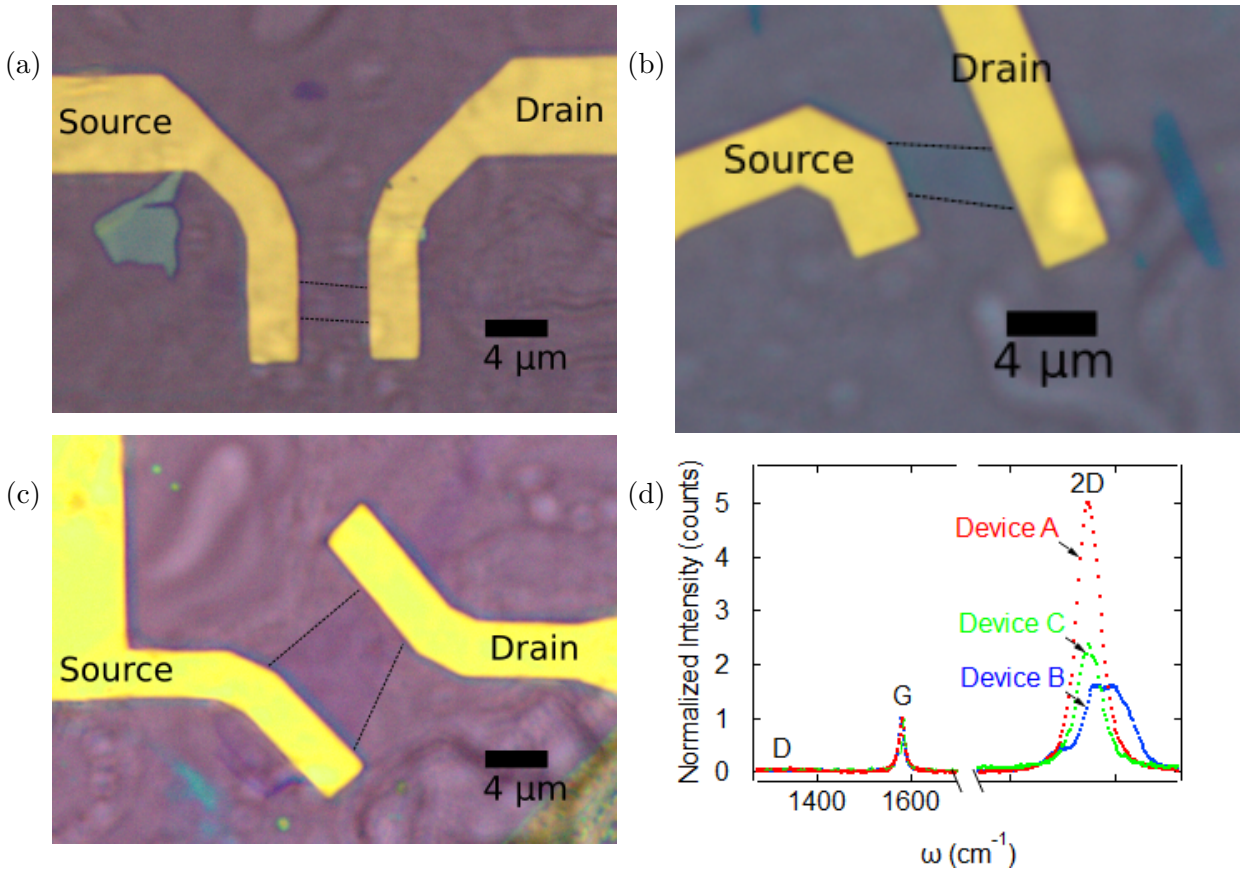

Figure 4.1: Optical images and Raman spectra of graphene devices. (a-c) Optical images of graphene devices A, B, and C as seen under a microscope at 100x magnification and their Raman spectra. The monolayer devices appear lighter, almost transparent. Lines have been added to indicate the graphene edges. (d) Raman spectra for devices A (monolayer), B (bilayer), and C (monolayer) confirming number of layers and structural quality. The lack of a discernible D peak indicates very low structural defects in the graphene lattices.

As can be seen in figure 4.2, we characterize the electron transport of our devices using bias and gate sweeps. Device A was shown to have a maximum resistance of about $R_{\max} \approx 8.639\ k\Omega$. For this device, we observed contact resistance $R_c = 4,753 \pm 19\ \Omega$ due to the contacts, a mobility of about $\mu_{\mathrm{e}} = 9,649 \pm 297\ cm^2\ V^{-1}\ s^{-1}$, and an electron mean free path of $\ell = 113\ nm$ for electrons. For holes, $R_c = 5,126 \pm 13\ \Omega$, $\mu_{\mathrm{h}} = 16,666 \pm 517\ cm^2\ V^{-1}\ s^{-1}$, and $\ell = 194\ nm$. Device B had a larger device resistance $R_{\max} \approx 16.2\ k\Omega$, $R_{\mathrm{c}} = 5.6\ k\Omega$, a hole mobility of about $\mu = 600\ cm^2\ V^{-1}\ s^{-1}$, and a mean free path of $\ell = 7\ nm$. Device C had a maximum resistance of $R = 2.915\ k\Omega$, contact resistance of $R_{\mathrm{c}} = 126\ \Omega$, a hole mobility of about $\mu = 3,739\ cm^2\ V^{-1}\ s^{-1}$, and a mean free path of $\ell = 43.6\ nm$. The contact resistances for devices A and B are rather high compared to devices found in literature, which are often hundreds of Ohms or less [33].

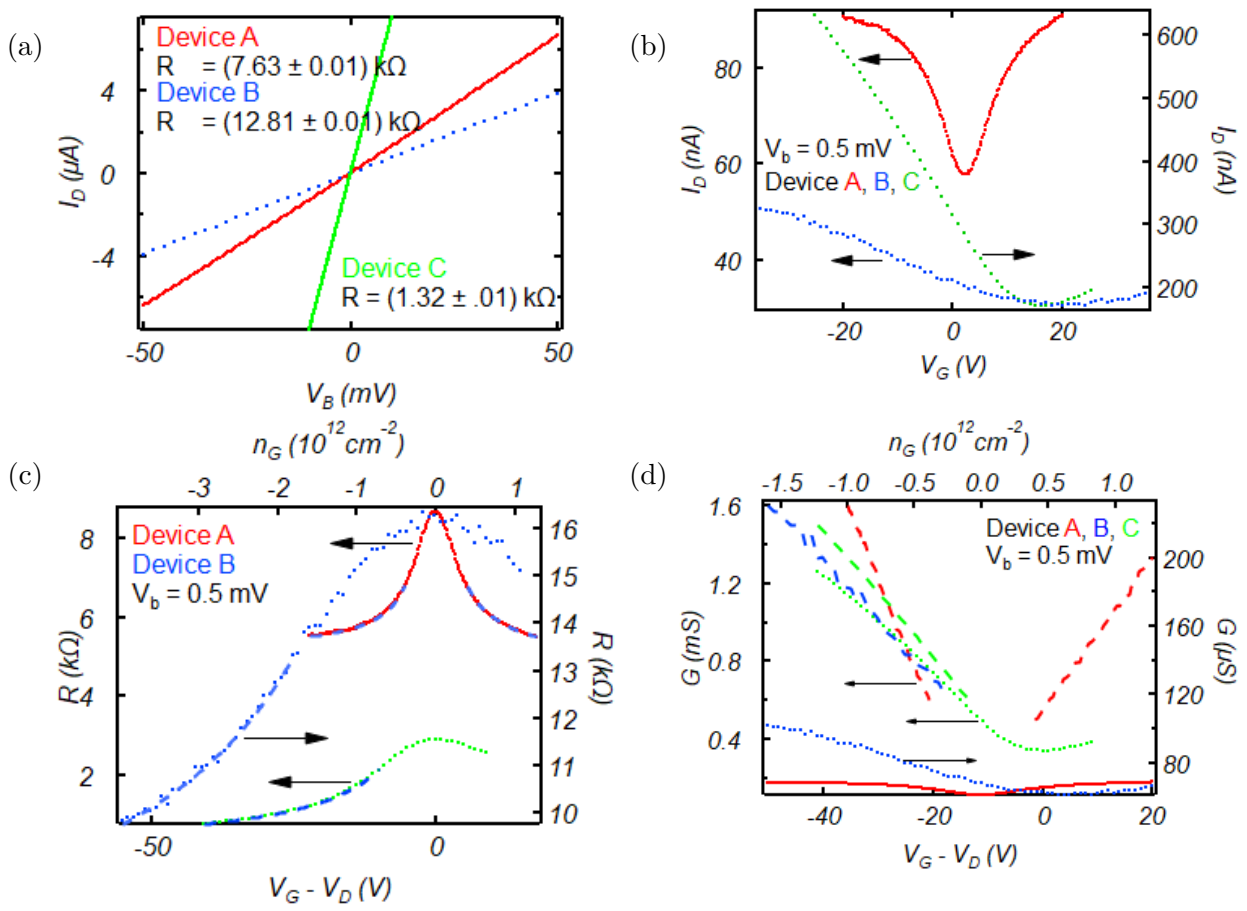

Figure 4.2: Electron transport characterization for devices A (red), B (blue), and C (green). (a) Bias sweeps of devices acquired in the dark at $V_g = 0$. Device resistance was found to be (7.63 ± 0.01) $k\Omega$ for A, (12.81 ± 0.01) $k\Omega$ for B, and (1.32 ± 0.01) $k\Omega$ for C. (b) Gate sweeps of devices acquired in the dark at $V_b = 0.5$ mV. Note that the width of the device B curve is significantly wider, indicating that it is less sensitive to changes in gate voltage. (c) Device resistance dependence on charge density for A, B, and C. Device A has mobility $\mu_e = 9,649 \pm 297$ cm^2 V^{-1} s^{-1} and contact resistance $R_0 = 4,753 \pm 19$ Ω for electrons, and for holes $\mu_e = 16,666 \pm 517$ cm^2 V^{-1} s^{-1} and contact resistance $R_0 = 5,126 \pm 13$ Ω. Device B has $\mu_h = 644 \pm 111$ cm^2 V^{-1} s^{-1} and contact resistance $R_0 = 5,501 \pm 498$ Ω for holes. Device C has hole mobility $\mu_h = 3,739$ cm^2 V^{-1} s^{-1}, and contact resistance $R_0 = 126$ Ω. (d) Device conductance with (dashed lines) and without (points) contact resistance subtracted. Note that the dependence on charge density becomes linear after contact subtraction.

4.2 Photocurrent Magnitude and Laser Power Dependence

According to the model outlined in Chapter 2, we expect that the photocurrent will relate to the incident optical power by $I_{\text{ph}} \propto P_{\text{opt}}^{\beta}$. Because we have bias voltage $V_{\text{B}} = 0$ during our experiments by grounding the source electrode, the resulting photobolometric contribution will also be zero. This simplifies our analysis, allowing us to investigate specifically the PV and PTE effects. The photovoltaic effect dominates when $\beta = 1$, and the photo-thermoelectric effect dominates when $\beta = 2/3$. When the two contributions are both present, then β will be between 1 and 2/3, depending on how much each contributes to the resultant current. Photodetector device performance is compared using photoresponsivity as a key figure of merit, and it was observed that a bilayer device outperformed a monolayer of comparable size. Since both mechanisms are proportional to charge density, we expect that for increased gate voltage there will correspond an increase in the photocurrent magnitude and no change in β.

Beginning with device A, we optically annealed the graphene and then identified a region of maximum photocurrent near the source contact, pictured in figure 4.3a. We then recorded the resultant photocurrent as we controlled the incident laser power, choosing our laser spot target to optimize the signal-to-noise of the photocurrent, as shown in figure 4.3b. According the theory for PV and PTE effects depends on photo-excited electrons reaching the built-in electric field at the graphene-contact interface. Near the drain contact could easily have been targeted instead, as this would result in the same magnitude photocurrent of opposite sign for a symmetric device. Device A exhibited a maximum photoresponse recorded of $(229.4 \pm 2.5)\ nA$ and a maximum responsivity of $(159 \pm 2)\ \mu A\ W^{-1}$. From the gate sweep shown in figure 4.3c, we can see that the channel at $V_{\text{G}} = 0$ is doped with holes with a charge density of around $0.5 \times 10^{12}\ cm^{-2}$. We also note that we find a photocurrent exponent $\beta = 0.9 \pm 0.1$, indicating that the PV effect is more prominent, contributing more than the PTE effect.

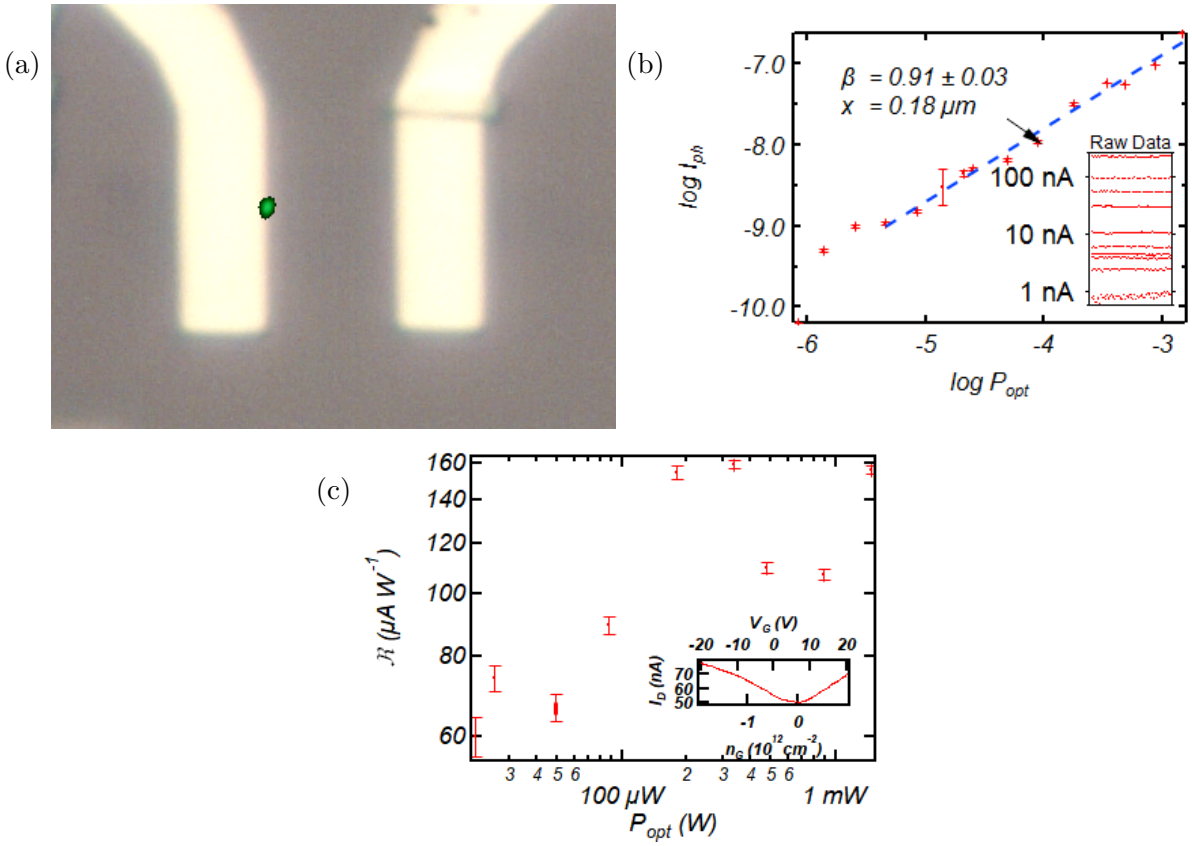

Figure 4.3: Laser power dependence of photoresponse for device A near the source contact. (a) Microscope image of bilayer device A with laser spot image superimposed, indicating the illuminated region. (b) Photocurrent vs laser power plotted on a log scale, with result from fit $\beta = 0.9 \pm 0.1$ indicating that the PV effect is the primary contributor to photoresponse, but PTE is non-negligible. Inset shows raw acquisition data, photocurrent vs time, for each laser power setting in descending order. (c) Photo-responsivity vs laser power at a distance $x = 0.18\ \mu$ from the source contact. Inset of a gate sweep acquired in the dark illustrating that during our photocurrent measurements taken at $V_g = 0$, our devices are doped with holes with very low charge density (near dirac point, but still in the linear current vs gate regime).

Next we direct our attention to our bilayer device B. Again, we choose a laser spot target near the source contact which yields the maximum photocurrent. After optically annealing the device, the maximum photoresponse and responsivity recorded were $(767.3 \pm 8.7)\ nA$ and $(371 \pm 10.1)\ \mu A\ W^{-1}$ respectively, as shown in figures 4.4b and 4.4c. Note that for $V_G = 0$, our graphene is hole-doped with a charge density of about $1.5 \times 10^{12}\ cm^{-2}$. Additionally, we find that the photocurrent exponent extracted is 1.0 ± 0.1, indicating that the photocurrent is almost exclusively due to the PV effect. This observed responsivity is larger than that recorded in the monolayer device by approximately a factor of 2, making it more desirable for photodetector applications as it has a higher signal-to-noise. However, it is rather small compared to the responsivity of other competing photodetector materials/devices which can achieve on the order of $1\ A\ W^{-1}$ or higher, albeit with longer response times. We suspect that this enhanced performance is likely due to superior optical absorption in bilayer graphene, creating about twice as many photo-excited electron-hole pairs available for transport. It may also be in part due to the predominantly photovoltaic nature of the photocurrent, considering that the PV effect is more efficient at generating e-h pairs than PTE.

Thus we have seen that for rectangular mono- and bi-layer graphene photodetectors of comparable dimensions, the PV effect plays a major role near the contacts where the photoresponse is the largest. However when we discuss the spatial dependence of photocurrent, we will see a monolayer device that is not rectangular, nor symmetric, which exhibits a different distribution of maximum photocurrent.

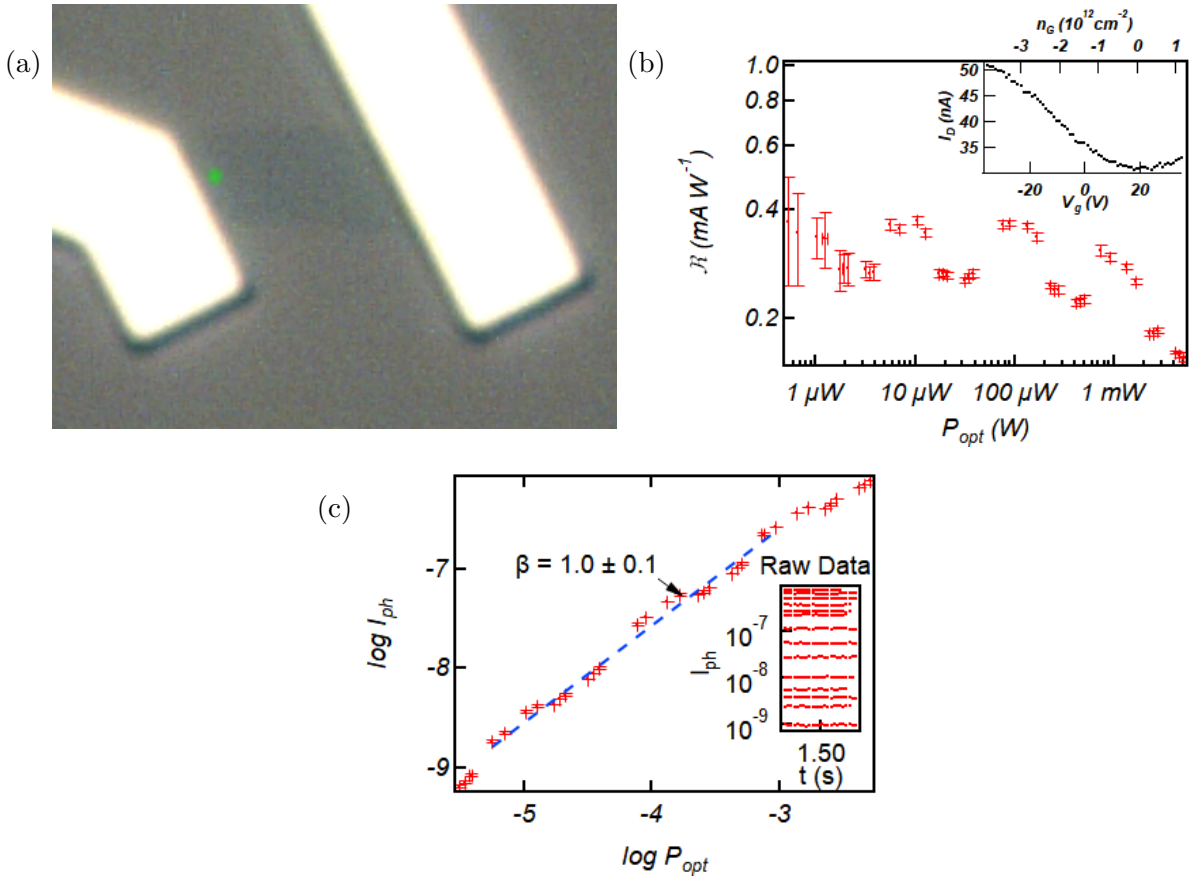

Figure 4.4: Photocurrent and responsivity measurements for Device B. (a) Microscope image of bilayer device B with laser spot image superimposed at target location. (c) Averaged laser photocurrents vs incident laser power taken in the channel center 0.18 μm from the source electrode. The inset shows the raw data used to calculate averages and std dev. (b) Responsivity measured at $x = 0.18$ μm from the source electrode. From the inset gate sweep acquired in dark, we note that our photocurrents measured $V_G = 0$ are slightly hole-doped.

Comparing devices A and B, we initially see that there is no difference in photocurrent mechanism, both yielding about 0.91 within the uncertainty of our measurement. According to Patil et al, we would expect these results to correspond to suspended graphene devices, not monolayer and bilayer devices supported on SiO_2 [1]. This may be because our experiment is performed exposed to the ambient air, or perhaps due to the lack of any significant amount of structural disorder in our devices as evidenced in our Raman spectra. Since their photocurrent mechanisms were measured to be comparable, the factor of 2 difference in photoresponsivity is likely due to the greater absorption of photons in bilayer compared to monolayer graphene. The bilayer device absorbs about twice as many net photons, and therefore has about twice as many opportunities for photons to generate electron-hole pairs contributing to photocurrent generation. We estimate our uncertainty to be at least approximately ± 0.1, considering uncertainties due to laser spot position, anneal recovery, and fluctuations in charge density (which is more profound for monolayer samples).

4.3 Charge Density Dependence of Photoresponse

According to the theory outlined in chapter 2, both the PV and PTE effects rely on a proportional relationship to a built-in electric field at the interface between the contacted and exposed regions of the graphene channel. It is understood in literature that an increase in charge density results in a larger magnitude of photogenerated current. Here we present data from device B, investigating whether the contribution of the PV and PTE effects to the total photocurrent changes with charge density. To do this, we probe the bilayer device with the same laser spot target as seen in figure 4.4a.

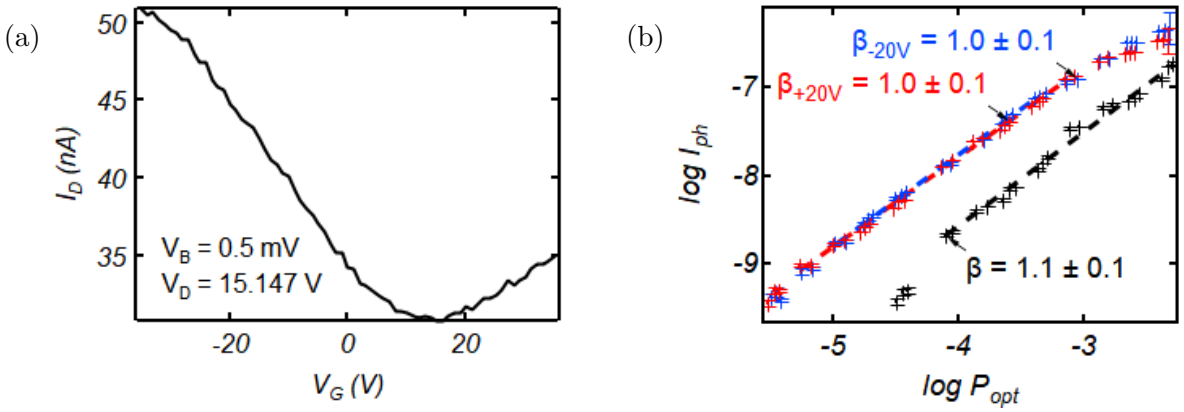

Figure 4.5: (a) Gate sweep of Device B showing a Dirac Point $V_{\mathrm{D}} = 15.15\ V$, indicating that measurements acquired at zero gate voltage will have a non-zero charge density. Laser power dependence was then measured at $V_{\mathrm{g}} = 0\ V, \pm 20\ V$ (b) Photocurrent laser power dependence at varied charge densities for device B near the source electrode for gate voltages 0V (black), -20V (blue), and 20V (red). Results for β do not significantly vary, indicating no change in photocurrent mechanisms with charge density. The magnitude of the photocurrent changes with charge density, which is due to the proportional dependence of both PV and PTE effects on charge density.

As seen in 4.5a, a gate sweep obtained without laser illumination indicates that our graphene is lightly hole-dope for $V_{\mathrm{G}} = 0$. Shown in figure 4.5b, we recorded photocurrent vs power at low hole doping ($V_{\mathrm{G}} = 0$), high hole doping ($V_{\mathrm{G}} = -20\ V$, and electron doping ($V_{\mathrm{G}} = +20\ V$. The first observation we make is that the magnitude of the photocurrent increases with increased charge density. Second, we see that at $V_{\mathrm{G}} = \pm 20\ V$, the magnitude of the photocurrent measured is approximately the same. Third, the slopes extracted from the log plotted were $\beta = 1.1 \pm 0.1$ for $V_{\mathrm{G}} = 0$ and $\beta = 1.0 \pm 0.1$ for $V_{\mathrm{G}} = \pm 20\ V$, which represents

no change within the uncertainty of our measurement. It should be noted that from the unilluminated initial gate sweep we see that $V_G = 0$ corresponds to about $n = 1.1 \times 10^{12}\ cm^{-2}$, which is about twice the charge density as in the previous experiment for the same device due to a shifting Dirac point. Gate voltages $V_g = \pm 20\ V$ correspond to charge densities of $n = 349 \times 10^9\ cm^{-2}$ holes and $3.60 \times 10^{12}\ cm^{-2}$ electrons.

From these observations we conclude that the photocurrent magnitude depends on the charge density, that in device B the most prominent photogeneration mechanism near the contacts is the PV effect, and that the relative contributions of the PV and PTE effects are unchanged with variations in charge density. That is, when the laser spot targets the region of maximum photocurrent near the source electrod, the photovoltaic effect is the largest contributor to photo-induced current. However we will see in the next section that position of the laser spot is an important factor in what photogeneration mechanisms can contribute.

4.4 Spatial Dependence of Photoresponse

By focusing our attention on how photocurrent responses are spatially distributed within a sample, we may learn more about how the PV and PTE mechanisms differ in terms of how far photo-excited electrons may scatter and contribute to photocurrent. First we consider the rectangular region around device A, as pictured in figure 4.6a. Mapping this region by simultaneously accquiring photocurrent and Raman data, we investigate the spatial dependence of photoresponse at constant optical power. In 4.6c we plot the G/2D peak extracted from the Raman spectra of each (x,y) coordinate. From this we can see that the G/2D ratio is uniformly near 0.11 when the laser spot is close enough to the graphene to obtain a Raman signal. When no significant amount of laser reaches the graphene channel, the fits used to produce the map produce extreme, random values observed as strongly red or blue pixels. Additionally, the Raman reassures us that our map did not drift off target, as the boundary between uniform signal and noise indicates the edges of the graphene channel, within the spatial resolution of our spot size. As seen in figure 4.6b, the photocurrent shows an anti-symmetric distribution of photoresponse, with the photoresponse near the source and drain electrodes to be about the same magnitude with opposite sign.

The PV effect requires that a photogenerated electron pair reach the built-in electric field at the interface between the graphene channel and the graphene directly beneath a gold contact before they can recombine. Thus we would expect the PV effect to become negligible as

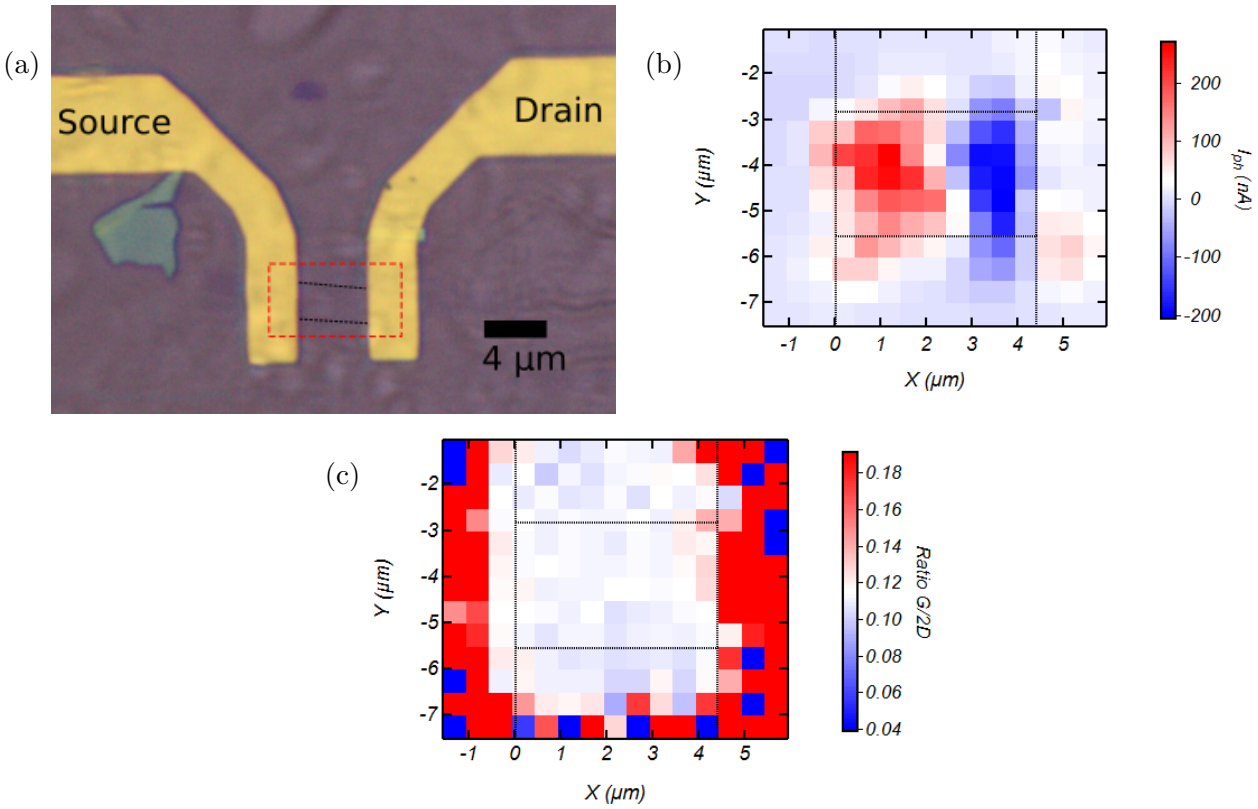

Figure 4.6: Photocurrent 2D map of Device A. (a) Optical image and (b) 2D photocurrent map of device A (monolayer), acquired at $P_{\text{opt}} = (514.4 \pm 0.16)\ \mu W$. Dashed horizontal lines indicate the edges of the graphene channel, and the vertical dashed lines represent edges of the source-drain contacts. The antisymettric sign of the photocurrent is due to the difference in Fermi level between the graphene channel and the contact nearest the laser spot. The built-in electric field at the contacts are in opposing directions. (c) Integral Raman G/2D peak ratio map acquired dudring photocurrent measurements. The device appears uniformly monolayer, with a G/2D ratio of about 0.12.

the distance between the laser spot and the nearest contact exceeds the electron mean free path. While this may also be true for the PTE effect, PTE-excited electrons have a highly elevated temperature compared to that of the graphene lattice, and therefore may effectively diffuse over an extended distance. While the PTE photocurrent would weaken as the laser spot reaches farther away from the nearest contact and fewer hot electrons are able to diffuse to the contact, we expect that it would still be effective long after exceeding the effective range of the PV effect. To investigate this, we measured the photocurrent at varied laser powers in device B both near the source contact, as pictured in figure 4.7a, and just near the channel center, as pictured in figure 4.7c. We found that exciting near the source electrode yielded a significantly higher photocurrent magnitude, with photocurrent near the source electrode ranging on the order 10^{-9} to 10^{-7} amps, whereas near the channel center, pictured in figure 4.7b, the current only ranged from 10^{-9} to 10^{-8} amps. In general the error bars near the channel center are much larger due to an inferior signal-to-noise ratio. We extracted photocurrent exponents of $\beta_{\text{source}} = 1.1 \pm 0.1$ and $\beta_{\text{center}} = 0.6 \pm 0.1$, which is a stark contrast suggesting that although the PV effect dominates near the source contact, only the PTE effect can contribute to the total photocurrent when the distance between the laser spot and the nearest contact is significantly larger than the electron mean free path.

Now considering the spatial distribution of photocurrent in device B, we acquired a 2D photocurrent map as shown in figure 4.8. We observe right away that the maximum photoresponses are nearest the contacts and have approximately equal and opposite magnitudes. This is due to the built-in electric fields at the interfaces between the graphene channel and each contact. They are equal but in opposite directions, resulting in equal but opposite photocurrents when the laser is targeted near one contact compared to the other.

Up to this point we have studied rectangular devices, where we expect an antisymmetric photoresponse as a function of laser spot position along the channel from one contact to the other. However in non-rectangular devices, such as the trapezoidal device C, we see this is no longer true. Firstly, comparing the the magnitudes of the photocurrents near the source and drain contacts, we see that the narrow end of the graphene produces a much larger photocurrent than the broad end. Additionally, the midway point shows a nonzero photoresponse, exchibiting a point of zero photoresponse closer to the broad end of the graphene.

Device C is interesting because its maximum photocurrents were not necessarily found close to the contacts, and the photocurrent produced was not symmetric as a function of position.

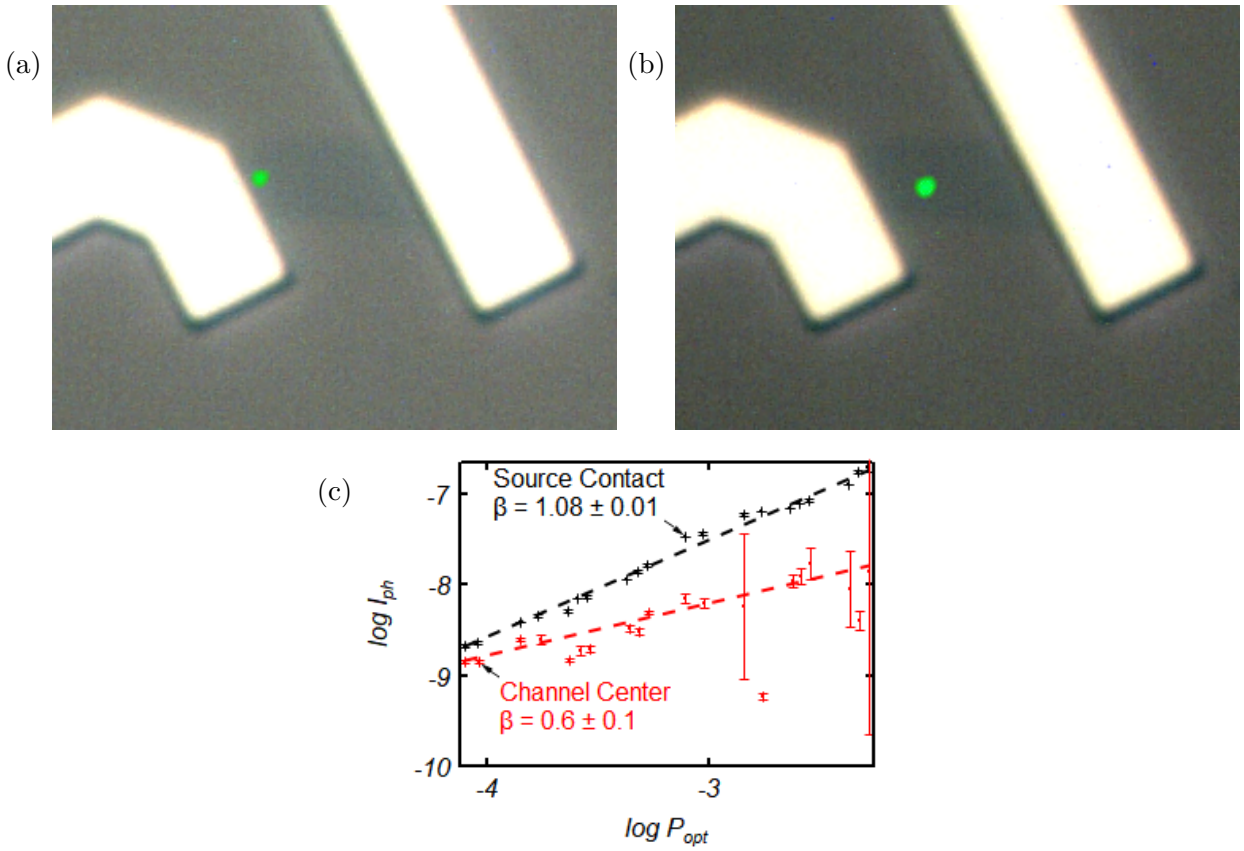

Figure 4.7: Photocurrent dependence on power and laser spot position for Device B. (a) Optical image with superimposed laser spot image, indicating laser spot position during measurement near source electrode. (b) Optical image showing laser spot position during measurement near the channel center. (c) Photocurrent laser power dependence taken near the source electrode and the center of the graphene channel of device B, yielding $\beta = 1.1 \pm 0.1$ and 0.6 ± 0.1 respectively. This indicates that the PV effect completely dominates near the source contact, but only the PTE effect contributes near the channel center.

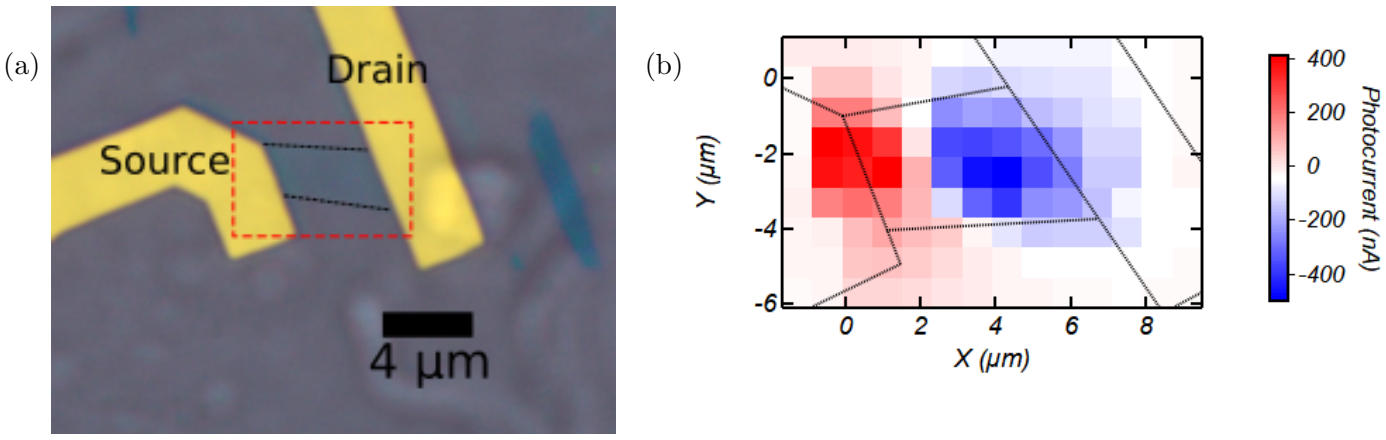

Figure 4.8: Photocurrent 2D map of Device B. (a) Optical image and (b) 2D photocurrent map of device B, acquired at $P_{\text{opt}} = (2.326 \pm 0.009)\ mW$. Dashed lines outline the gold contacts and the graphene channel.

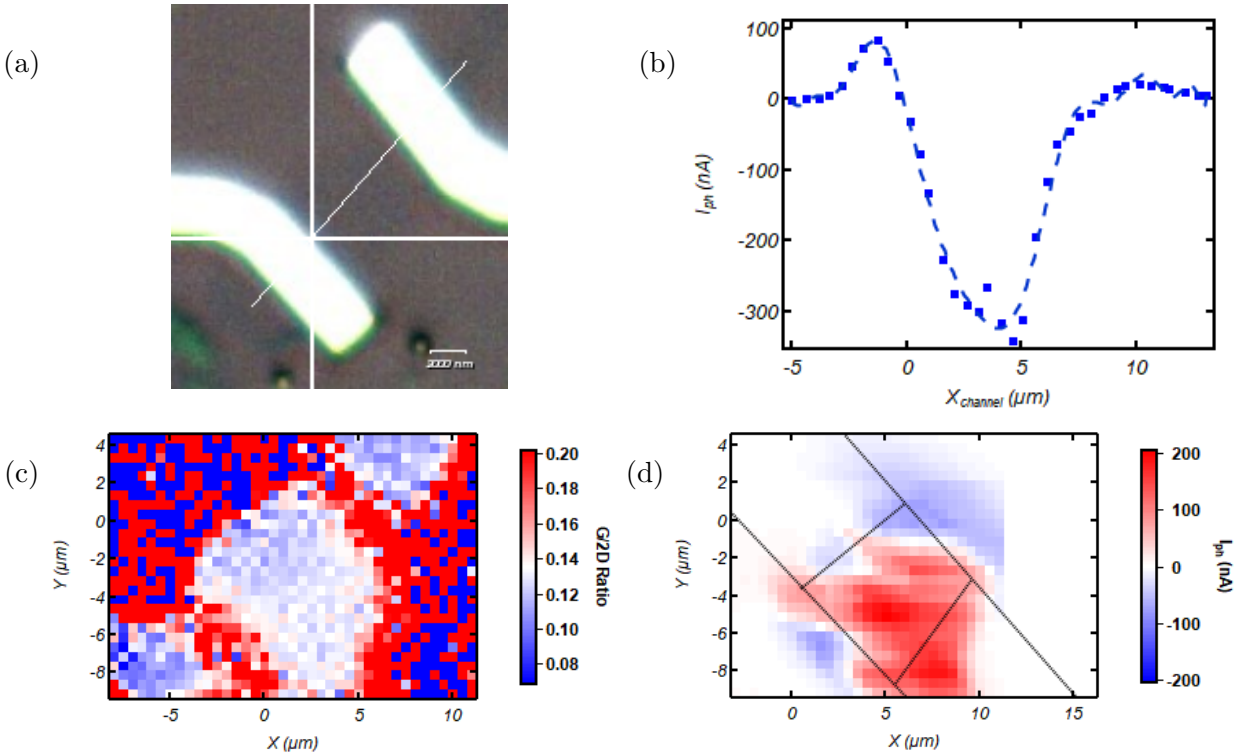

Figure 4.9: Raman maps of device C. (a) Optical image of Device C, with line map path. (b) Photocurrent line map along graphene channel of device C at constant optical power. (c) Raman G/2D ratio 2D map of device C at constant optical power. The device is uniformly monolayer, and the contacts are seen as regions lacking a Raman signal. (d) Photocurrent map of Device C, showing the spatial dependence of the photocurrent.

As is clear in the line map presented in figures 4.9a and 4.9b, the largest photocurrent was found near the narrower end of the channel, but not as near to the contacts as in devices A and B. Additionally, the higher photoresponse of the narrow side covered a much larger area of the flake than the broad side. This dependence on channel shape is an interesting feature that can be explored in future experiments. Due to its trapezoidal shape, maximum photocurrents measured varied from 84.701 nA to 342.52 nA when excited with $P_{\text{opt}} = (318.158 \pm 1.186)\ \mu W$, yielding responsivities 266.22 $\mu A\ W^{-1}$ and 1076.6 $\mu A\ W^{-1}$. This suggests that asymmetric devices may yield higher responsivities as a consequence of their shape, and thus asymmetric designs could be more desirable for enhanced photodetector performance.

However device C in particular lacked repeatability, often suffering from large hysteresis with respect to applied gate voltages, and a shifting charge density. In experiments that take a particularly long amount of time to acquire, such as the photocurrent map shown in figure 4.9d which took around 5 hours to complete, yielded inhomogeneous patterns. Compared to the line map which took several minutes, the 2D map acquisition took over more than an hour during which the charge density likely shifted. Also due to its large size, inhomogeneous charge puddles may have formed. Comparing this photocurrent map with the simultaneously acquired Raman map seen in figure 4.9c, one sees that the G/2D ratio in a region near the top left edge appears to be slightly lower than in the rest of the channel, though still well within the range expected for a monolayer. Since device C lacked any significant D peak, could possibly be attributed to inhomogenous stresses or charge traps within the channel.

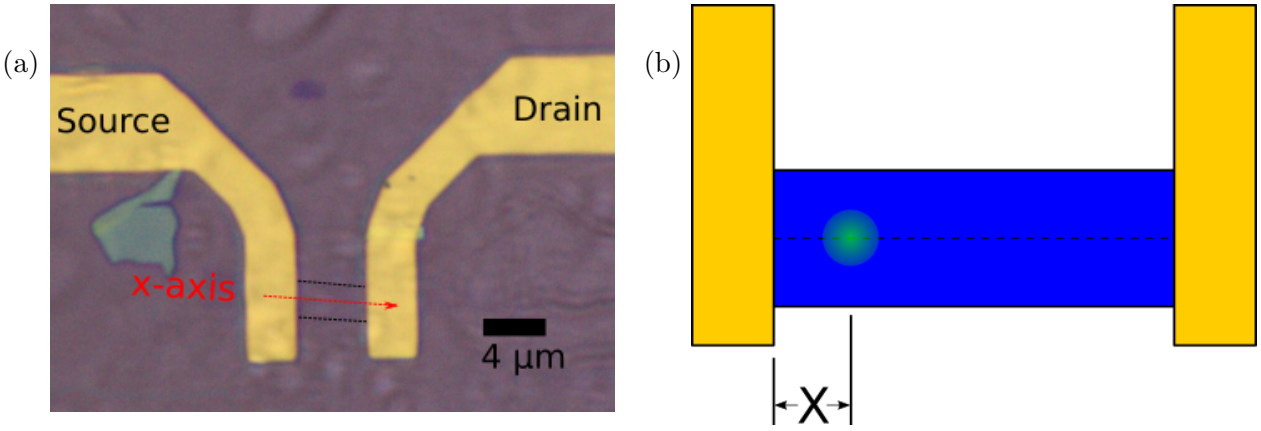

Figure 4.10: Photocurrent and responsivity line map path for device A. (a) Optical image of device A indicating path and direction of acquisition. (b) Line map diagram, defining position x as the distance from the source electrode.

Now we return our attention to device A to discuss the photocurrent dependence on optical

power as a function of laser spot position. Figure 4.10 illustrates the line map acquisition path and defines the laser spot position x along the channel as distance from the source contact. To reduce the time of the experiment, we used the "descend" method outlined in chapter 3 and optically anneal the sample before each mapping position. This resulted in an average of 30 minutes between the beginning of each power sweep and the sweep following it. We present our results in figure 4.10. We see that the absolute value of the photocurrent is greatest near the source-drain contacts with a maximum photocurrent measured at points near the contacts around 80-230 nA. However we notice there is a non-zero photocurrent near the center of the channel resulting in maximum photocurrents for each mapping point ranging between 22 nA and 46 nA, as seen in figure 4.11a. Looking at this from the standpoint of responsivity, as presented in figure 4.11b, we see that the most efficient spot locations translating photons into current are within 1 μm of the contacts, the next-best near the channel center, and the worst in-between the previous regions.

Figure 4.11c shows responsivity vs optical power for map point $x = 0.18\ \mu m$, with an inset displaying the initial unilluminated gate sweep acquired before experiments began, with $V_{\mathrm{D}} = 18\ V$. Although we did not record gate sweeps between each successive power sweep, we did at the beginning of each complete dataset. We noticed that the Dirac point had shifted by about $\Delta V_{\mathrm{D}} = 11.6\ V$ between the previous round of measurements and the start of this acquisition set.

We present our result for the photocurrent exponent β as a function of position in figure 4.11d, where we see little systematic change in the exponent along the channel. A few of the points were removed, since they lacked sufficient signal-to-noise to obtain a reliable fit of the photocurrent vs power data. Within the uncertainty of our measurement, we conclude that we observed little change in photocurrent mechanism as the laser scanned across the channel, except near the center of the channel. With the exception of one point, the central positions along the channel yielded lower values of β (between 0.80 and 0.90) than near the contacts (between 0.95 and 0.98). This may indicate that although the PV effect is not completely eliminated near the channel center, its effectiveness relative to the PTE effect is reduced. However the uncertainty of our measurements were much higher than in our bilayer device, with three map points being removed due to very low signal-to-noise. While it may be possible that with greater precision we might see a more convincing reduction in β near the center, there may be other factors interfering with the measurement. For example, shifting or fluctuating charge doping during the experiment, induced by the ambient air, may skew our values or introduce seemingly random fluctuations. It may be that monolayer graphene is

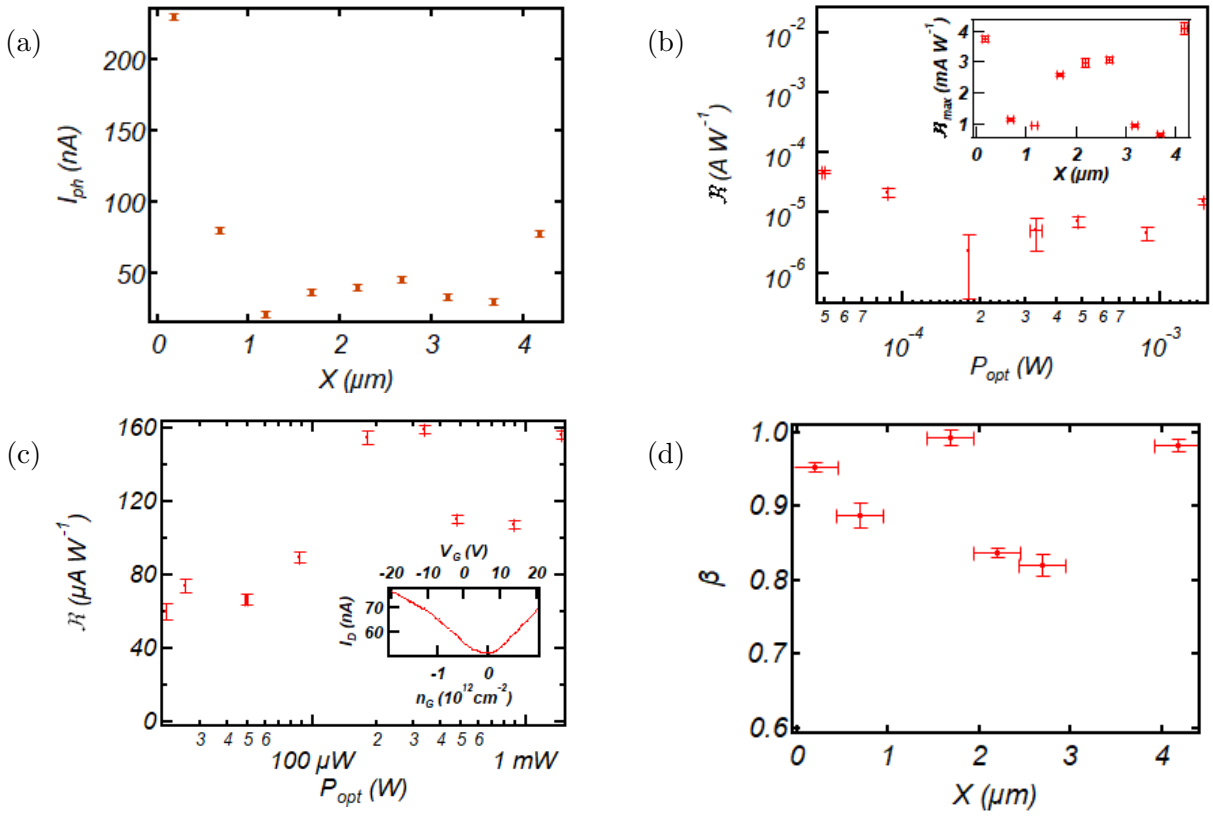

Figure 4.11: Photocurrent line map of Device A. (a) Maximum photocurrent measured at various positions along the graphene channel. Data is presented as absolute value to compare magnitude of photoresponse. (b) Responsivity vs power along the channel. Inset shows max responsivity as a function of laser spot position. Note that the largest photoresponses are nearest the contacts, and a smaller photoresponse was measured near the channel center. (c) Power sweep including the maximum photoresponsivity, recorded nearest the source contact. Inset shows a gate sweep obtained in the dark, indicating the charge density of the device before photocurrent acquisitions. Device A was lightly hole-doped at $V_G = 0$ during photocurrent experiments. (d) Photocurrent exponent vs channel position.

too sensitive to changes in charge density and requires a vacuum- and temperature-controlled environment to ensure repeatability.

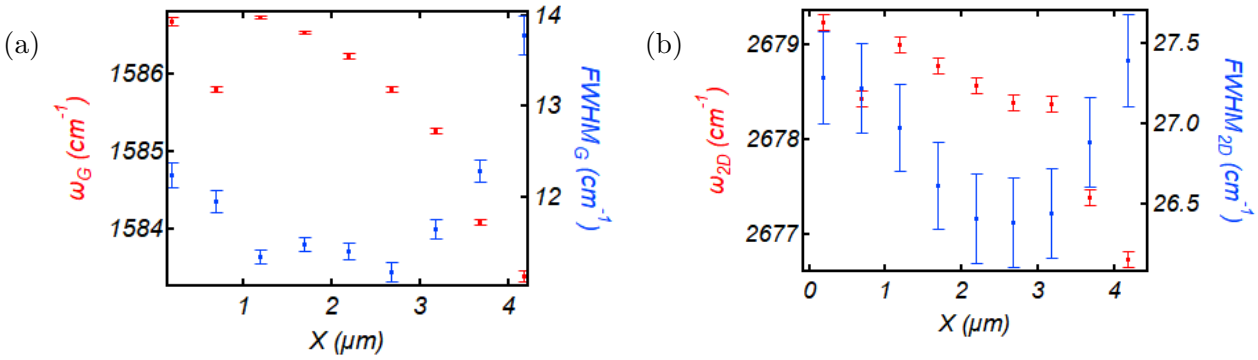

Figure 4.12: Raman line map of Device A. (a) G peak Raman shift and width as a function of channel position. The FWHM increases near the source-drain contacts because there is less Raman signal due to much of the optical excitation reflecting off of the gold contacts. The G peak trended toward softening near the end of the map, which may be due to changes in temperature or charge density over the course of the experiment. (b) The 2D peak FWHM dips near the channel center, much like for the G peak, due to more Raman signal collected.

Along with photocurrent data, we simultaneously acquired Raman measurements, presented in figure 4.12. The FWHM of Raman peaks is commonly associated with crystal quality and plastic deformation, and the peak positions are sensitive to heating, charge density, and strain, among other things. In particular, we know that the peak widths decrease with increased charge density, while the peak positions increase [17][34]. Additionally, we know that the peak positions decrease with increased heating[21]. In our own data, we see that the FWHM of both the G and 2D peaks is highest near the gold contacts, and decreases within the bulk of the graphene channel. This could be due to graphene near/under the contacts having a different amount of internal tension or compression compared to the exposed channel. The resulting dip in FWHM may also be due to a difference in charge densities between the contacted and exposed graphene regions, of which the former is fixed and the latter is tuned by the gate voltage.

The observed change in peak positions for G and 2D peaks follow a slightly different pattern, initially decreasing slightly in Raman frequency while approaching the drain contact, and then falling drastically as it reaches the drain contact. On the one hand, this could be due to a decrease in charge density during the measurement, though unilluminated gate sweeps before and after the map indicate an increase in hole-doping. It may instead be increasing

sample temperature during the course of the experiment, although one would expect the gold contacts to act as a heat sink resulting in higher peak positions near the contacts. Further still we might argue that the strain in the graphene is non-uniform and is greatest near the drain contact. However, it was shown by Tsukamoto in 2012 that water on the surface of graphene, or trapped beneath it, will blue-shift the Raman G and 2D peaks, increasing their frequency [10]. Since our Raman frequencies red-shift while approaching the end of the experiment, we might conclude that the moisture content decreased, perhaps due to changes in humidity in the room or more effective annealing over time.

In the end, this set of data illustrates the difficulty of measuring monolayer photocurrents at room temperature, humidity, and pressure. An optical cryostat would certainly provide a repeatable environment and remove the need for repeated anneals, but surrounding the translation stage in a dry environment may be enough to ensure repeatability. The monolayer flake is too sensitive to perturbations by ambient conditions, and would be best investigated in vacuum. In terms of photocurrent devices, two-point monolayer graphene devices with dimensions on the order of micrometers are less robust, have worse performance, and suffer greater noise than comparable bilayer devices.

4.5 Conclusions

In this chapter, we introduced our graphene transistor devices for discussion, along with their characteristic electronic transport and dimension quantities, and then presented our top 3 results. First, we showed that photocurrent exhibits a maximum magnitude when the laser spot target is closest to either source or drain electrodes, and that a bilayer device will yield about twice as much photoresponse as a comparably-sized monolayer device. Second, we showed that changes in charge density will affect the magnitude of the photocurrent, but not the proportional contribution of the photocurrent mechanisms. And finally we demonstrated that when the laser spot is farther than the electron mean free path from the contacts that likely only the PTE effect can contribute to the photocurrent in a bilayer device. A monolayer device showed a possible reduction in PV effect near the channel center, although uncertainty of the measurement was significantly larger than the bilayer device.

Chapter 5

Conclusions and Prospects

We have demonstrated that by combining the capabilities of two independently-designed optical and electronic measurement systems, we were able to study photocurrent physics in graphene FET's. By probing graphene with a focused laser spot and measuring the photoresponse current, we can investigate photocurrent generation mechanisms and their dependence on incident optical power. Furthermore we can map this information with respect to the laser spot target position. In this conclusion, we begin with a brief summary of our main results as described in Chapters 3 and 4, as well as their implications for the design of graphene-based photodetectors. Finally we will end with a discussion of how to improve our opto-electronic apparatus and procedures in order to improve resolution and add new capabilities, as well as what is possible for future experiments.

5.1 Main Results

We presented a basic theoretical framework with which to understand the physics of photocurrent generation in graphene explored throughout this thesis. We began with a description of the graphene lattice and its electron band structure. We then summarized diffusive electron transport and the effects on transport of surface contaminants, especially water. We then provided a background of Raman spectroscopy on graphene, with special attention to extracting Raman features in order to quantify the number layers of graphene in a sample in addition to the quality of sample by its defect density. We use these concepts in Chapter 4 to characterize our samples by number of layers and defect density, as well as to monitor any changes in the lattice temperature, charge carrier doping, or defect density during

photocurrent measurements. Next we provided a basic theoretical background for the three most prominent photo-generation mechanisms in graphene-based devices: the photovoltaic, photo-thermoelectric, and photo-bolometric effects. We again use this in Chapter 4 as a basis to understand and interpret our results.

We presented our fabrication and device production processes, our custom measurement apparatus capable of simultaneous opto-electronic measurements with sub-micron precision on graphene FET's, demonstrations of our analysis techniques, and measurement protocols. Our fabrication process produces graphene devices of high quality and with low structural disorder by design, with dimensions of up to several microns to allow for optical probing with a laser spot with FWHM of up to 0.4 μm. We then detailed our custom apparatus and modifications for simultaneous optical and electronic measurements while addressing the hardware and software challenges of synchronizing two systems not designed to cooperate with each other. Next we outlined our measurement and annealing procedures to produce spatially-resolved photocurrent maps in addition to photoresponse optical power sweeps.

In Chapter 4, we presented the results of our experiments on three devices: one monolayer and one bilayer graphene device of comparable dimensions, and one large, irregularly shaped monolayer device. Through dark transport measurents, we determined device A to be a monolayer with $R_{\max} = 8.639\ k\Omega$ and mean free path $\ell =$ 113-194 nm, device B to be a bilayer with $R_{\max} = 16.2\ k\Omega$ and mean free path $\ell = 7\ nm$, and device C to be a trapezoidal monolayer with $R_{\max} = 2.915\ k\Omega$ and mean free path $\ell =$ 43.6-194 nm. For devices A and B, we found photocurrent exponents of $\beta = 0.9 \pm 0.1$ and $\beta = 1.0 \pm 0.1$ near the contacts, indicating that the primary contributor to photocurrent in our devices is the PV effect, with some contribution from the PTE effect. For device B, we found that while an increase in charge density did increase the resulting photocurrent, the dominant photocurrent mechanism did not change within the uncertainty of our measurement. While the photoresponse measured near the channel center in our bilayer device was significantly weaker than near the source contact, we found that it also exhibited a different dependence on laser power, with $\beta_{\text{contact}} = 1.1 \pm 0.1$ and $\beta_{\text{center}} = 0.6 \pm 0.1$. We argue that while both PV and PTE effects require charge carriers to reach a built-in electric field, such as at a junction (graphene-contact), only the PTE-generated hot electron-hole pairs can effectively exceed the electron mean free path to reach the built-in electric field before recombining. Thus when the photogeneration occurs more than the mean free path from the nearest contact, only the PTE effect can contribute to the net photocurrent. We had great difficulty making conclusions about the spatial dependence of β in device A, likely due to its sensitivity to charge doping

from the ambient environment, however we did observe that the largest photocurrents measured were nearest the contacts. From the Raman spectra simultaneously acquired, we see that the G and 2D peak positions shift during the course of the 5-hour measurement set, especially toward the end, suggesting that the charge doping was decreasing. This may mean that we had a lower surface moisture content near the end than at the beginning, and that our anneal procedure was not enough to compensate for the ambient humidity. Our bilayer device, being more absorptive and robust, is better suited for room-temperature, ambient pressure photodetector applications.

5.2 Prospects for Graphene Photodetectors

All of the photocurrent experiments presented in this thesis were acquired at bias voltage $V_B = 0$ in order to preclude any photoresponse due the photobolometric effect. However some research claims that the photobolometric effect dominates the photoresponse of biased graphene, and therefore it is certainly an area of interest for photodetector design applications [35][3]. Once we understand the photobolometric effect and how to distinguish it experimentally from PV and PTE effects, we will be able to interpret photoconductive experiments. Our current setup is capable of performing biased transport photocurrents, and such measurements would be the obvious next step. Photo-illuminated bias sweeps can characterize the photodetector performance of graphene devices in terms of photoresponsivity and open-circuit voltage.

Further still, there has been observed an intrinsic photoresponse in graphene for $V_G = V_D$ and $V_B = 0$, shown in figure 5.1, which has interesting spatial dependence and is not explained by theory for photovoltaic, photo-thermoelectric, or photo-bolometric effects [36]. This so-called "intrinsic" photoresponse has only begun to be investigated, and to the best of our knowledge has not been analyzed according to its photocurrent exponent dependence on laser spot target. We believe that this photoresponse was at least in part responsible for the odd distribution of photocurrents observed in 2D maps of device C. Our measurements were acquired at low charge carrier doping, but future experiments can be performed at incremental carrier densities starting from the Dirac point, mapping the evolution of the photoresponse. Investigation into the photocurrent dependence on device shape, particularly when $V_G = V_D$, is ripe for exploration.

With our custom setup, we are well-equipped to study photoresponsive devices, and may

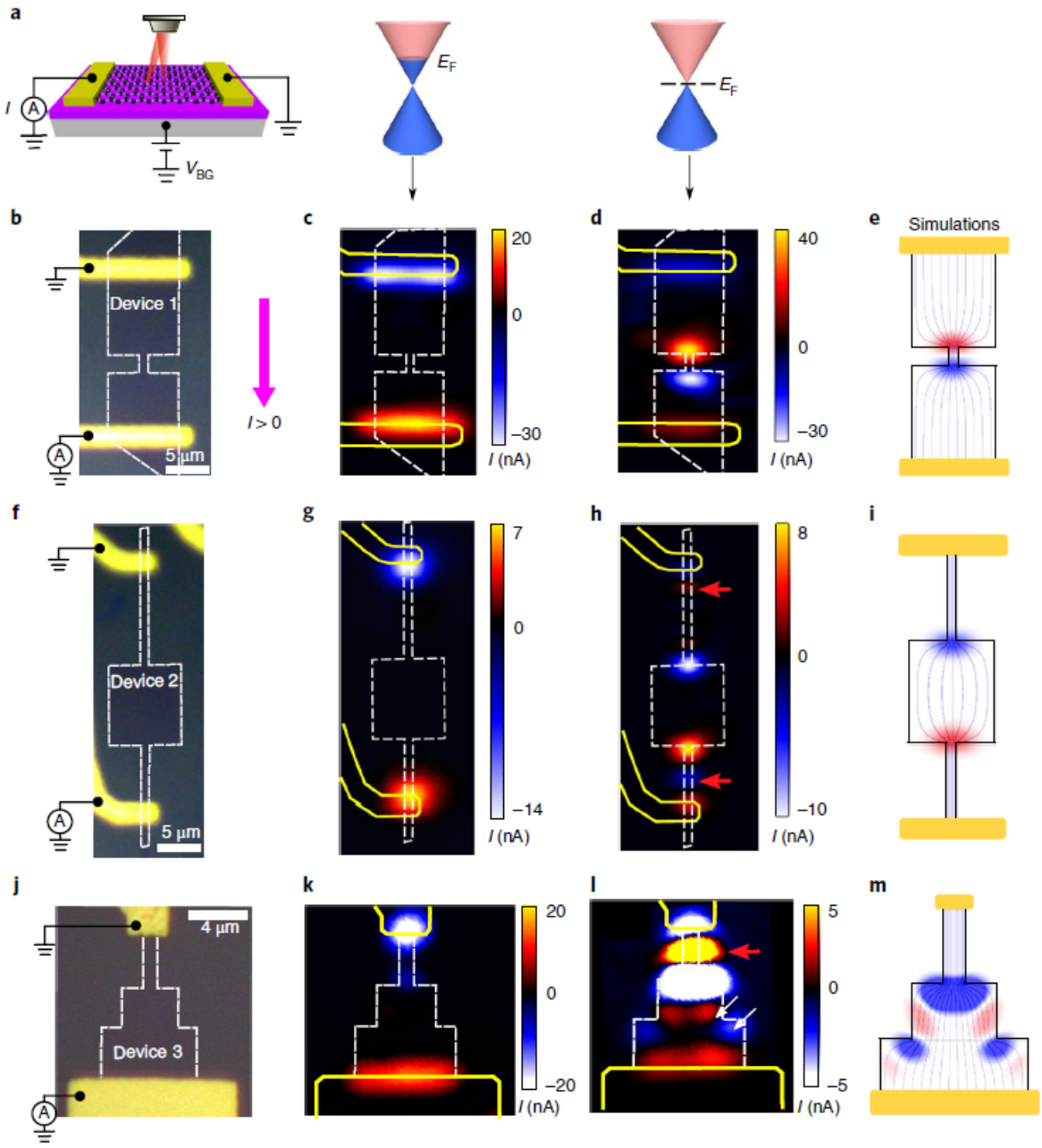

Figure 5.1: Comparison of photocurrent maps on graphene for V_G and V_D. (a) Illustration of experimental setup and measurement circuit, with the laser spot scanning on a two-point graphene device with shorted bias and controlled back gate voltage. (b,f,j) Optical images of devices with different geometries. (c,g,k) Scanning short-circuit photocurrent maps of devices 1-3 for $V_G - V_D > 0$. The photocurrents measured are commonly attributed to the photovoltaic and photo-thermoelectric effects, and are greatest at the contact interfaces. (d,h,l) Scanning short-circuit photocurrent maps of devices 1-3 for $V_G - V_D = 0$. The locations of maximum photoresponse are no longer near the contacts, and much stronger photoresponses are generated near edges where a change of geometry occurs. (e,i,m) Authors' simulations attempting to model and predict locations of maximum photoresponse for $V_G - V_D = 0$. Figure borrowed from [36]

expand to other materials such as carbon nanotubes, MoS_2, WS_2, $MoSe_2$, WSe_2, SnS_2, ReS_2, $MoTe_2$, GaS, $GaTe$, $SnSe_2$, h-BN, MoO_3, Bi_2Te_3, Si, Ge, ZnO, $GaAs$, $InAs$, and heterostructures combining these and other materials [37]. With the exception of ZnO, MoO_3, ZnO, and h-BN, all of these materials have band gaps under the 2.33 eV photon energy of our laser and therefore require no modifications to our current optical setup.

A major limitation of our setup, however, is the inability to control temperature or conduct experiments under vacuum. All of our measurements were performed at room temperature, exposed to the ambient environment. As discussed in Chapter 2 and observed in Chapter 4, ambient air and its moisture content can significantly impact charge carrier transport in graphene, especially in monolayer devices. By introducing vacuum capabilities into our system, we would simplify the physics of our measurements by removing a significant source of doping and eliminate the need for our optical annealing procedure. Noise of measurements would reduce in general, but especially we would be able to explore the photocurrents of monolayer graphene which is particularly sensitive to ambient conditions. Temperature control would allow us to explore the rich physics at cryo temperatures, at which the PV and PTE effects are expected to be enhanced due to weakening of electron-phonon interactions at low temperature. Additionally, we would then be able to explore the Kohn anomaly in monolayer graphene via simultaneous Raman and electrical measurements.

To add temperature control and vacuum features, we require an optical cryostat compatible with our translation stage, a new sample holder with electrical connections designed for use in the optical cryostat, and a microscope objective with a long working distance compatible with a cover slip matching the cryostat's window. Alternatively, it may be enough address the humidity issue by surrounding the translation stage in a non-airtight container and pumping a steady supply of dry air to the sample environment. This would provide a stable, low-humidity environment in which to carry out experiments, and likely both reduce the time to optically anneal samples and extend the anneal recovery time.

Besides working with other materials or heterostructures, structural modifications to the size, spacing, and shape of our gold contacts can enhance photodetection. Groups have investigated sub-wavelength ($L < \lambda_{\text{photon}}$) [38], as well as plasmon-induced [39] and fractal metasurface [40] photocurrent enhancements. With electron-beam lithography, we can design features on our contacts on the order of 10^3 nm to take advantage of surface plasmon enhancements. We chose to work with microns-scale devices so that we could map the spatial dependence of photocurrent and photocurrent mechanisms, but sub-wavelength devices

could be explored within the context of photocurrent mechanisms. If we develop instrumentation for vacuum and temperature control, such devices could be investigated to observe the relationship between photocurrent and ballistic electron transport.

Bibliography

[1] V. Patil, A. Capone, S. Strauf, and E.-H. Yang, Sci Rep **3**, 2791 (2013).

[2] M. Freitag, T. Low, F. Xia, and P. Avouris, Nature Photonics **7**, 53 (2012).

[3] R. Jago, E. Malic, and F. Wendler, Physical Review B **99** (2019).

[4] M. W. Graham, S.-F. Shi, D. C. Ralph, J. Park, and P. L. McEuen, Nature Physics **9** (2012).

[5] F. Xia, T. Mueller, R. Golizadeh-Mojarad, M. Freitag, Y.-m. Lin, J. Tsang, V. Perebeinos, and P. Avouris, Nano Letters **9** (2009).

[6] F. H. L. Koppens, T. Mueller, P. Avouris, A. C. Ferrari, M. S. Vitiello, and M. Polini, Nature Nanotechnology **9** (2014).

[7] J. Wang, H. Fang, X. Wang, X. Chen, W. Lu, and W. Hu, Small **13** (2017).

[8] Y. Zhang, H. Zheng, Q. Wang, C. Cong, L. Hu, P. Tian, R. Liu, S. L. Zhang, and Z. J. Qiu, Small **14**, e1800691 (2018).

[9] S. Riazimehr, S. Kataria, R. Bornemann, P. Haring Bolivar, F. J. G. Ruiz, O. Engstrom, A. Godoy, and M. C. Lemme, ACS Photonics **4**, 1506 (2017).

[10] T. Tsukamoto, K. Yamazaki, H. Komurasaki, and T. Ogino, The Journal of Physical Chemistry C **116**, 4732 (2012).

[11] S. Zhuang, Y. Chen, W. Zhang, Z. Chen, and Z. Wang, Science China Physics, Mechanics & Astronomy **61** (2017).

[12] V. C. T. Matthew J. Allen and R. B. Kaner, Chemical Reviews **110**, 132 (2010).

[13] A. H. Castro Neto, F. Guinea, N. M. R. Peres, K. S. Novoselov, and A. K. Geim, Reviews of Modern Physics **81**, 109 (2009).

[14] Y.-J. Yu, Y. Zhao, S. Ryu, L. E. Brus, K. S. Kim, and P. Kim, Nano Lett **9**, 3430 (2009).

[15] A. C. McRae, *Graphene Quantum Strain Transistors and Two-in-One Carbon Nanotube Quantum Transistors*, Ph.D. thesis (2018).

[16] Y. Jia, X. Gong, P. Peng, Z. Wang, Z. Tian, L. Ren, Y. Fu, and H. Zhang, Nano-Micro Letters **8**, 336 (2016).

[17] R. Saito, M. Hofmann, G. Dresselhaus, A. Jorio, and M. S. Dresselhaus, Advances in Physics **60**, 413 (2011).

[18] InPhotonics Technical Notes #11 (1999).

[19] C. T. Stephanie Reich, The Royal Society **365** (2004).

[20] A. C. Ferrari, J. C. Meyer, V. Scardaci, C. Casiraghi, M. Lazzeri, F. Mauri, S. Piscanec, D. Jiang, K. S. Novoselov, S. Roth, and A. K. Geim, Phys Rev Lett **97**, 187401 (2006).

[21] I. Calizo, A. A. Balandin, W. Bao, F. Miao, and C. N. Lau, Nano Lett **7**, 2645 (2007).

[22] I. Calizo, F. Miao, W. Bao, C. N. Lau, and A. A. Balandin, Appl Phys Lett **91**, 071913 (2007).

[23] D. Graf, F. Molitor, K. Ensslin, C. Stampfer, A. Jungen, C. Hierold, and L. Wirtz, Nano Letters **7**, 238 (2007).

[24] D. K. Sharma, S. Fateixa, M. J. Hortigela, R. Vidyasagar, G. Otero-Irurueta, H. I. S. Nogueira, M. K. Singh, and A. Kholkin, Physica B: Condensed Matter **513**, 62 (2017).

[25] A. C. Ferrari and D. M. Basko, Nature Nanotechnology **8**, 235 (2013).

[26] U. Jung, Y. G. Lee, C. G. Kang, S. Lee, J. J. Kim, H. J. Hwang, S. K. Lim, M. H. Ham, and B. H. Lee, Sci Rep **4**, 4886 (2014).

[27] X. Xie, Y. Peng, X. Yang, X. Chen, X. Hu, X. Xu, P. Yu, and R. Wang, "Raman analysis of phonon lifetimes in 4h-sic and their doping dependence," in *2016 13th China International Forum on Solid State Lighting: International Forum on Wide Bandgap Semiconductors China (Sslchina: Ifws)* (2016) pp. 23–26.

[28] A. Srivastava, X. Chen, and A. K. Pradhan, "Photo-electronic current transport in back-gated graphene transistor," in *Society of Photo-Optical Instrumentation Engineers (SPIE) Conference Series*, Vol. 10167 (2017) p. 101671H.

[29] J. Yan, M. H. Kim, J. A. Elle, A. B. Sushkov, G. S. Jenkins, H. M. Milchberg, M. S. Fuhrer, and H. D. Drew, Nature Nanotechnology **7**, 472 (2012).

[30] M. R. Abel, *Thermal Metrology of Polysilicon MEMs Using Raman Spectroscopy*, Ph.D. thesis (2005).

[31] K. I. Bolotin, K. J. Sikes, Z. Jiang, M. Klima, G. Fudenberg, J. Hone, P. Kim, and H. L. Stormer, ArXiv (2008).

[32] S. Yigen and A. R. Champagne, Nano Letters **14**, 289 (2014).

[33] K. Keramatnejad, Y. S. Zhou, D. W. Li, H. R. Golgir, X. Huang, Q. M. Zhou, J. F. Song, S. Ducharme, and Y. F. Lu, Advanced Materials Interfaces **4**, 1700294 (2017).

[34] A. C. Ferrari, Solid State Communications **143**, 47 (2007).

[35] R. Jago, F. Wendler, and E. Malic, Physical Review B **96** (2017).

[36] Q. Ma, C. H. Lui, J. C. W. Song, Y. Lin, J. F. Kong, Y. Cao, T. H. Dinh, N. L. Nair, W. Fang, K. Watanabe, T. Taniguchi, S.-Y. Xu, J. Kong, T. Palacios, N. Gedik, N. M. Gabor, and P. Jarillo-Herrero, Nature Nanotechnology (2018).

[37] X. M. Li, L. Tao, Z. F. Chen, H. Fang, X. S. Li, X. R. Wang, J. B. Xu, and H. W. Zhu, Applied Physics Reviews **4** (2017).

[38] F. Leonard, C. D. Spataru, M. Goldflam, D. W. Peters, and T. E. Beechem, Sci Rep **8**, 45873 (2017).

[39] V. Shautsova, T. Sidiropoulos, X. Xiao, N. A. Gusken, N. C. G. Black, A. M. Gilbertson, V. Giannini, S. A. Maier, L. F. Cohen, and R. F. Oulton, Nat Commun **9**, 5190 (2018).

[40] J. Fang, D. Wang, C. T. DeVault, T. F. Chung, Y. P. Chen, A. Boltasseva, V. M. Shalaev, and A. V. Kildishev, Nano Lett **17**, 57 (2017).